공학박사 학위논문

전기자동차 주행거리 증대를 위한 통합열관리시스템에 관한 연구

An Integrated Electric Vehicle Thermal Management System for Range Extension

2020년 8월

서울대학교 대학원

기계항공공학부

김 귀 택

Abstract

An Integrated Electric Vehicle Thermal Management System for Range Extension

Gwi Taek Kim
Department of Mechanical and Aerospace Engineering
The Graduate School
Seoul National University

The mileage of a single charge of an electric vehicle is determined by the capacity of the mounted battery. However, due to the limitation of energy density per unit weight of lithium-ion batteries that have been applied recently, the maximum mileage of an electric passenger car is less than about 500 km. However, this mileage is greatly changed by the outside temperature, causing the driver anxiety, which is known as a major obstacle to the expansion of electric vehicles. The main cause of the change in the driving distance according to the outside temperature is that the air conditioning load used for indoor heat management of the vehicle is large and also varies according to

the outside temperature. In this study, we proposed an integrated heat management system with a low rate of change in power consumption of the air conditioning system according to the outside temperature, and quantitatively analyzed the effect of these systems on the mileage extension of electric vehicles.

First, a method for predicting the amount of heat generated from a battery, a motor, and an inverter of an electric vehicle was presented based on simulation. The battery, the motor, and the inverter each continuously store and convert electrical energy. In this process, electrical energy moves in the form of voltage and current. In this study, an integrated power transmission model for real-time conversion of mechanical and electrical energy was developed to quantitatively measure the amount of heat generated by each component.

In order to quantitatively calculate the air conditioning load required in the interior of the vehicle according to the outdoor temperature, a vehicle interior model based on thermal comfort was developed. In the developed model, it is possible to predict a more realistic air conditioning load by considering not only radiant energy introduced from the outside of the vehicle, but also specific heat of the vehicle interior material.

We designed an integrated heat management system that can be applied

based on the amount of heat generated from the battery, inverter, and motor and the air conditioning load. Experimental studies were conducted to verify the performance and efficiency of the designed system, and as a result, a reduction in power consumption of about 12% under heating conditions and about 5% under cooling conditions was confirmed.

An electric vehicle mileage prediction model was developed to confirm the impact of such reduction in power consumption on the mileage of an electric vehicle. As a result of confirming the effect of increasing the mileage for various outdoor conditions, an effect of increasing the mileage of about 10% is expected. If the integrated heat management system proposed in this study is applied to electric vehicles, it is expected that the mileage change rate according to the outside temperature can be reduced and further contribute to the supply of electric vehicles.

Keywords: Electric vehicle, Integrated thermal management system, Heat pump, Range extension

***Identification Number*: 2015-30996**

Contents

List of Figures

List of Tables

Nomenclature

A	area (m^2)
Bo	Boiling number
C_p	specific heat (kJ/kg·K)
COP	coefficient of performance
D	diameter (m)
DSC	degree of subcool (K)
DSH	degree of superheat (K)
EEV	electronic expansion valve
f	friction factor
G	mass flux (kg/s·m^2)
g	gravitational accerleration (= 9.81 m/s^2)
h	heat transfer coefficient (kW/m^2·K)
h_{fg}	speicif latent heat (kJ/kg)
i	enthalpy (kJ/kg)
j	Couburn j factor
k	thermal conductivity (kW/m·K)
L	length (m)
m	mass (kg)
$\dot{m}$	mass flow rate (kg/s)
Nu	Nusselt number
n	polytropic coefficient

P	pressure (kPa)
Pr	Prandtl number
Q	capacity (kW)
Q’	heat flux (kW/m)
Re	Reynolds number
s	gradient
T	temperature (K)
U	overall heat transfer coefficient ($kW/m^2 \cdot K$)
V	velocity (m/s)
v	specific volume (m^3/kg)
W	work (kW)
x	vapor quality

Greek

η	efficiency
ε	void fraction
μ	dynamic viscisity (Pa·s)
ρ	density (kg/m^3)
σ	surface tension (N/m)
ω	frequency (Hz)

Subscript

air	air side
amb	ambient
C	cooling
comp	compressor
cond	condenser
dis	dischrage
disp	displacement
eev	electronic expansion valve
g	gas
H	heating
hps	high pressure side
i	inside
in	inlet
l	liquid
ll	liquid line
lps	low pressure side
max	maximum
o	outside
oil	lubricant
out	outlet
s	surface
sat	saturate

sc	subcooled
sh	superheated
sol	solubility
tp	two phase
v	vapor
V	volumetric
w	wall

Chapter 1. Introduction

1.1 Background of the study

Human beings have a limit on the range of movement due to the physical limitations. However, by using vehicles the individuals can escape from space constraints. Vehicles that has grown with the development of internal combustion engines are in the midst of a paradigm shift, based on connectivity, autonomous, sharing, and electrification (C.A.S.E). In particular, the electrification of automobiles is gaining a strong growth potential in terms of reducing the high oil dependence and reducing air pollution sources. According to the IEA World Energy Balances 2019 [1], the total final energy consumption is 9,717 Mtoe in worldwide, and transport accounts for about 29% (2,808 ktoe) as shown in Fig. 1.1. In addition, 92% of the energy used in transport comes from oil, one of the primary energy sources [1]. As the conventional ground transport is highly dependent on fossil fuel, shown in Fig 1.2, it may be vulnerable to changes in the oil prices. Moreover, they may not be able to fill the requisition of sustainable development when the oil supply chain is threatened. Furthermore, the internal combustion engine (ICE) are causing

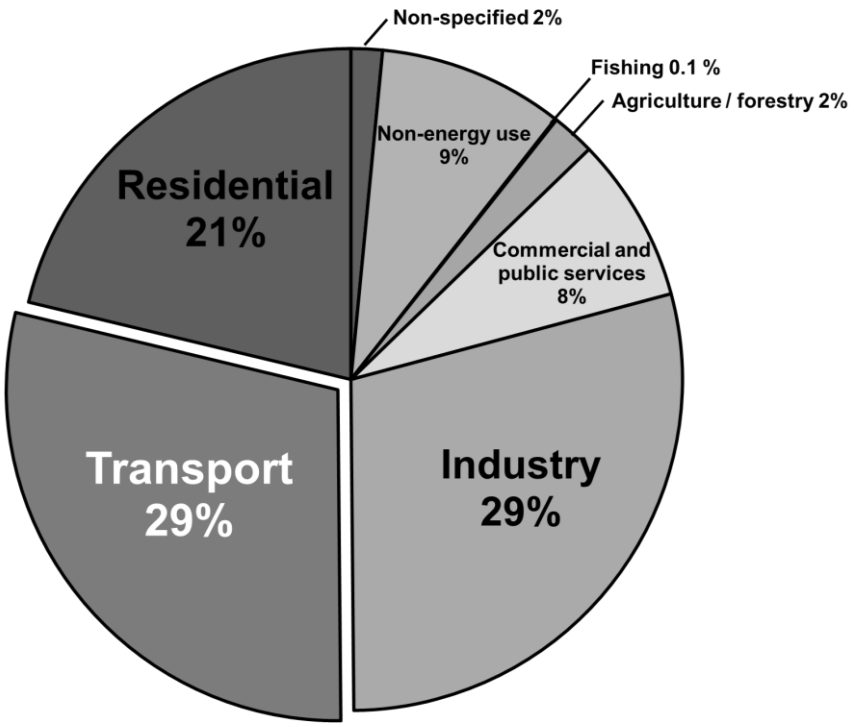

Fig. 1.1 The world total energy consumption by sector (IEA, 2019)

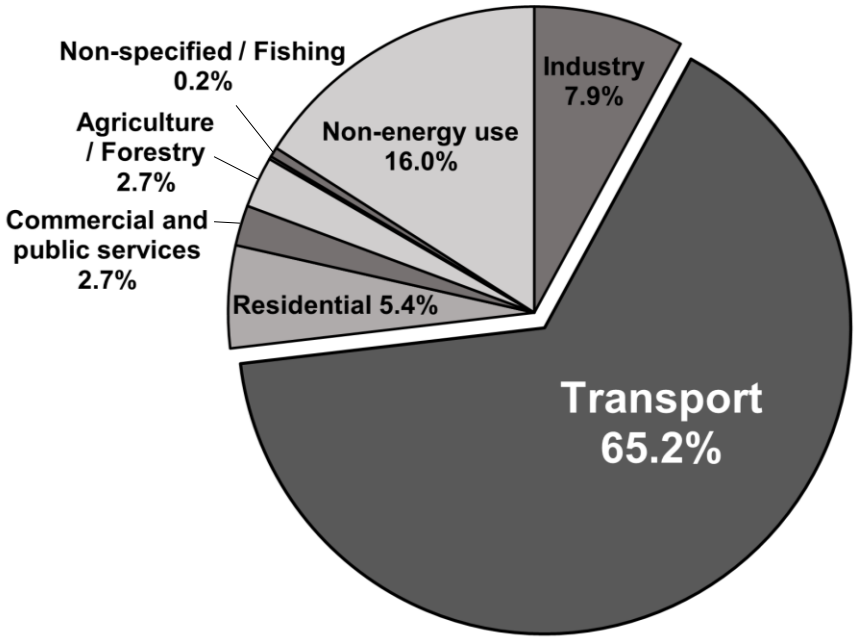

Fig. 1.2 Oil products final consumption by sector (IEA, 2019)

environmental problems as well producing combustion by-products ranging from carbon dioxide, nitrogen dioxides, and sulfur dioxide which can impact human health and global environmental [2]. Therefore, the electrification of vehicles has been receiving considerable attention due to the energy paradigm shift, and has continued to settle in, producing electric energy from renewable energy such as solar, wind farms, and geothermal by escaping from the petroleum energy source that is presumably to be exhausted. In addition, the electric traction system converts stored electrical energy into mechanical energy, resulting in high conversion efficiency and zero emissions to air [3].

Despite the needs of the times, electric powertrain system is inconvenient in charging electric energy, unlike ICE vehicles that can get the fluid energy without great difficulty and conscious effort. Unlike other electric vehicle, such as various hybrid-electric vehicles (HEVs) and plug-in hybrid electric vehicles (PHEVs), a battery electric vehicle (BEV) is a vehicle that is powered entirely on electric energy, typically a large electric motor and a large battery pack. Range anxiety is the fear that the electric vehicle won't have sufficient electric energy to reach its duty. The range anxiety for battery electric vehicle is due to the charging time and stations which are sparsely located. It occurs because there are not enough charging stations, and it takes time to charge as little as 20-40 minutes even though it is supported from fast charging technology. More

important than the cause of the concern is the difficulty of predicting remaining mileage of electric vehicle. Many studies related to the dissemination of electric vehicles consistently noted that the range anxiety phenomena is one of the biggest obstacle for electric vehicle commercialization [4,5,6]. Fig 1.3 shows the decrease in the mileage of the electric vehicle according to the change in the ambient temperature and the operation of the heating, ventilation, and air conditioning (HVAC), and it can be indirectly confirmed that such a reduction in driving distance can sufficiently cause a range anxiety to the driver [7]. When the HVAC system works at 35ºC, there is 17.2% mileage reduction, and it operates at -6.6ºC, it can be seen that the mileage is reduced by up to 40.5%. In particular, in winter, it can be seen that the decrease in mileage is greater than the hot weather condition. This is because electric vehicles perform indoor heating through a positive temperature coefficient (PTC) heater or heat pump system because there is no sufficient waste heat source like ICE.

In order to reduce the effect of ambient temperature on the range reduction, there have been two systematic approaches in solving the problem both external and internal approach respectively. Some typical example of external approaches are building more charging stations [8], fast- charging strategy [9], and using car sharing tactic [10]. The internal approaches is progressing mainly at first stage of the vehicle concept development. This strategy can be classified

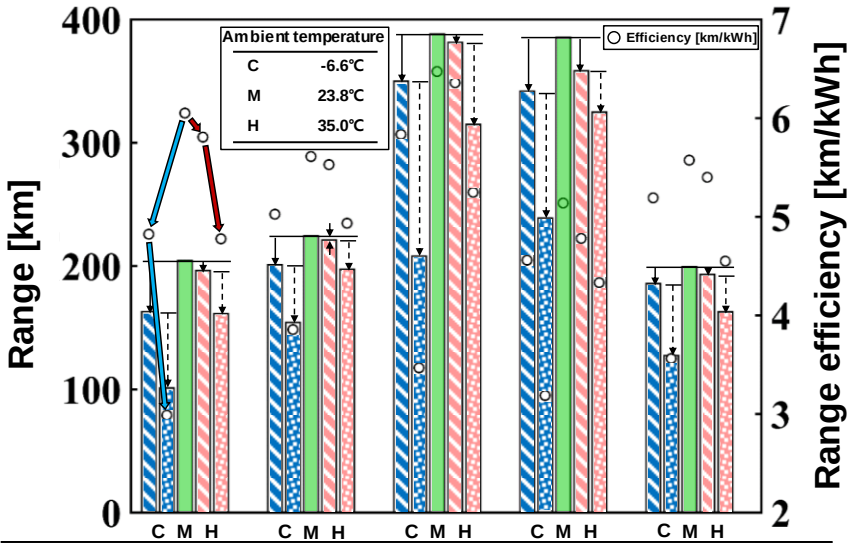

Temp.	HVAC	2018 i3s	2018 Leaf	2018 Bolt	2017 Model S	2017 e-Golf	Avg.(%)
-6.6℃	OFF	**-20.3**	-10.4	-9.9	-11.3	**-6.9**	-11.7
	ON	**-50.6**	**-31.3**	-46.4	-38.0	-36.1	-40.5
35.0℃	OFF	-4.0	**-1.4**	-1.7	**-7.0**	-3.1	-3.5
	ON	**-21.1**	-12.1	-18.9	**-15.7**	-18.4	-17.2

Fig. 1.3 The effect of ambient temperature on driving range reduction

into methods of producing electric energy inside the vehicle and supplying it to the electric energy storage system, and methods of reducing the electric energy consumed by the vehicle to increase the driving range. As a technique of generating electric energy in a vehicle, there are many ways ranging from operation of a gas generator [11], installation of some solar panels on the roof of it [12], and using regenerative braking system [13]. In order to extend the mileage, various strategies have been devised to reduce energy consumption including driving energy. As a typical example, there is a way of devising an optimal driving pattern reducing electric energy consumed in driving by adjusting the acceleration and deceleration of a vehicle and simultaneously generating a maximum amount of regenerative braking energy [14]. However, considering that the electric energy used in the HVAC is the largest part of the electric energy consumed in the entire vehicle except for the driving energy, it is clear that the efficiency of the HVAC system is the most influential factor on the range [15]. Consequently, it is necessary to develop an HVAC system that is vulnerable to ambient temperature, i.e., a system with little difference in energy consumption despite changes in ambient temperature. Also, the system should satisfy the thermal comfort for the cabin room continuously, and at the same time, minimize the reduction in mileage, consuming as little energy as possible.

1.2 Literature survey

1.2.1 Electric powertrain thermal management system

For ICE vehicles, the thermal connectivity between the engine thermal management system and the HVAC system is almost weak because the operating temperature of each system has a large difference. The thermal management for power train and cabin thermal management were independently performed. Since the outdoor heat exchanger (condenser) for HVAC system is located in front of the coolant radiator for power train thermal management, the temperature of the air entering the radiator tended to be higher than that of the air entering to the condenser. However, in the case of electric vehicles, it is desired to reinforce the mutuality between the both thermal management system, electric powertrain and cabin HVAC. In particular, it is required to cool down the lithium-ion battery pack using the HVAC system due to maintain its optimum temperature range. Therefore, it is necessary to investigate the electric powertrain system to design an efficient HVAC system. Electric vehicle configurations include battery electric vehicles (BEVs), various hybrid-electric vehicles (HEVs), and plug-in hybrid electric vehicles (PHEVs). Also, there are fuel cell electric vehicles powered by hydrogen. Unlike other electric powertrain systems, the battery electric vehicle which is

powered by 100% electric energy from the battery, so there is an adverse impact of energy use on range reduction. Therefore, in this study, the battery electric vehicles considered as a subject of study.

A large number of comprehensive studies for electric drivetrain for EV have been carried out in diverse aspects to extend the driving range; however, most studies have been focused on performance improvement, and enhancement of efficiency remaining have a little interest research on a systematic approach. As for the component, energy storage system (ESS), and power electronics and electric machine (PEEM) are essential components of the electric drivetrains. It is a priority to enhance the energy density of battery in particular. Until now, a lithium-ion battery is widely adopted in major carmakers with its superiority in energy density, cycle life, and safety [16]. Many types of lithium-ion batteries with various cathode metal oxides have been studied, such as lithium cobalt oxide (LCO), lithium manganese oxide (LMO), and lithium nickel manganese cobalt oxide (NMC) [17]. As a result, the energy density of commercial lithium-ion batteries has begun to approach its theoretical limit (250 Wh/kg) [18]. Therefore, several types of next-generation batteries have been considered to break through this limitation [19]. For example, the all-solid-state battery can overcome the intrinsic limitation of the organic liquid electrolyte in the conventional lithium-ion battery [20]. It is

also reported that batteries with substitute anode material have higher theoretical limits of energy density, such as silicon-lithium [21] and lithium-air [22] batteries. In the case of a lithium-ion battery with optimum operating temperature, various studies have been conducted on the battery pack. Siruvuri and Budarapu [23] studied for the thermal management of lithium-ion battery pack using water as the cooling fluid. Wang et al. [24] conducted an experimental and simulation research for the lithium-ion battery pack using phase change material. Lai et al. [25] did a numerical research for the liquid-cooled thermal management system for cylindrical type battery pack. Not only ESS, but also PEEM can also affect the performance and mileage of electric vehicles. To increase the performance of PEEM, an interior permanent magnet synchronous motor (IPMSM) is receiving the most attention [26]. Different types of motors have been studied for increasing the energy density and efficiency of electric machines. Axial flux permanent magnet machine (AFPMM), synchronous reluctance machine (SynRM), and permanent magnet assisted SynRM (PMa-SynRM) are the promising power traction motor for electric vehicles [27]. Tariq et al. [28] studied the effect of cooling conditions on the design and operation of IPMSM. Park [29] did a numerical research to find out the temperature of coil, stator, magnet, and rotor with water cooling jacket system. Kang [30] did a simulation research for the effect of rotor cooling

holes to cool down the rotor temperature. A regenerative braking system (RBS) is also an essential part of motor technologies. Employing the electric motor as a generator, RBS allows kinetic energy to be recycled rather than to dissipate the energy as heat. Recent studies are focusing on the control optimization of a regenerative braking system. Li et al. [31] suggested a hierarchical control strategy to maximize the efficiency improvement of downshifting during regenerative braking. It is reported that energy recovery efficiency is improved up to 27.4%. Some studies suggested new control algorithms that ensure high energy efficiency and safety under various road conditions targeting safety-critical driving situations [32,33]. Other relevant studies include multi-objective optimization considering battery aging [34,35], low-speed cutoff detection [36], and motor and hydraulic braking coordination [37]. All the aforementioned technologies are valuable to ultimately solve the range anxiety issue. Meanwhile, it is also necessary to evaluate the impact of the technologies to the driving range with an adequate and efficient simulation model. However, only limited studies have been reported on the driving range estimation model for EVs by a system design approach. Chau and Wong [38] studied for power management in hybrid electric vehicles (HEV), and delineated the trends of HEVs and EVs. Banjac et al. [39] developed power loss model for plug-in hybrid-electric vehicle (PHEV) based on the efficiency map data, and noted

that the efficiency of energy conversion has a significant influence to electric energy depletion. Silva et al. [40] developed a power consumption model using utility factor to calculate energy consumption for PHEV, and represented the PHEV utilization prices for some centuries. Katrasnik [41] suggested analytical framework for energy conversion efficiency of different hybrid electric vehicle topologies. The researcher also developed energy conversion model, and revealed energy conversion phenomena of PHEV [42]. Gao et al. [43] generated a simple eco-driving model, and applied the distinctive driving profile to the developed simulation model. Since most of the previously developed models have been system perspective approaches with efficiency-map basement for each electric component, the electric power transfer and conversion process have not been developed or reflected in the simulation model in minute detail. Besides, there was a limit in determining how much the various types of heat loss generated by PEEM and ESS affect the mileage reduction of electric vehicles. To analyze the effect of the loss occurring in PEEM and ESS on the mileage, an integrated model that can quantitatively predict the electrical energy conversion and transfer between PEEM and ESS, calculating the thermal loss from them. In this study, a sequential approach with electric current based power transfer and loss model is developed to estimate the amount of electric power transfer and loss from PEEM and ESS for various driving

conditions and its operating temperature respectively with ambient temperature.

1.2.2 Cabin thermal management system

For the ICE vehicles, the air-conditioning system had a role to cool-down the cabin space for summer using the vapor compression refrigeration system. Enough thermal energy from the ICE is supplied to the cabin space to warm-up the indoor air for the winter season. However, in battery electric vehicle that does not have sufficient waste heat from the combustion engine, HVAC system is required to have functions not only cabin and battery cooling in summer, but also warm-up the temperature of the cabin air. Fig 1.4 shows the most representative heat pump system for battery electric vehicles. The PTC heater located at the down flow of indoor condenser supply additional heating capacity when the heat pump system cannot supply enough thermal energy to the cabin. In the case of a heat pump system that have two roles both cooling and heating of the vehicle interior, various research has been conducted to reduce the cooling or heating load. Zhang et al. [44] proposed a heat pump system for EVs with a desiccant-coated heat exchanger minimizing the dehumidify load for the cold fresh air. Zhang et al [45] also proposed a concept of applying a continuous anti-fogging air curtain for front windshield glass. In winter, the difference between the temperature of the indoor air and the ambient air is greater than

that of the summer. Therefore, due to the required heating load, vehicle mileage reduction is more severe than that of cabin cooling mode. The heat pump system has a disadvantage when it operates at cold and humid air. This condition can lead to a significant drop in heating performance and efficiency dramatically. Research has been conducted to overcome these operating conditions. Research on heat pumps for indoor heating of electric vehicles in winter has been carried out two way, vapor-injection heat pump system and waste heat recovery. Ahn et al. [46] did a experimental research to verify the performance of dual-evaporator heat pump system for dehumidifying and heating of a cabin. Choi et al. [47] designed a vapor-injection cycle for low temperature heating purposes. They showed the optimal injecting port position of the compressor. Ahn et al. [48] conducted an experiment to figure out the heating performance effect of a dual source heat pump using air and water waste heat. Han et al. [49] conducted simulation and experimental research for the vapor-injection heat pump system using waste heat recovery. Tian et al. [50] the electric vehicle thermal management system (EVTMS) performances under various conditions have been studied from the perspective of thermodynamic and thermo-economic view. Most of the previous studies have focused on either cooling or heating mode to improve the performance of air conditioners or heat pumps, or to increase its efficiency. Besides, to produce sufficient heating

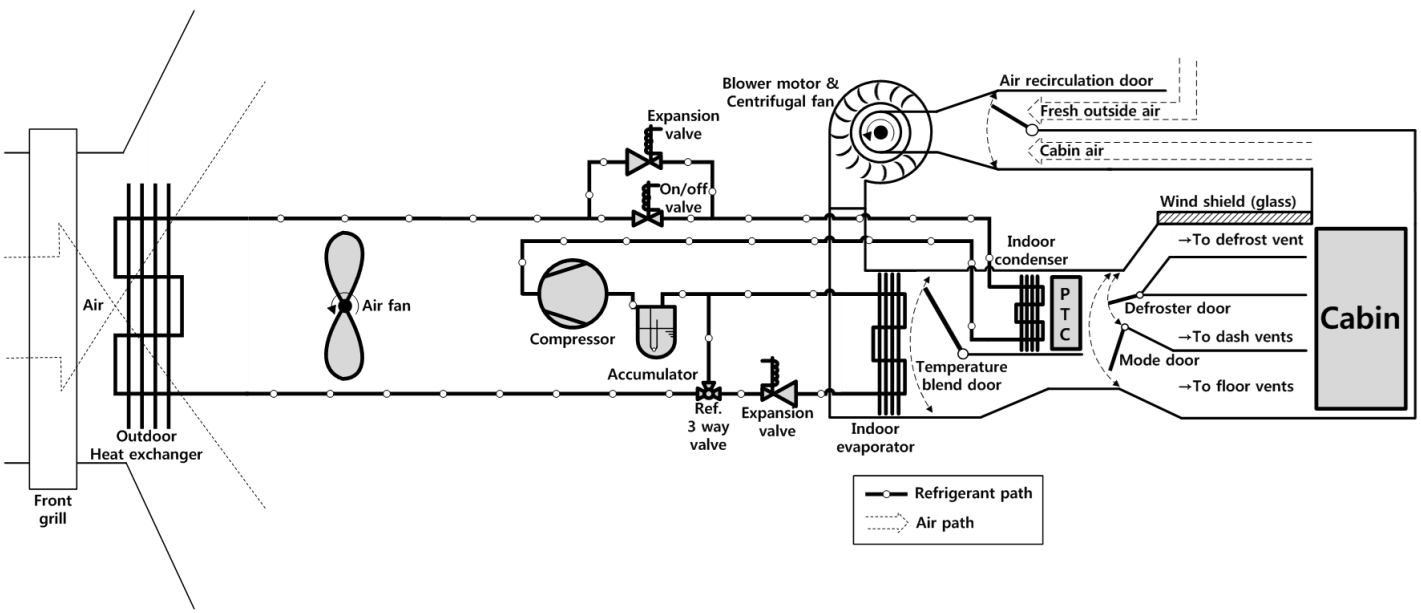

Fig. 1.4 Cabin thermal management system for battery electric vehicles
(3-heat exchangers type with PTC heater)

capacity in winter, waste heat recovery strategy is actively used, or vapor-injection heat pump technology has been developed. In summary, in order to increase the efficiency of the cabin thermal management system, which is greatly affected by solar heat flux, indoor and outdoor air temperature, and humidity, as well as the size of the heat exchangers (outdoor, indoor), it is necessary to attempt a macroscopic design approach from the vehicle point of view rather than seeking to increase efficiency by limiting to the cabin thermal management system itself.

1.3 Objectives and scopes

In order to design an efficient integrated thermal management system, the system design perspective needs to be expanded to the vehicle scale to increase the thermal linkage between electric powertrain (EPT) and cabin thermal management system (heat pump). In order to design an integrated thermal management system, it is essential to investigate thermal loads required from both the EPT and cabin, respectively, under several driving conditions and outdoor conditions.

The chapter 2 shows integrated electric power transfer and loss model - electric current based - development for the electric powertrain (EPT), i.e., energy storage system, power electronics, and electric machine. In addition, in

order to estimate the thermal load from the vehicle cabin, a cabin model is developed based on the thermal comfort. Through the simulation research of these models, the thermal load from EPT and cabin are estimated. Based on the calculated results, it is presented in the integrated electric vehicle thermal management system (IEVTMS) design concept from the wholescale point of view.

The chapter 3 presents the numerical and experimental results for the proposed IEVTMS. To design the IEVTMS, numerical research for the heat pump system is conducted resulting the cooling and heating capacity, and COP. There is assumption that the PEEM and ESS have cooling system based on the liquid as coolant. A coolant cooling system ranging from radiator, indoor heater core also developed. In order to compare the power reduction of the IEVTMS, a baseline system is also conducted. According to the ISO 15042, 2017, multiple split-system air conditioners and air-to-air heat pumps, for various ambient condition ranging from -7ºC to 46ºC, experiment for steady-state air to air heat pump system were conducted mearing the heating and cooling capacity of indoor units, and power consumption from the compressor.

Finally, the chapter 4 presents effect of the proposed IEVTMS on range extension. Based on the experimental results carried out in Chapter 3, the amount of electric energy consumed in the proposed IEVTMS was

quantitatively presented. To calculate the range for a battery electric vehicle, a transient electric power transfer and loss model interlocked with the mileage calculation is developed. Therefore, in this chapter, the range extension effect of the proposed system is verified by the developed numerical model.

Chapter 2 Electric vehicle thermal loads analysis

2.1 Introduction

In order to design an efficient HVAC system, the system design perspective needs to be expanded to the vehicle scale to increase the thermal linkage between electric powertrain (EPT) and HVAC. In order to design an integrated thermal management system, it is essential to investigate thermal loads required from both the EPT and cabin, respectively, under several driving conditions and outdoor conditions.

In this study, a sequential approach with electric current base is developed to get the amount of power transfer and loss from PEEM and ESS for various driving conditions, such as constant and dynamic respectively. The vehicle under this study is a long-range, light-duty battery electric vehicle. In order to calculate the power transfer and loss for PEEM, 150 kW IPMSM is designed for an electric machine. And then, the electromagnetic field analysis is conducted. For the power electronics, a three-phase full-bridge inverter/converter is designed, and the amount of heat generation from the high-voltage power electronics is predicted by electric current-based model. The

power loss model for lithium-ion battery pack is referred to the experimental data. Those prime components for electric traction system are combined with vehicle dynamics and regenerative braking system. To estimate the state of charge (SOC) on various driving loads, the multi-component simulation model is developed. Furthermore, its results are verified with real-world on-road vehicle data. Also, in order to investigate the characteristics of electric power transfer and loss according to the dynamic driving profile, the moving average method is applied to the existing urban dynamometer driving schedule (UDDS) velocity profile generating new velocity profiles with a low acceleration-deceleration rate.

2.2 Design a light-duty battery electric vehicle

As mentioned above, to design an efficient HVAC system, it is necessary to analyze the EPT in detail because the heating and cooling system for a cabin must increase the linkage with the electric vehicle power train. Unlike conventional vehicles which use internal combustion engine (ICE) and mechanical transmission gear for propulsion, electric powertrain for battery electric vehicles are composed of lithium-ion battery packs, power electronics (PE), and electric machine (EM); for example, electric motor, as shown in Fig. 2.1. The power flow diagram introduces components that have

representativeness for the BEV. The purpose of EPT is to convert electrical energy into kinetic energy of a vehicle or to store kinetic energy generated by a vehicle as electric energy. When the vehicle accelerates or drives at a constant speed, the electric energy transfer from the battery pack to the motor control unit (MCU). The MCU converts direct current (DC) to alternative current (AC), and supplies the converted electric energy to the electric machine. In the process of transferring and converting the energy, losses are continuously generated, and these losses occur in the form of heat. When the vehicle decelerates, the interaction between the hydraulic brake and the regenerative braking brake varies depending on the effect on deceleration. When a driver slows down the vehicle, the kinetic energy can be converted into electrical energy through the regenerative braking brake and stored in the battery pack. When there is rapid deceleration, the intervention of the hydraulic brake is increased. Even in all cases, the energy transfer and loss phenomenon continuously occurs. The electric energy for both driving and the HVAC system is supplied from the energy storage system (ESS). Therefore, if the compressor for HVAC consumes a lot of electric energy, the electric energy stored in the ESS is rapidly reduced, which means a reduction in mileage. Since the PTC required for indoor heating connects to a high voltage battery pack, it is advantageous to suppress the use of PTC heater in order to increase the driving distance of the vehicle. For the

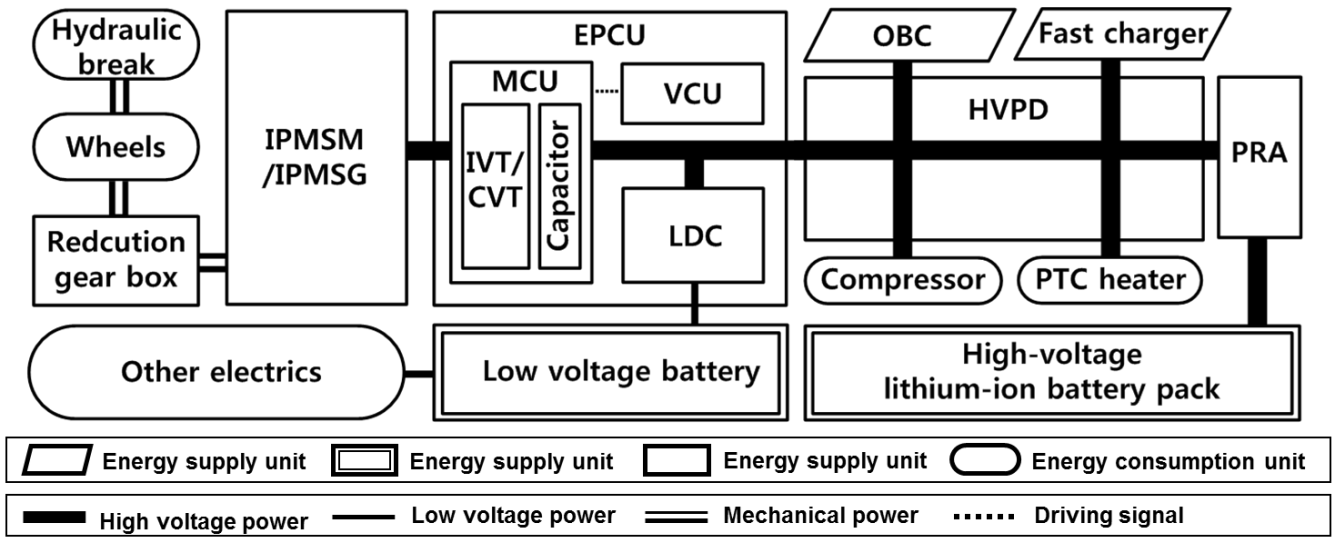

Fig. 2.1 Topology with power path for battery electric vehicle

quantitative design of EPT, the selection of the target vehicle must be preceded. Light-duty vehicles are the most in demand, and they are relatively easy to convert to electric vehicles because of their relatively lightweight. Therefore, in this study, the light-duty vehicle with realistic performance was selected as shown in Table 2.1, and the capacity of the energy storage system (ESS), electric machine (EM), and power electronics (PE) are selected to meet the requirements.

2.2.1 Design an energy storage system

A large number of comprehensive studies for BEV have been carried out in diverse aspects to extend the driving range; component development, system design, and driving control strategy. As for the component, energy storage system (ESS), and power electronics and electric machine (PEEM) are essential components of the electric traction system. NMC lithium-ion batteries were selected as energy storage devices for electric vehicles. In general, the energy density of an electrochemical battery is determined by the theoretical electrical capacity of the cathode. The theoretical electric capacity of the garden electrode is defined with the following equation [51]:

$$C_{theorical} = \frac{nF}{3.6\,M}\ [\mathrm{mAh/g}] \tag{2.1}$$

Table 2.1 Design parameters for a light-duty battery electric vehicle

Parameter	Value	Unit
Range on a single charge	400	km
Maximum velocity	165	km/h
Time (0 – 100 km/h)	7.0	s
Weight of vehicle without ESS	1420	kg
Maximum payload	450	kg
GVWR*	2100	kg
Rolling resistance coefficient	0.02	[-]
Frontal area	2.42	[m^2]
Rim and tire radius	0.33	[m]
Gear reduction ratio	7.98	[-]
Coefficient of drag	0.32	[-]
Cabin volume	2.8	m^3

*GVWR: gross vehicle weight rating [kg]

where, M is molar weight of material (lithium cobalt oxide: 97.87 g/mol), n is number of reactive electrons per formula unit (n: 0.4~1), and F is the Faraday constant (96,485 C/mol). In case of $LiCoO_2$, the theoretical electric capacity is about 137 mAh/g, and 166 mAh/g for $LiNi_{0.6}Mn_{0.2}CO_{0.2}O_2$. To design the total amount of energy that can satisfy various driving conditions, six representative driving modes provided by EPA were selected as shown in Fig 2.2. The characteristics of the six typical driving modes are indicated in the Table 2.2. When dividing the driving cycle by the average speed, NYCC is the lowest, HWFET and US06 are divided into the highest group, and UDDS, SC03, and FTP can be divided into medium speed. In order to calculate the required energy per each driving cycle, vehicle dynamics equations are applied and its results it is shown in Figure 2.3. It was found that the energy efficiency was better in the city driving mode, and the efficiency was reduced as the speed increased. The reason is that in the case of the city driving mode, since the kinetic energy of the vehicle can be converted into electric energy and stored when the vehicle decelerates, it shows a relatively high efficiency compared to the high-speed driving. The mileage of an electric vehicle is closely related to the weight of the vehicle. In addition, the weight of lithium-ion batteries has a significant effect on the weight of the vehicle. In order to comprehensively examine the proper weight, energy capacity, and mileage distance, the vehicle mileage distance was

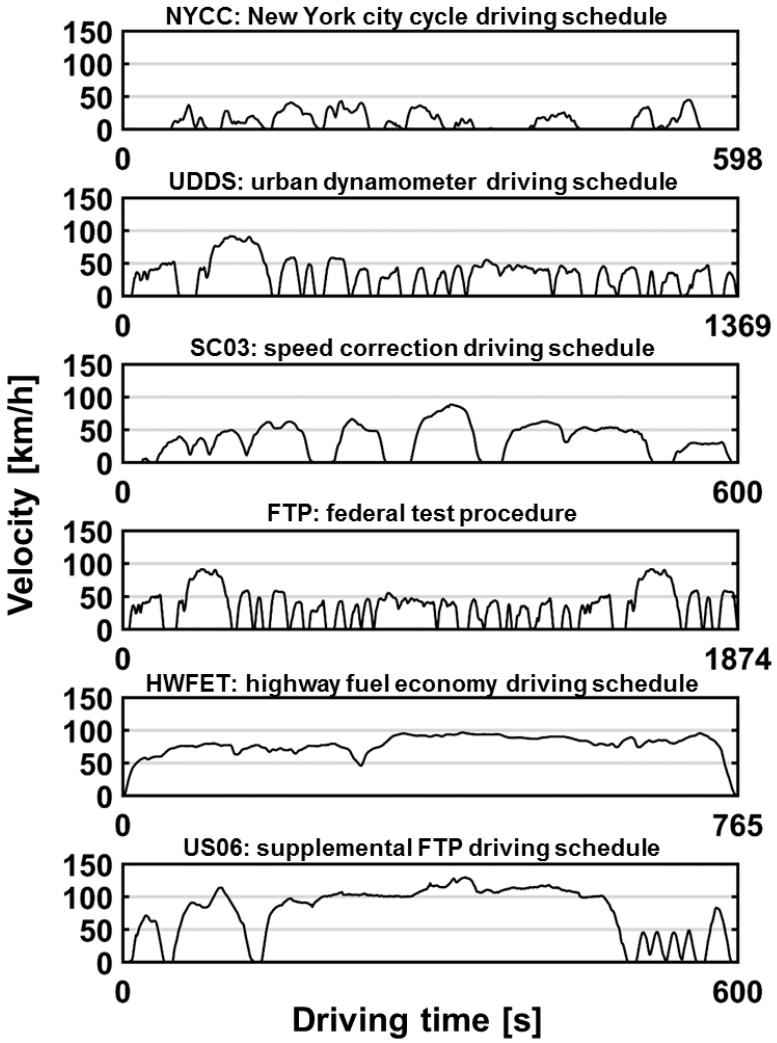

Fig. 2.2 Various driving cycles for light-duty vehicles

Table 2.2 Representative parameters for various driving cycles

Parameters		NYCC	UDDS	SC03	FTP	HWFET	US06
Time	[s]	598	1369	600	1874	765	600
	[min]	10.0	22.8	10.0	31.2	12.8	10.0
Distance	[km]	1.9	12.0	5.8	17.8	16.5	12.9
Maximum	[km/h]	44.6	91.3	88.2	91.3	96.4	129.2
Average velocity	[km/h]	11.4	31.5	34.5	34.1	77.6	77.2
Range efficiency	[km/kWh]	8.8	7.7	7.6	7.5	6.0	4.9

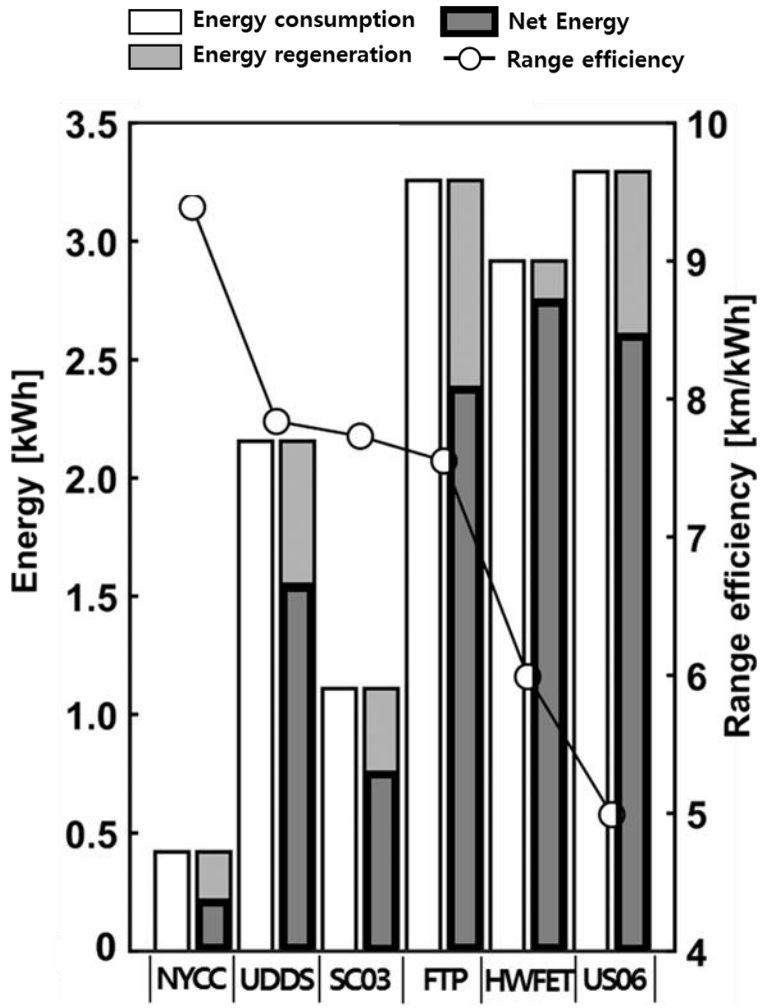

Fig. 2.3 Energy and range efficiency for single driving cycle

simulated for various driving conditions while increasing the number of cells as shown in Fig 2.4, considering the specific energy of NMC lithium-ion battery is about 227 Wh/kg and its mechanical density, 2700 kg/m^3. As a result, the intersection of the efficiency curve and the distance curve appeared at about 300 battery cells. Therefore, 300 battery cells were selected. On the other hand, when the vehicle is driven dynamically, the battery is discharged as well as charging through regenerative braking system. In order to confirm the C-rate of the battery unit cell, the dynamic variation of the C-rate was confirmed combining the vehicle dynamic model with the battery electric model. In this simulation, there is no power loss for PEEM and ESS. Two driving cycles (UDDS, US06) were considered at low and high driving load, respectively. As a result, shown in Fig 2.5, under the low driving load condition, it was about 1 C-rate for both discharge and charge state, and under high driving load condition, the discharge rate was about 1.5, and charge rate was about 1C. Since the acceleration is greater than the deceleration in most driving cycles, the discharge C-rate is greater than the charge C-rate. If these driving characteristics of an electric vehicle are applied to battery cell development, a more efficient battery cell can be developed after calculating the optimum C-rate according to the development target vehicle.

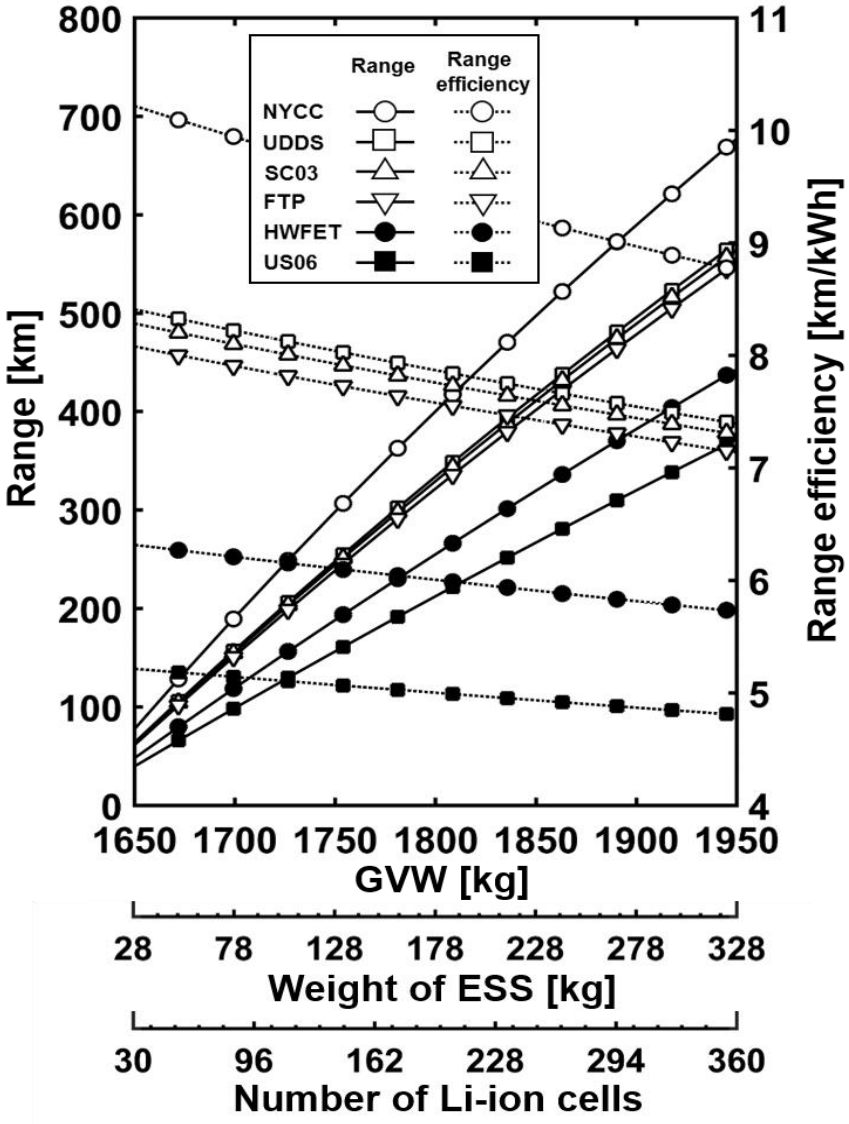

Fig. 2.4 Electric capacity design for ESS

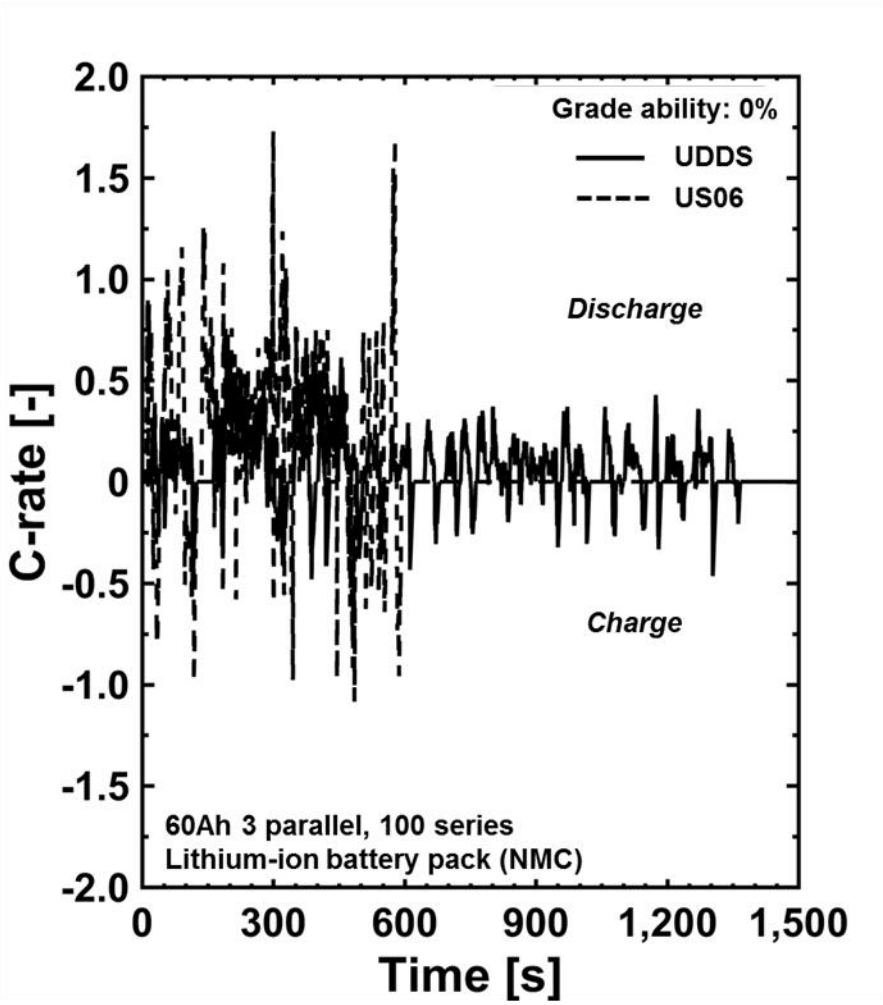

Fig. 2.5 Dynamic variation of C-rate for single cell

2.2.2 Design an electric machine

Not only ESS, but also PEEM can also affect the performance and mileage of electric vehicles. To increase the performance of PEEM, an interior permanent magnet synchronous motor (IPMSM) is receiving the most attention. Different types of motors have been studied for increasing the energy density and efficiency of electric machines. Axial flux permanent magnet machine (AFPMM), synchronous reluctance machine (SynRM), and permanent magnet assisted SynRM (PMa-SynRM) are the promising power traction motor for electric vehicles. Motor performance is related to vehicle torque and speed. First, in order to calculate the maximum torque required by the vehicle, simple vehicle dynamics equations presented in Eqns. (2.1) - (2.4) are used. The target time for 0-100 km/h is 7 sec. To satisfy the target time the required maximum torque for the IPMSM is 350 Nm as shown in Fig 2.6 (a) and (b). Also, the maximum torque should be maintained up to about 4000 rpm, and the maximum power of the motor was selected as 150 kW shown in from Fig 2.7. Electric machine is a component that make up a system (electric vehicle). Since the motor capacity must satisfy the required performance of the system, it is necessary to select the motor capacity after selecting the load condition that the system requires the most.

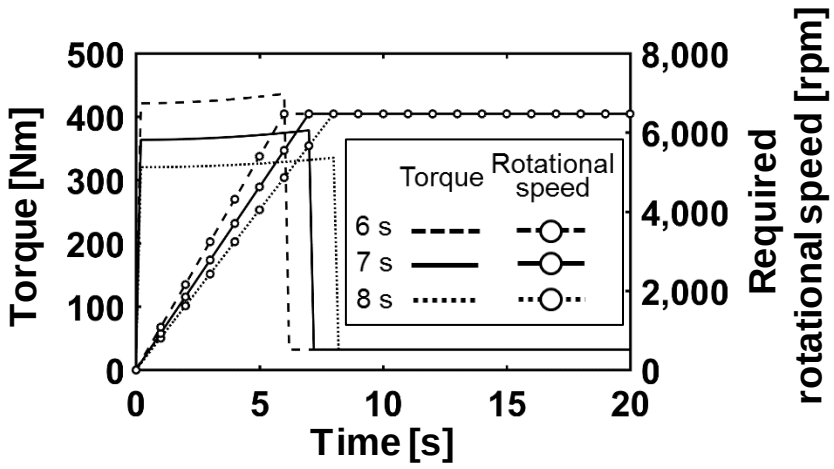

(a) Required torque and rpm for electric machine

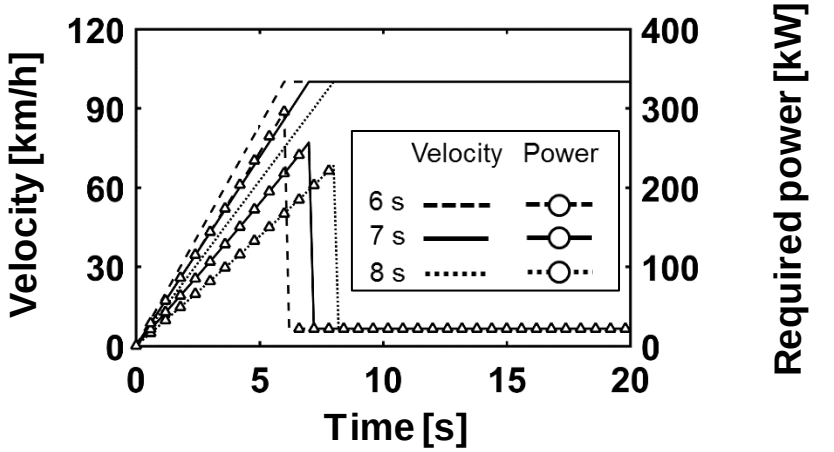

(b) Vehicle velocity and required power for electric machine

Figure 2.6 Requirement performance of electric machine

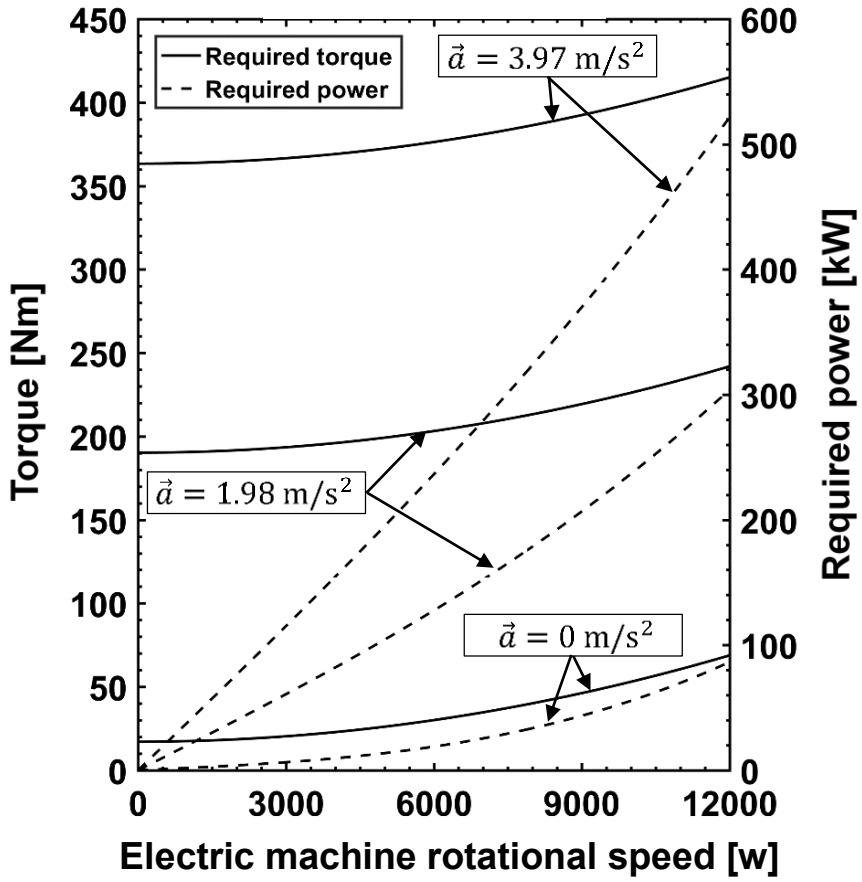

Figure 2.7 Demand of load curve of a light-duty electric vehicle

2.2.3 Design a cabin

In order to simulate the cabin thermal load of the vehicle, a cabin model suitable for a light duty electric vehicle (LDBEV) was constructed. The radiant energy flowing from outside of the vehicle, the number of passengers, and the heat capacity of the interior materials were considered. Thermal comfort that satisfies both summer and winter was selected as 0. The criterion for the thermal comfort is follow the Eq. (2.2) from ASHRAE HANDBOOK, 2017, FUNDAMENTALS. Cabin interior space was appropriately selected for LDBEV. All design parameters are presented in the Table 2.3.

$$\text{Thermal sensation (Y)} = 0.252\, T_{air,\ drybulb} + 0.24 \cdot P_{air,\ watervatpor} - 6.859 \qquad (2.2)$$

2.3 Electric powertrain thermal loads

2.3.1 Numerical model description

Unlike conventional vehicles with internal combustion engine (ICE) and weighty, complicated transmission, powertrain for battery electric vehicles are composed of energy storage system (ESS); for example, lithium-ion battery pack, power electronics (PE); for example, motor control unit (MCU), and electric machine (EM); for example, electric motor. The developed numerical

model focuses on electric-driven system, ESS, MCU, and EM. In order to calculate driving power transfer and losses at constant and dynamic driving load conditions, integrated power transfer and loss model is developed with vehicle dynamics considering parallel regenerative braking system.

2.3.2 Vehicle dynamics

A long-range light-duty battery electric vehicle is considered as a target vehicle. Specific vehicle parameters are shown in Table 1. The required power and torque for driving are calculated by vehicle dynamics as presented in Eqns. (2.3) - (2.6).

$$\sum \mathrm{F}_v = \mathrm{F}_d - \left(\mathrm{F}_{rr} + \mathrm{F}_g + \mathrm{F}_a\right) \tag{2.3}$$

$$\mathrm{F}_d = m_v \frac{dv}{dt} + \left(\mathrm{F}_{rr} + \mathrm{F}_g + \mathrm{F}_a\right) \tag{2.4}$$

where, $F_{rr} = C_{rr} m_v \vec{g} cos\theta$, $F_g = m_v \vec{g} sin\theta$, $F_a = \frac{1}{2} C_d A_f v_v^2 \rho_{air}$

$$w_{em} = w_w \xi_{rg} = \frac{v_v}{r_w} \xi_{rg} \tag{2.5}$$

$$T_{em} = \frac{F_d v_v}{w_{em}} \tag{2.6}$$

Table 2.3 Design parameters for HVAC system

Parameters	**Winter**	**Summer**
Solar heat flux	300 W/m^2	900 W/m^2
Cabin volume	2.8 m^3	
Cabin interior mass	150 kg	
Number of people	Four	
Target thermal sensation	Neutral within 30 minutes	

where, F_v is net force; F_d is the required vehicle driving force; F_r is rolling resistance; F_g is gravity force; F_a is aerodynamic force; w_{em} is required angular velocity for electric motor, and T_{em} is required torque for electric motor.

2.3.3 Power electronics and electric machine power transfer and loss model

2.3.3.1 Electric machine model

For electric vehicles, the electric machine demands both high speed and torque. IPMSM is a classic electric machine that receives electrical energy from the lithium-ion battery pack, and converts it into mechanical power through the power electronics [52]. The direct current electrical energy supplied from the high-voltage battery pack is inverted into alternating electric energy through the three-phase full-bridge inverter, and the inverter supplies the alternating current (AC) power to each phase for the IPMSM. On the contrary, when the IPMSM operates as a generator (IPMSG), the AC power is converted to direct current (DC) power to supplying electric energy to the battery pack. The AC power providing IPMSM causes an electric current to flow through the insulated copper coil wound on the stator, and the alternating current periodically induces the electromagnetic field interacting with the permanent

magnet to generate torque and power. The general voltage equations of IPMSM [53] are expressed as

$$V_d = R_{ser} i_d + \frac{d\psi_d}{dt} - w_e \psi_q = R_{ser} i_d + L_d \frac{di_d}{dt} - w_e (L_q i_q) \tag{2.7}$$

$$V_q = R_{ser} i_q + \frac{d\psi_q}{dt} + w_e \psi_d = R_{ser} i_q + L_q \frac{di_q}{dt} + w_e (L_d i_d + \psi_f) \tag{2.8}$$

where,

$$\psi_d = L_d i_d + \psi_f \tag{2.9}$$

$$\psi_q = L_q i_q \tag{2.10}$$

$$\psi_f = \frac{V_q - R_{ser} i_q - \frac{d\psi_q}{dt}}{w_e} - \psi_q \tag{2.11}$$

with R_{ser} as stator coil electric resistance, and i_d and i_q as d- and q-axis currents, L_d and L_q as d- and q-axis inductances, respectively. ψ_d, ψ_q, and ψ_f are the magnetic flux linkage for d-, q-axis, and permanent magnets, respectively. w_e is the electrical angular frequency. The electromagnetic torque for IPMSM [54] is expressed as in Eq. (2.12).

$$T_{em} = \frac{3}{2}\frac{P}{2}\{\psi_f i_q + (L_d - L_q) i_d i_q\} \quad (2.12)$$

where P is the number of poles. The first term in the right-hand side of Eq. (2.12) represents reaction torque due to interaction between permanent magnet flux density (ψ_f) and q-axis current (i_q), and the second term denotes reluctance torque resulting from the inductance difference, ($L_d - L_q$). For the light-duty electric vehicle, a 150 kW IPMSM is designed as shown in Fig. 2.8, and the design parameters are presented in Table 2.4. In order to satisfy the requirement of maximum torque and angular velocity for the light-duty electric vehicle, 8 poles, double layer and V-shaped configuration were applied to permanent magnet design [55]. The 48 slots and paralleled distributed winding method with Y-connection are also applied to the stator winding minimizing the power loss for the IPMSM. Combining vehicle information, arbitrary driving profile, and vehicle dynamics, the required torque and angular velocity for IPMSM are calculated. In order to calculate electric current and voltage satisfying the required torque and angular speed, it is necessary to conduct that electromagnetic analysis for the designed power electronics (PE). FluxMotor 2018 (Altair) [56] is applied to calculate the electromagnetic field analysis. For the numerical approach, the direct current voltage is assumed at 400 V identical to the lithium-ion battery pack, and the desired maximum angular velocity is

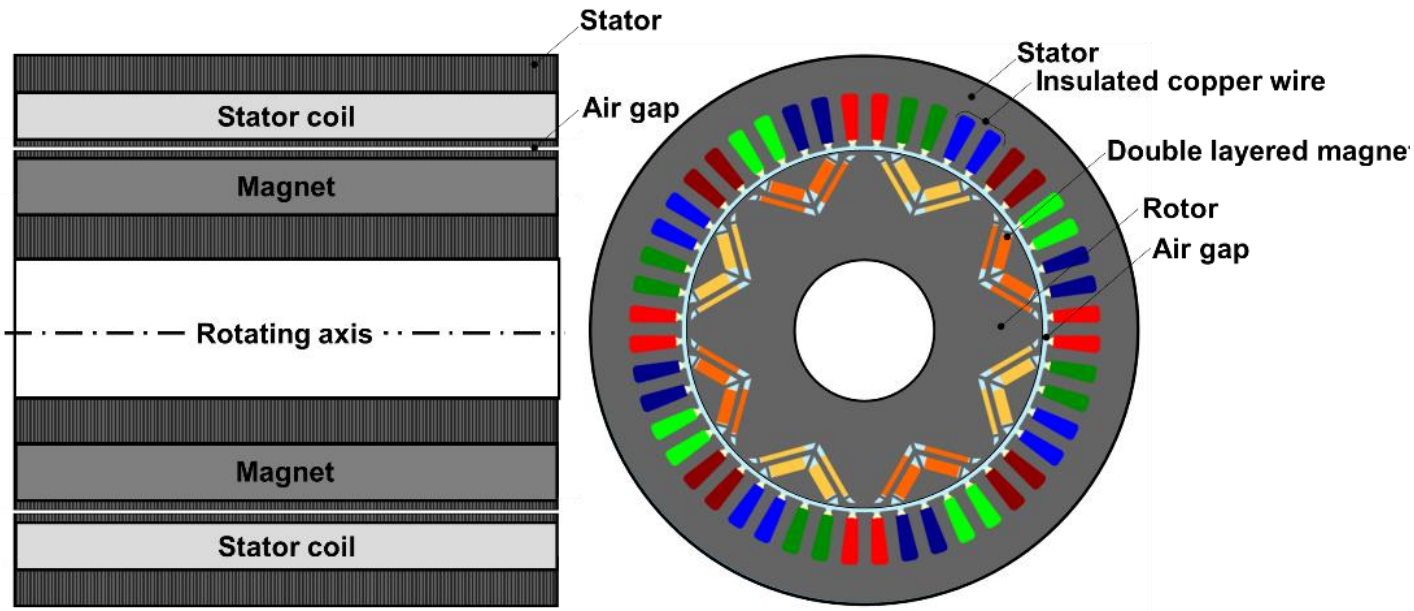

Fig. 2.8 Design for 150 kW interior permanent magnet synchronous motor

(8 poles, 48 slots, double layer and V-shaped permanent magnet configuration)

Table 2.4 Design parameters of IPMSM

	Parameters	Values	Units
Stator	Slot	48	[-]
	Stator diameter	200	mm
	Stator length	175	mm
	Stator material	M330_35A	[-]
	Winding turn	10	[-]
	Winding parallel path	4	[-]
	Winding connection	Y connection	[-]
	Line resistance	0.015 (at 20℃)	[Ω]
	Wire diameter	1	mm
Rotor	Rotor diameter	50	mm
	Rotor length	175	mm
	Rotor material	M330_35A	[-]
	Number of poles	8	[-]
	Magnet material	NdFeB_1320_1400	[-]
	Magnet placement	V-Shape	[-]
	Magnet flux density	1.32 (at 20℃)	[T]
Air gap	Thickness	0.97	[mm]

11,000 rpm. The representative results for electromagnetic analysis for the IPMSM are summarized in Fig. 2.9 and Fig. 2.10. In general, unlike surface-mounted permanent magnet synchronous motor (SPMSM), IPMSM have magnetic saliency causing the inductance unbalancing ($L_q > L_d$). Fig. 2.9 shows the inductance [H] field for d- and q-axis phase current values (RMS), and the magnetic saliency, which is a dominant factor for inductance torque, is prominently featured. Fig. 2.10 represents the flux linkage [Wb] field for the d- and q-axis RMS. The flux linkage for individual axes intertwined with magnetic toque is independent to a certain extent for d- and q-axis RMS. From Eq. (2.12), there are a myriad of combinations of i_d, i_q to generate equal magnitudes of torque. Therefore, an operating strategy for IPMSM needs to take into account motor characteristics. Maximum torque per ampere (MTPA) speed control method has been widely applied to IPMSM in a constant torque region [57,58], and it follows the current and voltage constraints as follows;

$$i_d^2 + i_q^2 \leq i_{s,max}^2 \tag{2.13}$$

$$V_d^2 + V_q^2 \leq V_{s,max}^2 \tag{2.14}$$

where, $i_{s,max}$ is the peak value of the maximum stator current, and $V_{s,max}$ is

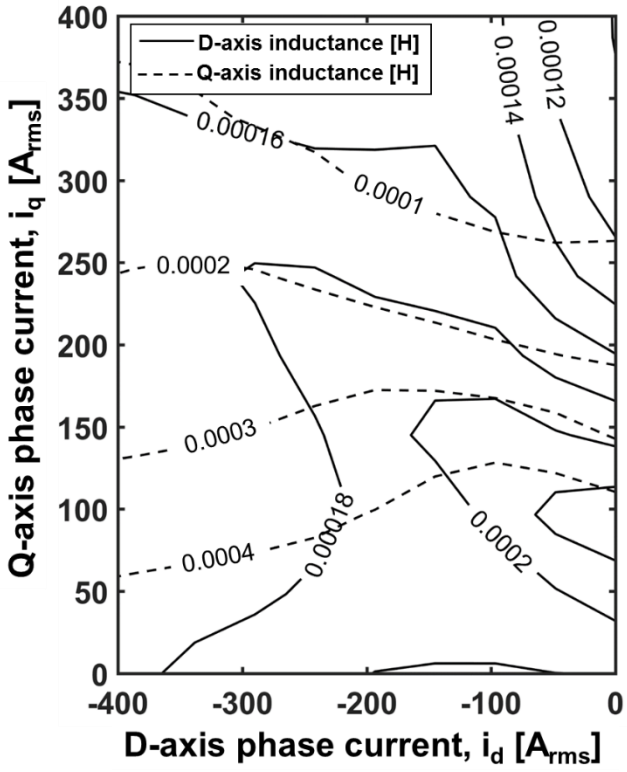

Fig. 2.9 Electromagnetic analysis results for inductance field

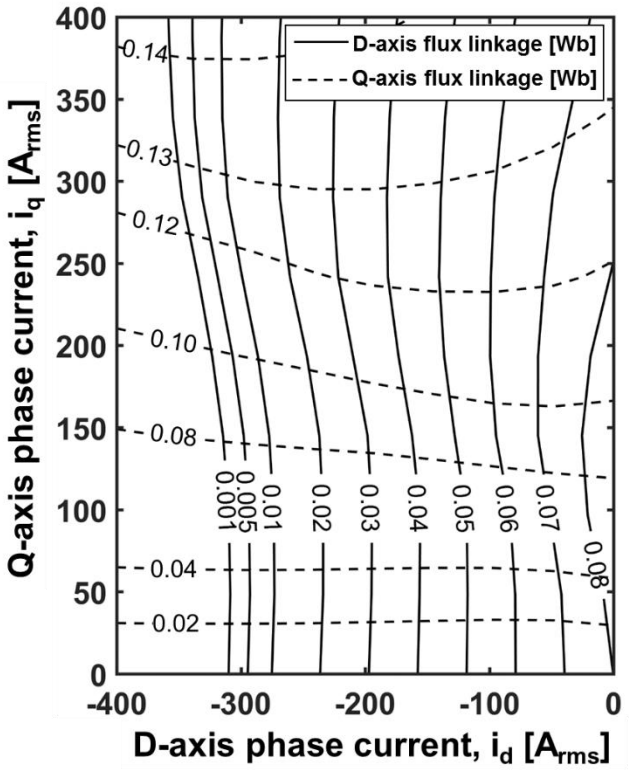

Fig. 2.10 Electromagnetic analysis results for flux linkage field

the peak voltage value of the maximum phase voltage. Eq. (2.15) represents the relationship between i_d and i_s when the MPTA control mode is working.

$$i_d = \frac{-\psi_f + \sqrt{{\psi_f}^2 + 8\left(L_d - L_q\right)^2 i_s^2}}{4\left(L_d - L_q\right)} \tag{2.15}$$

On the other hand, the flux-weakening strategy based on controlling d-axis stator current applied to middle speed operating zone ($\omega_{em} > \omega_{em,base}$) [59, 60]. When the IPMSM operating in the very high-speed region ($\omega_{em} \gg \omega_{em,base}$), maximum torque per voltage (MTPV) is carried out in flux weakening operation to increase the motor speed further [61, 62]. The flux-weakening control method represents as follows;

$$i_d = \frac{-\psi_f + \sqrt{{\psi_f}^2 + 8\left(L_d - L_q\right)^2 i_s^2}}{4\left(L_d - L_q\right)} \tag{2.16}$$

$$(\omega_{em} L_q I_q)^2 + (\omega_{em} L_d I_d + \omega_{em} \psi_f)^2 \leq {V_{s,max}}^2 \tag{2.17}$$

$$V_{s,max} = \frac{V_{dc}}{\sqrt{3}} \tag{2.18}$$

Fig. 2.11 represents the performance curve and control strategy considering the coalescence of electromagnetic features ranging from electric torque, current,

voltage to angular velocity referred to Eq. (2.15) - (2.18). The current limit circle, voltage limit ellipse, and constant torque curve on d–q axes with the performance curve are shown in Fig. 2.12. It is required to meet the electromagnetic characteristics of the designed motor that MPTA is applied to constant torque region (region I) generating maximum torque performance. For region II and III, flux weakening control strategy is applied due to high back electromotive force (BEMF). Consequently, the required driving power based on the current and voltage is calculated from Eq. (2.19) and (2.21).

$$i_{u,v,w} = i_s \cos\left(w_e t + \tan^{-1}\left(\frac{i_q}{i_d}\right) + \phi_p\right) \tag{2.19}$$

$$\phi_p = -\frac{2\pi}{3}, 0, \frac{2\pi}{3} \tag{2.20}$$

$$V_{u,v,w} = R_{ser} i_{u,v,w} + L_{u,v,w} \frac{di_{u,v,w}}{dt} + e_{u,v,w} \tag{2.21}$$

with $e_{u,v,w}$ is back electromotive force for u, v, and w phase, respectively.

As a result, through the development of power transfer model for EM, it is possible to calculate not only the drive power but also the power loss from the IPMSM. During the power conversion process, current flows through the copper wire causing heat loss (Joule heating). At the same time, due to the

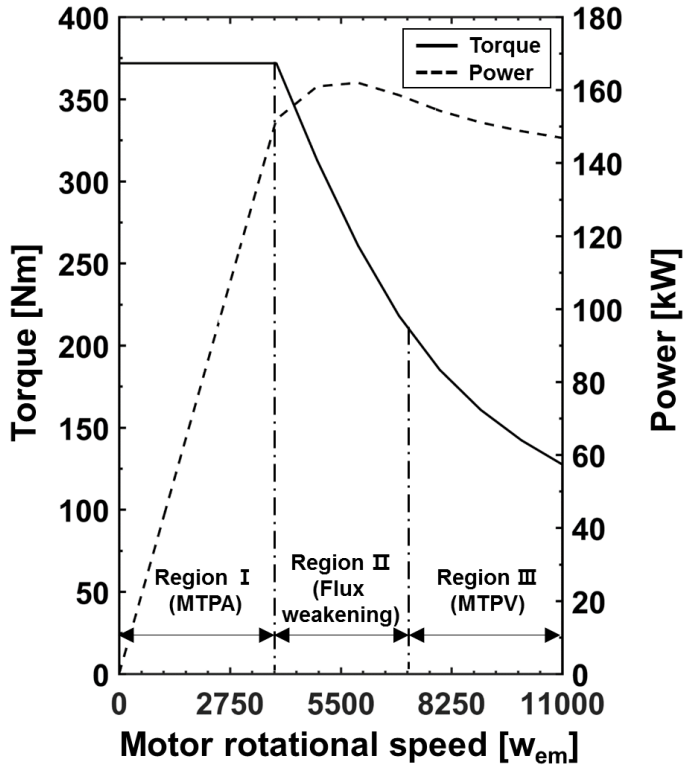

Fig. 2.11 Control strategy for interior permanent synchronous motor

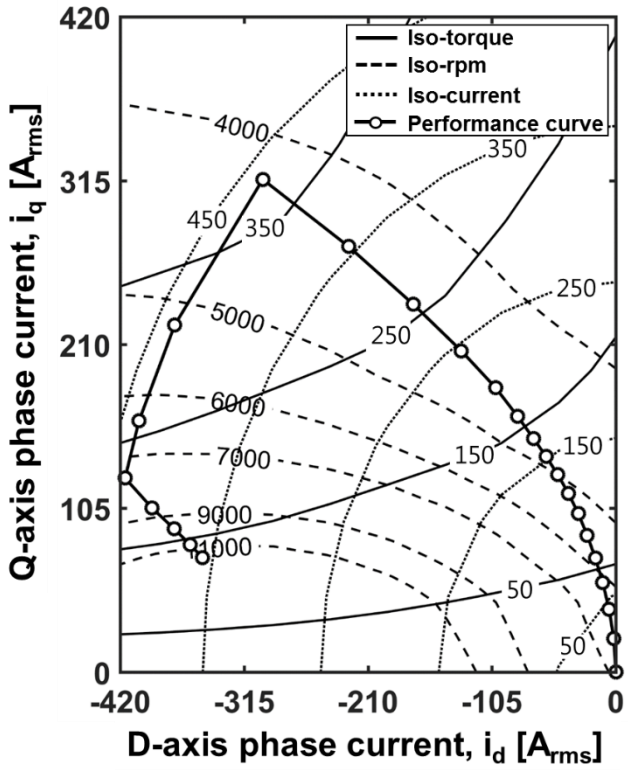

Fig. 2.12 Performance curve for interior permanent synchronous motor

rotating magnetic field, iron loss occurs in the stator and the rotating shaft. In addition, the mechanical power loss during the power transfer process is also inevitable. The amount of Joule loss is determined by the strength of the electric current and the specific resistance of the copper wire, the most widely used as electric conductor. It tends to increase its specific thermal resistance with temperature, and thus, the higher the temperature of the copper, the greater the heat generation rate per unit volume for the same electric current. The appropriate copper wire temperature is assumed, $T_{em,coil} = 373$ K, based on the on-road vehicle data and the previous studies in thermal management system for IPMSM [63,64]. The Joule loss is calculated by Eq. (2.22) and (2.23).

$$\dot{Q}_{em,Joule} = 3R_{em,coil}{i^2}_{rms} = \frac{3}{2}R_{em,coil}(i_d^2 + i_q^2) \tag{2.22}$$

$$R_{ser} = r_{coil}(1 + \alpha_{em,coil}T_{em,coil})\frac{L_{em,coil}}{A_{em,coil}} \tag{2.23}$$

with r_{coil} as specific resistance of the copper coil, $\alpha_{em,coil}$ as temperature coefficient of resistance for the copper coil, $L_{em,coil}$ as the total length of copper coil, $A_{em,coil}$ as the cross-section area of copper coil.

Iron loss, on the other hand, is known to be affected primarily by the strength of the electromagnetic force and the rotational speed of the magnetic

field rather than by the temperature of stator [65]. The iron loss is calculated by Eqs. (2.22) and (2.23).

$$\dot{Q}_{em,eddy} = \frac{k_e(f)D}{2\pi^2}\int_{Iron}\frac{1}{N}\sum_{k=1}^{N}\left\{\left(\frac{B_r^{k+1}-B_r^k}{\Delta t}\right)^2 + \left(\frac{B_\theta^{k+1}-B_\theta^k}{\Delta t}\right)^2\right\}dv \tag{2.24}$$

$$\dot{Q}_{em,hysteresis} = \frac{k_h(f)D}{T}\sum_{i=1}^{NE}\frac{\Delta V_i}{2}\left(\sum_{j=1}^{N_{pr}^i}\left(B_{mr}^{ij}\right)^2 + \sum_{j=1}^{N_{p\theta}^i}\left(B_{m\theta}^{ij}\right)^2\right) \tag{2.25}$$

Eq. (2.24) and (2.25) can be simplified as presented in Eq. (2.26).

$$\begin{aligned}\dot{Q}_{em,iron} &= \dot{Q}_{em,eddy} + \dot{Q}_{em,hysteresis} \\ &= k_h B_{max}^{\beta} w_m + k_e B_{max}^2 {w_m}^2\end{aligned} \tag{2.26}$$

For the mechanical loss Eq. (2.27) is applied to the model

$$\dot{Q}_{em,mech} = k_{em,mech} w_{em}^2 \tag{2.27}$$

$$k_{em,mech} = \alpha_1 \left(w_{em,rpm}^2\right) + \alpha_2 \left(w_{em,rpm}\right) + \alpha_3 \tag{2.28}$$

where $\alpha_1, \alpha_2, \; and \; \alpha_3$ are -1×10^{-11}, 4×10^{-7}, and 6×10^{-5}.

As a result of the electromagnetic analysis, the amount of iron loss varying with required angular velocity and torque is represented in Fig. 2.13. Finally, by combining the various variables considered above, the total amount of power loss and demanding drive power for the IPMSM are presented in Eq. (2.29) and (2.30).

$$\dot{Q}_{em} = \dot{Q}_{em,Joule} + \dot{Q}_{em,iron} + \dot{Q}_{em,mech} \tag{2.29}$$

$$\begin{aligned} P_{em,drive} &= P_{drive} + \dot{Q}_{em} \\ &= P_{drive} + \dot{Q}_{em,Joule} + \dot{Q}_{em,iron} + \dot{Q}_{em,mech} \end{aligned} \tag{2.30}$$

2.3.3.2 Power electronics model

For an electric vehicle, the power electronics (inverter and converter), which is an electric energy conversion device that converts DC electrical energy into AC energy or vice versa, consists of insulated gate bipolar transistors (IGBTs) and diodes as shown in Fig 2.14. The IGBT is a power semiconductor device working as an electronic switch with the advantage of high efficiency

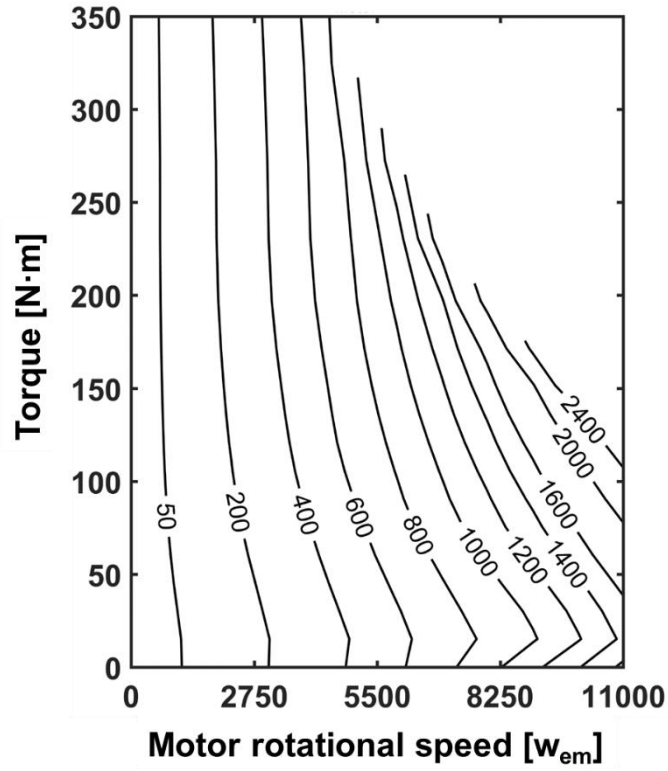

Fig. 2.13 Iron loss analysis for 150 kW interior permanent magnet synchronous motor

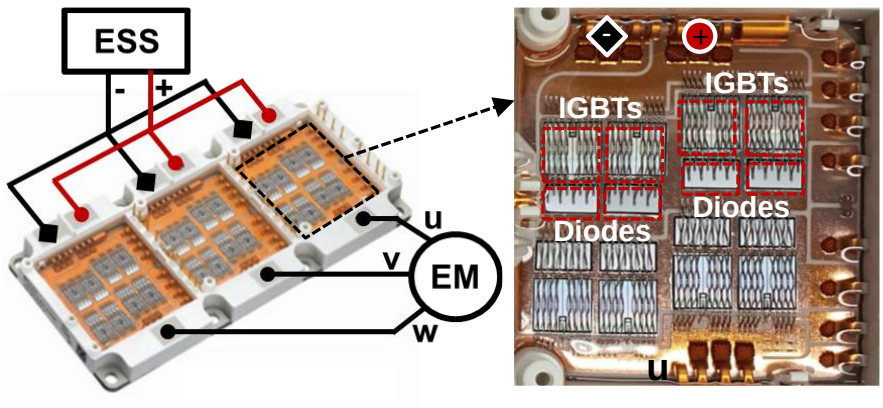

Fig. 2.14 Power electronics 150kW (Infineon, Germany)

and fast switching, and it works under the external voltage (gate voltage). The diode allows the electric current to flow in only one intended direction and to block the flow in the opposite direction. The power loss for power electronics (PE) depends on the magnitude of current, switching frequency, and temperature of the IGBTs and diodes [66, 67, 68]. In recent years, the power semiconductors made of silicon have been applied to electric vehicles for low switching frequency and high voltage electric power transfer. The IGBTs and diodes, like copper wire, play a role in letting current flow, which inevitably causes to electric power loss while DC power is inverted to AC power and vice versa. Each time the IGBT operates, intervals occur in which the current (I_{IGBT}) and voltage (V_{IGBT}) are concurrently non-zero. Those non-zero sections are divided into three zones, turn-on switching zone, conduction zone, and turn-off switching zone in consecutive order. The switching losses are generated when turn-on and -off (switching loss) processes, and for conduction loss occurs on conducting zone. Similar to the IGBTs habit, the diodes also have conducting and switching characteristics. During the diode turns on, the voltage drop for the diode can generate heat. When the device turns off, the diode generates heat loss called due to the reverse recovery time [66]. However, IGBTs and diodes that make up the inverter/converter show different characteristics compared to conductors such as copper, lead, and aluminum. For the IGBT and diode,

conduction and switching loss are not just proportional to temperature. In the case of conduction loss for IGBT, below the critical current, the heat loss and its temperature are inversely related to each other. On the other hand, above the critical current, IGBTs temperature and its conduction loss are proportional. For conduction loss in the diode, the higher the operating temperature the greater the loss regardless of the critical current value. In the case of switching loss for IGBT and the reverse recovery loss for diode, the losses increase with temperature. The characteristics of the power loss for the power electronics are indicated in Fig. 2.15. Fig. 2.15 (a) shows the IGBT conduction loss and switching loss. Fig. 2.15 (b) shows the diode conduction and switching loss. In order to get the current magnitude through the PE, the required current simulated from the EM part are used.

$$\dot{Q}_{pe,conduction,IGBT} = \frac{{I_{pe}}^2 r_{IGBT}}{8} + \frac{I_{pe} \cdot V_{CE}}{2\pi} + M \cdot \cos(\varphi) \cdot \left(\frac{{I_{pe}}^2 r_{IGBT}}{3\pi} + \frac{I_{pe} \cdot V_{CE}}{8} \right) \quad (2.31)$$

$$\dot{Q}_{pe,conduction,diode}$$

$$= \frac{{I_{pe}}^2 r_{diode}}{8} + \frac{I_{pe} \cdot V_F}{2\pi} - M \cdot \cos(\varphi) \cdot \left(\frac{{I_{pe}}^2 r_{diode}}{3\pi} + \frac{I_{pe} \cdot V_F}{8} \right) \tag{2.32}$$

$$\dot{Q}_{pe,switching,IGBT}$$

$$= \frac{1}{\pi} \times f_{SW} \times (E_{ON}[I_{NOM}, V_{NOM}] E_{OFF}[I_{NOM}, V_{NOM}]) \times \frac{I_{pe}}{I_{NOM}} \times \frac{V_{DC}}{V_{NOM}} \tag{2.33}$$

$$\dot{Q}_{pe,switching,diode}$$

$$= \frac{1}{\pi} \times f_{SW} \times E_{REC}[I_{NOM}] \times \left(\frac{I_{pe}}{I_{NOM}} \right) \times \frac{V_{DC}}{V_{NOM}} \tag{2.34}$$

The total amount of power loss for inverter/converter presented in Eq. (2.35).

$$\dot{Q}_{pe,conduction,IGBT}$$

$$= \frac{{I_{pe}}^2 r_{IGBT}}{8} + \frac{I_{pe} \cdot V_{CE}}{2\pi} + M \cdot cos(\varphi) \cdot \left(\frac{{I_{pe}}^2 r_{IGBT}}{3\pi} + \frac{I_{pe} \cdot V_{CE}}{8} \right) \tag{2.35}$$

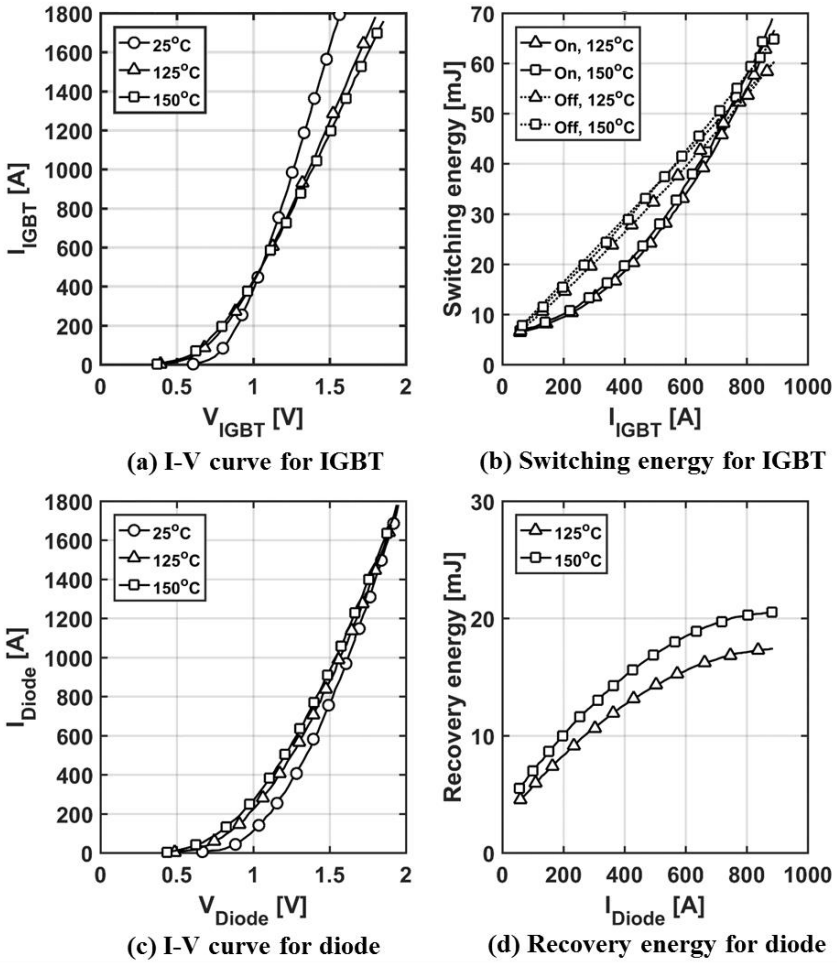

Fig. 2.15 Characteristics of IGBT and diode power loss

2.3.4 Lithium-ion battery power transfer and loss model

This study adopted a commercial pouch-type lithium polymer cell of a 60 Ah capacity with NMC (Nickel-Manganite-Cobalt) cathode and graphite anode is adopted as a battery cell. It is accepted that heat generation of the lithium-ion cell occurs with two factors; the irreversible heat from the internal resistance of the cell, and the reversible heat by the entropy change. Total heat generation is defined as the following equation [69,70].

$$\dot{Q}_{ess} = \dot{Q}_{ess,irr} + \dot{Q}_{ess,rev} = I(E - V) + IT\frac{dE}{dT} = I^2R - T\Delta S\frac{I}{nF} \quad (2.36)$$

Based on the preliminary experiment results from Hosseinzadeh et al. [71], the equation for open circuit voltage of the cell is presented as

$$OCV_{25℃} = (0.7223)SOC^3 - (0.6175)SOC^2 + (0.6201)SOC^1 + 0.34824 \quad (2.37)$$

Especially for the internal resistance, the experimental correlation is presented as Fig 2.16. From experimental results from Hosseinzadeh et al. [71], the internal resistance according to the state of the charge at various C-rate

including charging and discharging is represented in Fig 2.16. In addition, the experimental results from Lyu et al. [72] are used to reflect the temperature effect to the internal resistance. As a result, 3 dimensional internal resistance map considering the temperature, C-rate, charging/discharging, and SOC is proposed as shown in Fig 2.17. This graph shows the characteristics of the internal resistance of the battery for most operating conditions in the system from a vehicle dynamics perspective. In the same temperature condition, it can be seen that the internal resistance is higher in the low current region. This is because activation loss dominates at low currents density. In addition, entropy change ΔS of the target cell is obtained by Visvanathan et al. [70]. Polynomial correlation between the entropy change and SOC is presented as follows.

$$\begin{aligned}\Delta S = {} & (1.49 \cdot 10^3)SOC^5 - (4.37 \cdot 10^3)SOC^4 + (4.96 \cdot 10^3)SOC^3 \\ & -(2.72 \cdot 10^3)SOC^2 + (7.15 \cdot 10^2)SOC + (6.59 \cdot 10^1)\end{aligned} \tag{2.38}$$

2.3.5 Regenerative braking system model

A regenerative braking system (RBS) is also an essential part of motor technologies. Employing the electric motor as a generator, RBS allows kinetic energy to be recycled rather than to dissipate the energy as heat. Recent studies

are focusing on the control optimization of a regenerative braking system. A regenerative braking system is an imperative technique for electric vehicles (EVs). EVs almost always have better driving efficiency in urban driving than on highways due to this power recovery system. Generally, the regenerative braking system is classified into serial and parallel braking system. In serial type, either hydraulic or electric brake is selected and operated according to the required braking power. While in the case of the parallel type, the complementary braking systems are used simultaneously by dividing the required braking torque appropriately. In this study, the parallel regenerative braking system is adopted to convert part of the total frictional braking power into electrical energy while using the IPMSM as a generator. This model is developed by considering the battery SOC, required deceleration force, braking torque ratio between front and rear wheels, and maximum torque. The net power from RBS is defined as Eq. (2.39).

$$\begin{aligned} P_{em,regen} &= P_{regen} - \dot{Q}_{em} \\ &= P_{regen} - \left(\dot{Q}_{em,Joule} + \dot{Q}_{em,iron} + \dot{Q}_{em,mech}\right) \end{aligned} \tag{2.39}$$

Because thermal loss occurs even in the process of regenerative braking, a part

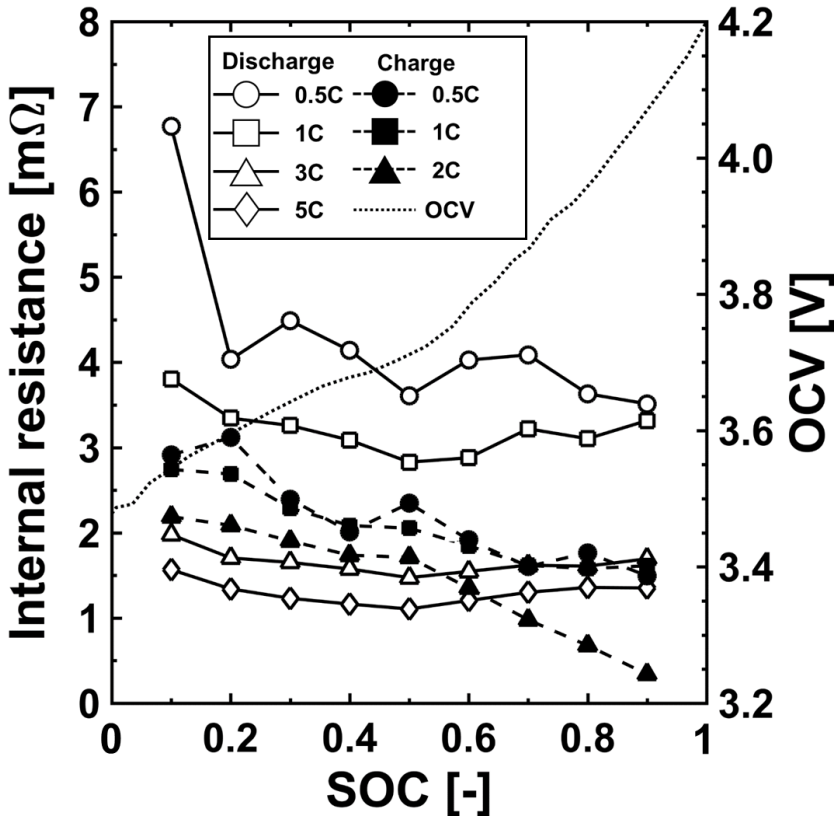

Fig. 2.16 NMC lithium-ion battery internal resistance and OCV at 25ºC

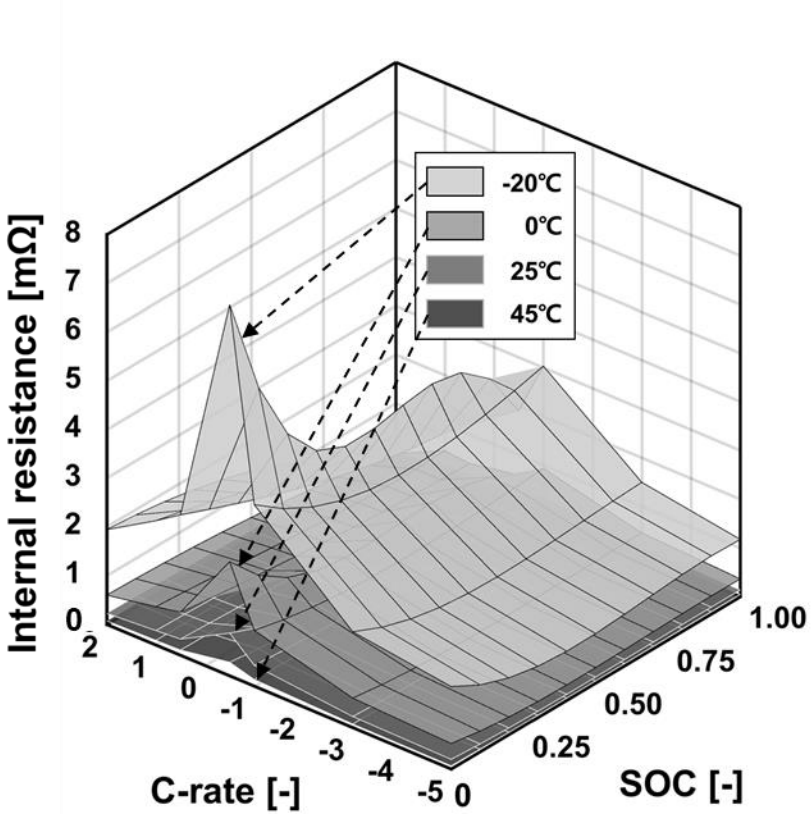

Fig. 2.17 Internal resistance estimation of NMC lithium-ion battery for various operating conditions

of the electric power recovered by the electric machine is considered to be lost as a heat generation (thermal energy). Fig. 2.18 shows the flow chart of parallel regenerative braking system model. The required braking torque is divided into 0.8:0.2 for frontal and rear, respectively.

2.3.6 Integrated power transfer and loss model

Vehicle dynamics, PEEM and battery electric power model, and parallel regenerative braking system are combined into a dynamic BEV power transfer and loss model. Fig. 2.19 describes the flow chart of the developed integrated power transfer and loss model considering the regenerative braking system. Most of the other researchers who predicted the mileage of electric vehicles chose the map-based loss model when calculating the loss of the components. However, since the prime cause of the heat loss occurring in the components is the magnitude of the current, in this study, a current-based integrated heat loss prediction model was developed. When the speed profile enters into the model, the model calculates the driving load of the vehicle and then predicts the required electric power in real-time. The vehicle information ranging from GVWR and coefficient of drag for the vehicle should be considered at this time. The gradeability, which has a great impact on the driving load, was also considered as an input variable. In the integrated power and loss model, the

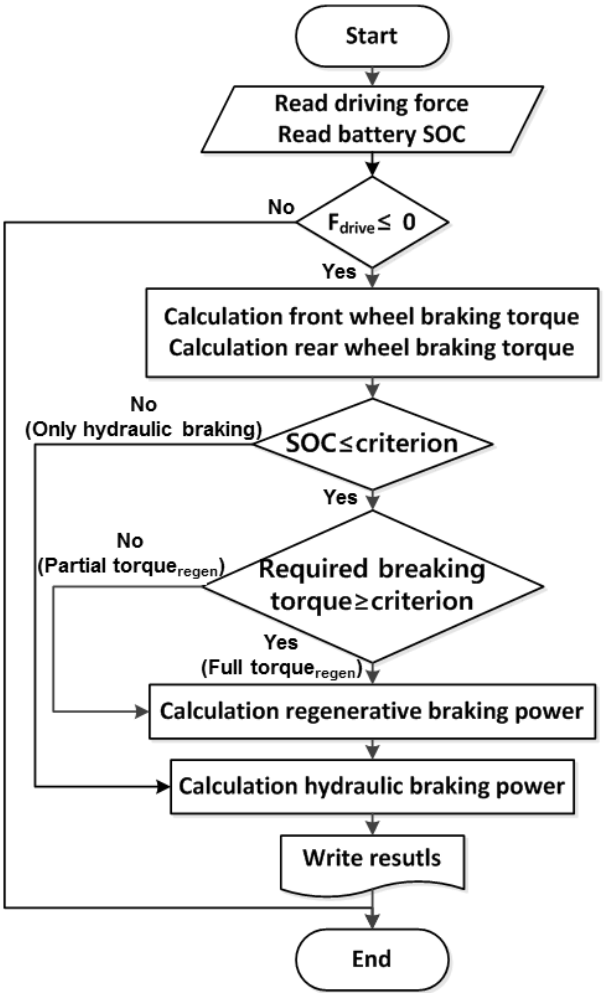

Fig. 2.18 Simulation flow chart of the regenerative braking system

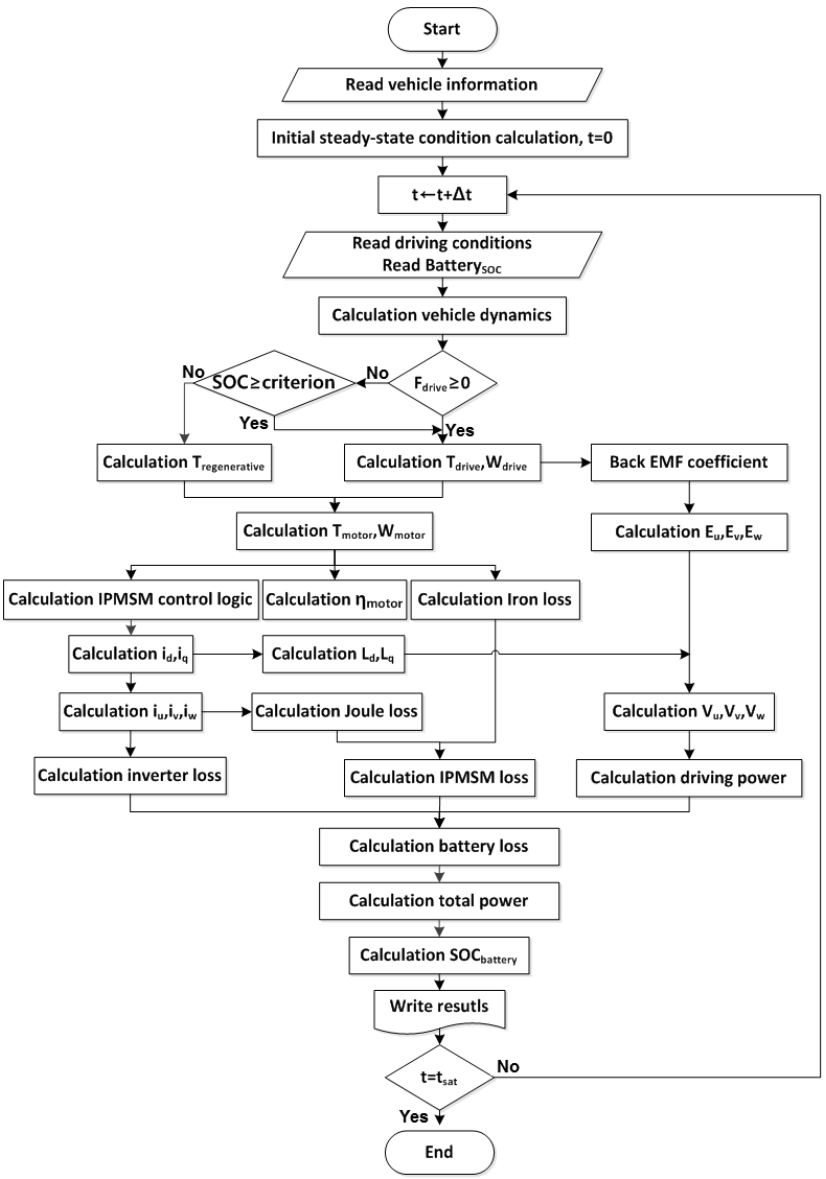

Fig. 2.19 Flow chart of integrated power loss model with the regenerative braking system

amount of heat generated by each element is mainly determined by the magnitude of the current and the internal resistance. However, the internal resistance of each component is a function of temperature and changes with temperature. In this algorithm, it is assumed that the temperature of each part has a constant temperature difference from the outside temperature through a proper liquid cooling based thermal management system. The total power from the battery pack is estimated, considering not only the driving power but also its losses from PEEM and ESS.

2.4 Cabin thermal load

2.4.1 Numerical model description

The cabin thermal management system of vehicles is essential for the thermal comfort of a driver and passengers. In particular, the interior surface of the vehicle is mostly made of glass to gain visibility, and thus solar heat flux can affect the indoor temperature variation. Besides, exceptionally, when the interiors such as seats, dashboards, and other useful gadgets temperature are soaked similar to the outdoors, even higher, the cabin thermal load is required to be larger due to the interiors having a relatively large heat capacity compared to that of the air. In this study, a cabin for light-duty vehicle is designed, and the parameters of it is shown in Table 2.5. Based on the research results from

Table 2.5 Design parameters for cabin

Parameters		Warm-up and heating	Pull-down and cooling
Vehicle surface area		16.04	
Cabin volume		2.8 m^3	
Cabin interior	Mass	150 kg	
	Specific heat	1500 J/kgK	
	Convective heat transfer coefficient	100 W/m^2K	
	Surface area	6.7 m^2	
Window	Area	3.04 m^2	
	Reflection effectiveness	0.313 [-]	
Number of people		4 [-]	
Solar heat flux		300 W/m^2	900 W/m^2
Degree of soaking		$T_{ambient}$+5ºC	$T_{ambient}$+15ºC
Thermal sensation[1)]		0 (Neutral)	

[1)] ASHRAE,2017, Exposure time: 2 hours, Subjects: Men and Women

Thermal sensation (Y) = $0.252 \cdot T_{air,\ drybulb} + 0.24 \cdot P_{air,\ watervatpor} - 6.859$

Huang [73], the cabin thermal load is calculated. For simplicity, the cabin sensible and latent loads are treated separately, i.e., there is one set of equations that has temperature as the main variable and another set with humidity as the main variable. However, the air properties are calculated at the corresponding temperature and humidity in each time step. Therefore, to calculate the interior temperature and relative humidity, the passenger compartment was analyzed using the lumped capacitance method. It is assumed that the temperature and humidity inside the passenger compartment is spatially uniform at any instant of time during the process. These equations for the cabin thermal load estimation are based on: dry air mass balance, vapor mass balance, interior air energy balance, and cabin interior mass energy balance. Eq. (2.40) represented the dry air mass balance.

$$\frac{dm_{air,cabin}}{dt} = \dot{m}_{air,infil} + \dot{m}_{air_{to}cabin} - \dot{m}_{air_{from}cabin} \tag{2.40}$$

The vapor mass balance equation is presented as

$$\frac{d}{dt}(mW)_{air,cabin} = \tag{2.41}$$

$$(\dot{m}W)_{air,infil} + (\dot{m}W)_{air_{to}cabin} + \dot{m}_{v,human} - (\dot{m}W)_{air_{from}cabin}$$

Eq. (2.42) represented the interior air energy balance.

$$\frac{dE_{c.v}}{dt} = \dot{E}_{in} - \dot{E}_{out} + \dot{E}_{gen} \tag{2.42}$$

The Eq. (2.42) is reconstituted as Eq. (2.42) by describing the each term for cabin thermal energy.

$$\frac{d}{dt}(mh)_{air,cabin} = \Omega\dot{Q}_{solar} + \dot{Q}_{convec} + \dot{Q}_{human} + \dot{Q}_{interior} + (\dot{m}h)_{air,infil} + (\dot{m}h)_{air_{to}cabin} - (\dot{m}h)_{air_{from}cabin} \tag{2.43}$$

From Eq. (2.43), the variation of cabin air temperature is presented as Eq. (2.44), (2.45), and (2.46) as below:

$$\frac{dT_{air,cabin}}{dt} = \frac{B - A(2501 + 1.86T_{air,cabin})}{m_{air,cabin}\,(1.006 + 1.86W_{air,cabin})} \tag{2.44}$$

where,

$$A \equiv \Big\{(\dot{m}W)_{air,infil} + (\dot{m}W)_{air_{to}cabin} + \dot{m}_{v,human} - W_{air_{from}cabin}\big(\dot{m}_{air,infil} + \dot{m}_{air_{to}cabin}\big)\Big\} \tag{2.45}$$

$$B \equiv \Omega \cdot \dot{Q}_{solar} + \dot{Q}_{convection} + \dot{Q}_{human} + \dot{Q}_{interior} + (\dot{m}h)_{air,infil} + (\dot{m}h)_{air_{to}cabin} - (\dot{m}h)_{air_{from}cabin} \tag{2.46}$$

The temperature of the interior is presented as follows the Eq. (2.47) as below:

$$\frac{dT_{interior}}{dt} = \frac{(1-\Omega)\cdot\dot{Q}_{solar} - h_{interior}A_{interior}\big(T_{interior} - T_{air,cabin}\big)}{(mc)_{interior}} \tag{2.47}$$

The variables referred at these equation above are described in Fig 2.20. The four coupled nonlinear ordinary differential equations are solved computationally. In order to verify the developed simulation results, the

experimental data from Huang's results [73] are adopted. The results is represented in Fig 2.21. For cooling conditions, the temperature of air and the relative humidity agree well with the experimental results. The root mean square error (RSME) is 2.03%, 3.39% for temperature and relative humidity respectively. And average absolute deviation error (AAD) is 1.75%, 2.04% for temperature and relative humidity respectively.

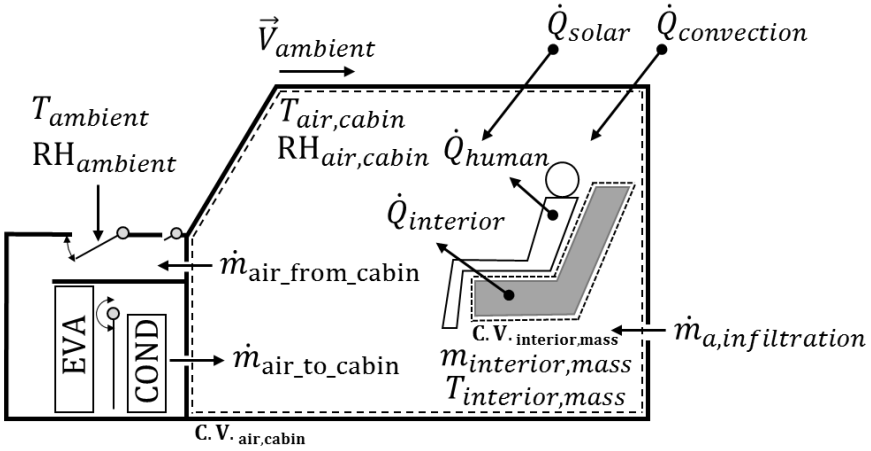

Fig. 2.20 Physical model of cabin

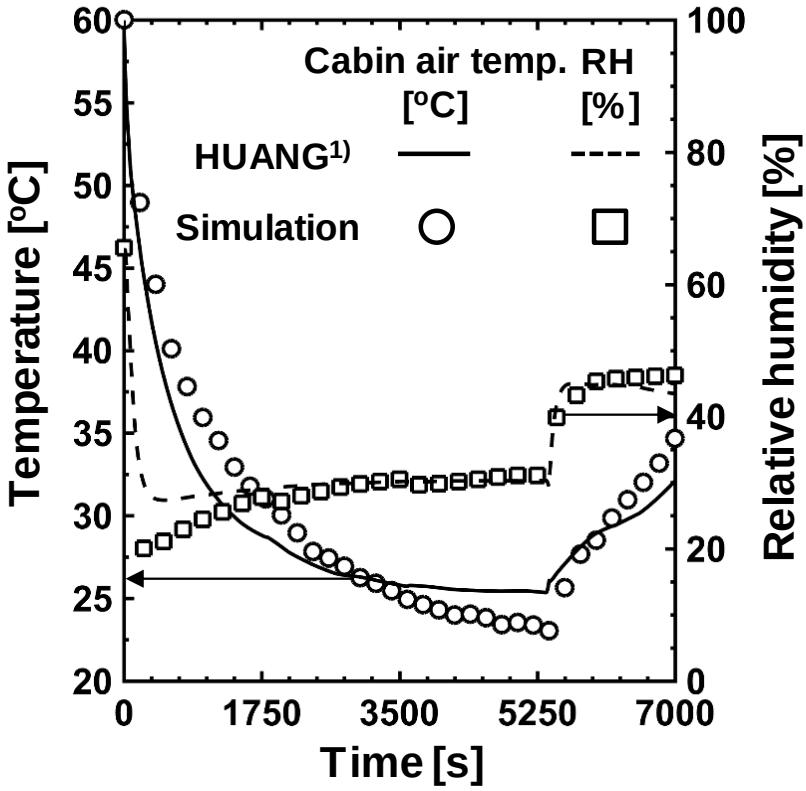

Fig. 2.21 Cabin model validation

2.5 Results and discussion

2.5.1 Electric powertrain thermal load analysis

Fig. 2.22 reveals simulation results of three constant driving load conditions. In Fig. 2.22, the pie charts on the left side represent the amount of total electric power consumption in cruise driving mode. The electric power consumption can be divided into rolling resistance, air resistance, acceleration resistance, and gradient resistance. However, there is no acceleration resistance in the constant velocity-driving mode. In the case of 140 km/h (0%), the gradient resistance is negligible because the climbing angle is zero. The pie charts on the right side represent the electric power loss for each driving condition. The generated power loss was divided into electric machine (EM), power electronics (PE), and energy storage system (ESS). The power loss for EM is calculated by dividing copper, iron, mechanical loss in detail, and electric power loss for the inverter is calculated by dividing into IGBTs and diodes. The total energy consumption is the highest at about 57 kW at 100 km/h (6%) driving mode while driving at the speed of 140 km/h (0%) and 50 km/h (8%) consumes 50.6 kW and 31.6 kW, respectively. By considering the relationship between the speed of the vehicle and the consumption of electrical energy, it can be seen that the higher the speed, the greater the energy consumed in the air resistance mostly. In this case, as

shown in Fig 2.22 (c-2 → a-2 → b-2), the influence of the speed on the electric power of the vehicle shows that the ratio of mechanical loss increases rapidly and the iron loss gradually increases. For this reason, as the speed of the vehicle increases, the magnetic field of the motor also needs to rotate quickly, which can cause the iron loss, and the frictional loss inside the motor is non-linearly proportional to the rotational speed. In contrast, as the grade ability increases, the climbing resistance naturally increases. In steep slope condition, a larger torque is required rather than a faster rotation of the motor, which increases the amount of loss affected by the electric current strength. As shown in Fig. 2.22 (b-2 → a-2 → c-2), depending on the grade ability, Joule loss from IPMSM and inverter loss for both IGBTs and diode are mostly affected. In the driving conditions where the speed of the vehicle is continually changing, electrical energy was consumed most in rolling resistance, followed by air resistance and acceleration resistance. In a combined dynamic driving condition, it is assumed that the initial SOC of the vehicle battery is 0.95, and the vehicle is set to drive the designed profile repeatedly until the battery was depleted at 50% of SOC. The simulation result shows the total energy consumption to drive the vehicle, and it is calculated to be about 60.4 kWh, of which about 8.7% is found to be the thermal energy loss. Among the thermal losses, the loss from EM is about 73% of total energy loss, and PE and ESS generated 15% and 11%

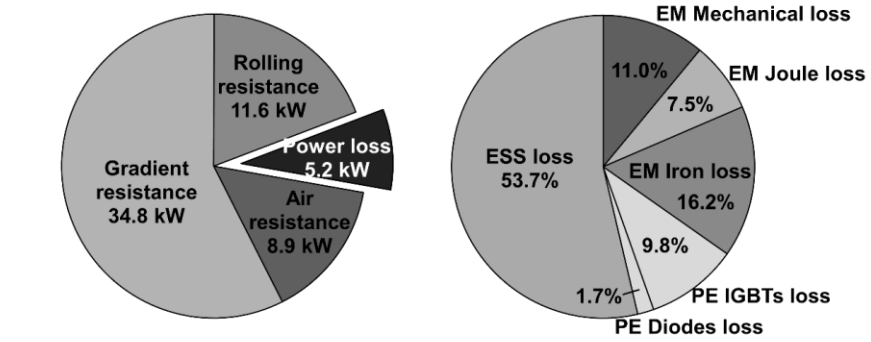

(a-1) Power consumption: 100km/h (6%) (a-2) Loss distribution: 100 km/h (6%)

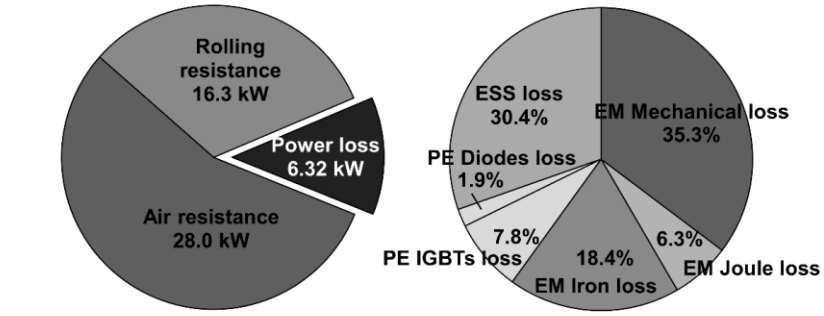

(b-1) Power consumption: 140 km/h (0%) (b-2) Loss distribution: 140 km/h (0%)

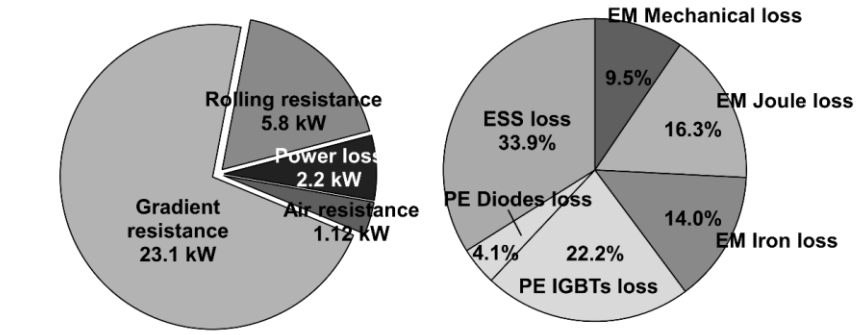

(c-1) Power consumption: 50 km/h (8%) (c-2) Loss distribution: 50 km/h (8%)

Fig. 2.22 Total power consumption and its loss distribution for constant driving modes

acceleration-deceleration pattern of the vehicle, it is possible to confirm that the heat loss from EM with various energy loss factors is greater than that of the PE and ESS in which the heat generation depends mainly on the intensity of current. The simulation results is compared with the on-road data. The torque and rotational speed from EM, and electric power at the ESS is choose as comparison variables. The transient results are agree well with the on-road experimental data. As shown in Fig 2.24, the total energy gained from regenerative braking of the motor was calculated to be about 7.4 kWh, and the loss of electrical energy in each part is small in regenerative braking mode because the total energy regenerated from the EM is less than that of total energy use for the driving mode. Although the regenerative braking mechanism produced 7.4 kWh of mechanical energy, 5.7 kWh of electric energy was estimated as net output from regenerative braking considering hydraulic brake loss, EM loss, PE loss and ESS loss.

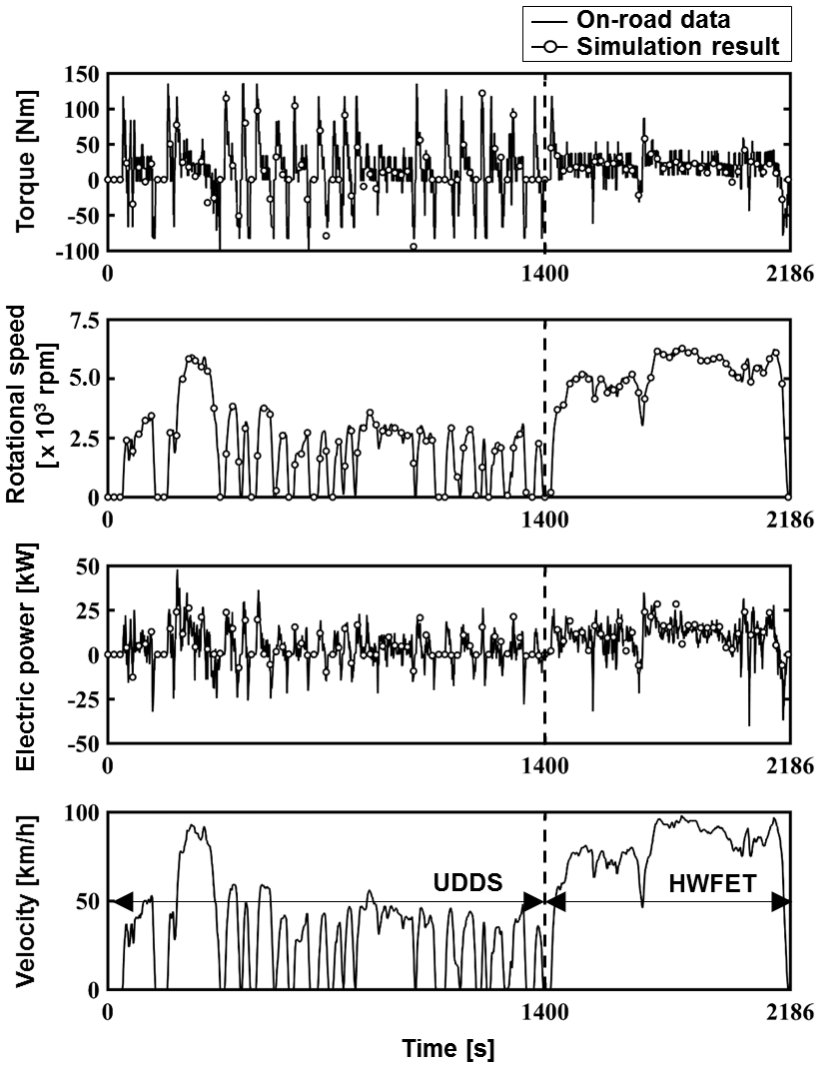

Fig. 2.23 Simulation verification for dynamic driving load condition

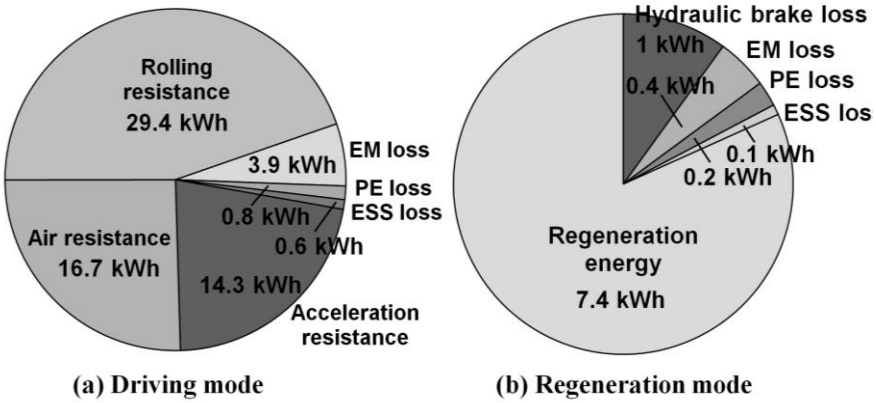

Fig. 2.24 Total energy consumption, generation and its loss distribution for dynamic driving mode (Driving cycle: UDDS + HWFET)

2.5.2 Cabin thermal load analysis

Fig. 2.25 shows the required thermal loads for thermal comfort of cabin. Using the developed cabin thermal model, the thermal load conditions required to maintain the thermal comfort of the room at 0 according to various ambient temperature conditions were calculated. The air entering the cabin was either 100% outdoor air or completely indoor circulating air. Above 20℃, it was selected to operate under cooling conditions. Looking at the heat load trend, for most outdoor temperature conditions, a higher heat load condition was required in the 100% outdoor circulation mode. The reason is that when the HVAC system is operated in the outdoor circulation mode, more energy is required to maintain indoor thermal comfort. In this study, the maximum load condition was selected as the cabin heat load condition, assuming 100% circulating mode. A numerical study was conducted to confirm the heating capacity required by the vehicle according to the change of outdoor temperature in winter. The simulation conditions for the heating capacity in winter are indicated in the Table 2.6. The soaking temperature of the cabin inside is +5ºC from the ambient air temperature. This is due to the solar heat flux which makes a temperature of cabin in side warmer then the outside. In order to calculate the maximum heating capacity, it is assumed that the 100% outside air enters into the cabin. The target thermal sensation is neutral from ASHRAE 2017. The Fig 2.25

Table 2.6 Design criteria for cabin heating system

Simulation conditions	**Warm-up & heating**
Ambient temperature (DB/WB)	-7°C / -8°C
Soaking temperature	-2°C
Solar heat flux	300 W/m^2
Cabin volume	2.8 m^3
Cabin interior mass	150 kg
Number of people	Four (1 driver and 3 passengers)
HVAC operation mode	Outside air
Vehicle profile	US06
Target thermal sensation[1)]	0 (neutral)

[1)] ASHRAE, 2017, Thermal sensation (Y) = $0.252 \cdot temp_{DB} + 0.24 \cdot P_{vp} - 6.859$

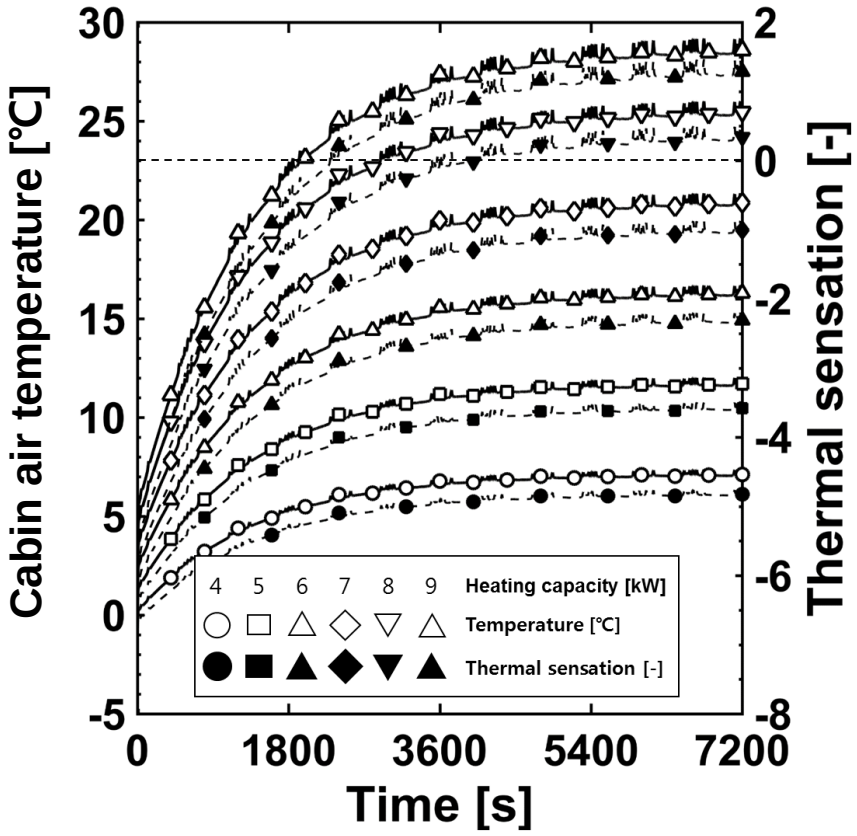

Fig. 2.25 Cabin air temperature and thermal sensation (cabin heating)

shows the temperature inside the cabin and the thermal sensation felt by the human body over time, assuming that a certain amount of heat is supplied to the room in winter. As the heating capacity increases, it can be seen that the thermal sensation approaches zero quickly, and it can be seen that about 9 kW heating capacity is required to raise the temperature inside within 1800 s properly. If the indoor thermal sensation satisfaction time is further extended, for example 3600 s, about 7.5 kW of heating capacity is required. It can be seen that the heating capacity is quite large when the vehicle is in a low-temperature thermal equilibrium state. The reason is that in order to satisfy the thermal sensation, the indoor air temperature must be raised in a short time, but it can be seen that the temperature rise time is slow due to large thermal capacity of the indoor interior that is thermally balanced at low temperature. The heating capacity of the heat pump for electric vehicles must take into account the initial cabin temperature in winter. If the performance of the heat pump does not meet the maximum heating requirements, an auxiliary heat source device, a PTC heater, must be additionally introduced to meet the thermal sensation in a short time. Numerical studies were conducted similarly to confirm not only the heating capacity but also the cooling capacity in summer. The simulation conditions for predicting cabin cooling capacity in summer are indicated in the Table 2.7. Since solar heat flux is stronger in summer compared to winter, the

indoor cabin temperature was selected as +15ºC. Fig 2.26 shows the simulation results for the cabin cooling load in the summer. As the cooling capacity increases, it can be seen that the thermal sensation approaches zero quickly, and it can be seen that about 8 kW cooling capacity is required to pull down the temperature inside within 1800 s properly. If the indoor thermal sensation satisfaction time is further extended to 3600 s, about 5.5 kW cooling capacity

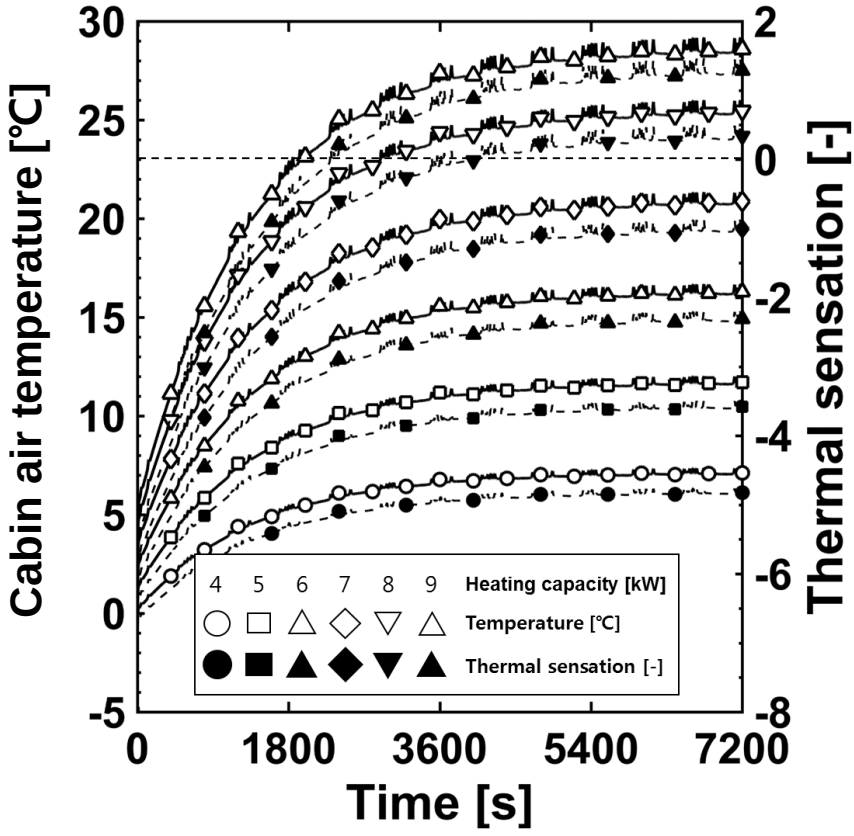

Fig. 2.25 Cabin air temperature and thermal sensation (cabin heating)

Table 2.7 Design criteria for cabin cooling system

Simulation conditions	**Pull-down & air-conditioning**
Ambient temperature[1)] (DB/WB)	46ºC / 24ºC
Soaking temperature	61ºC
Solar heat flux	900 W/m^2
Cabin volume	2.8 m^3
Cabin interior mass	150 kg
Number of people	Four (1 driver and 3 passengers)
HVAC operation mode	Outside air
Vehicle profile	US06
Target thermal sensation[1)]	0 (neutral)

[1)] ASHRAE, 2017, Thermal sensation (Y) = $0.252 \cdot temp_{DB} + 0.24 \cdot P_{vp} - 6.859$

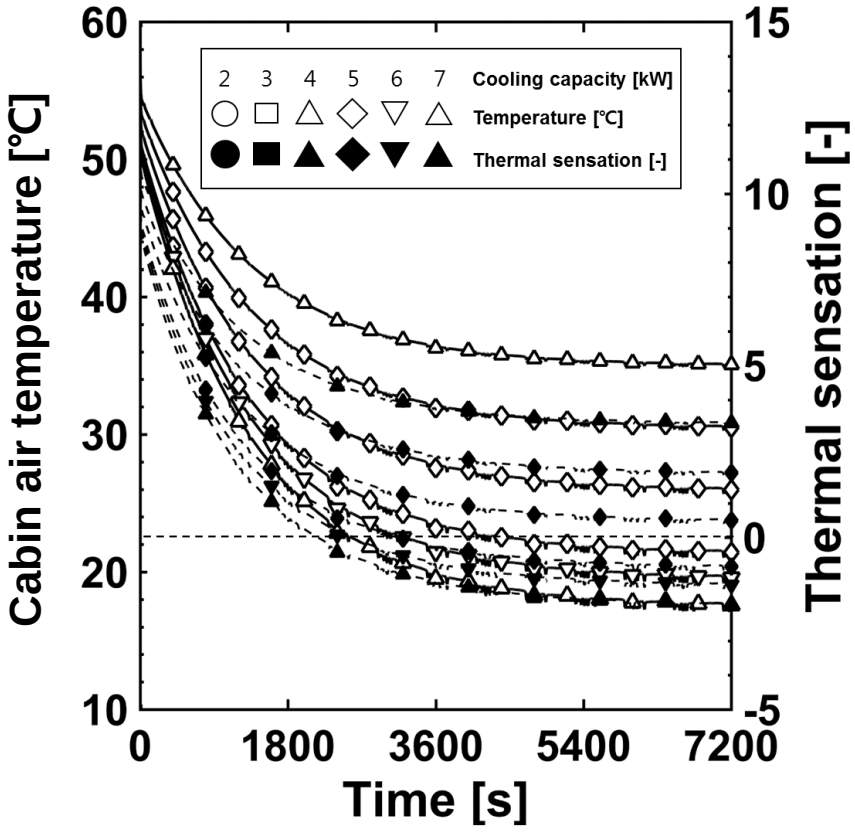

Fig. 2.26 Cabin air temperature and thermal sensation (cabin cooling)

is required to meet the thermal sensation. In order to satisfy the thermal sensation in the cabin in a short time in summer, a cooling capacity is required to meet the temperature and humidity of the air to the target thermal sensation. However, compared to winter, since the temperature of the interior of the cabin is maintained higher than the outside temperature in the summer, a higher cooling performance is required to lower the air temperature comparing with the cooling capacity that cools down the air only. Although, at initial condition, the temperature difference between cabin air temperature and ambient air is greater than that in winter, the maximum heating capacity in winter is larger than that in summer because the temperature difference between outdoor air and indoor air temperature is larger than is required to for summer. It is necessary to examine not only the maximum heating and cooling capacity required in winter and summer, but also how much cooling and heating capacity is required under other outdoor temperature conditions. The numerical study also conducted varying the simulation conditions. Fig. 2.27 shows the thermal load to meet the zero thermal sensation for various ambient conditions. It can be seen that as the outside temperature increases from 20ºC, a larger cooling and heating load is required. The maximum load is the capacity to satisfy the heat sensation within 1800 s, and the minimum load is selected as 3600 s for the target time. In order to confirm the required cooling and heating capacity

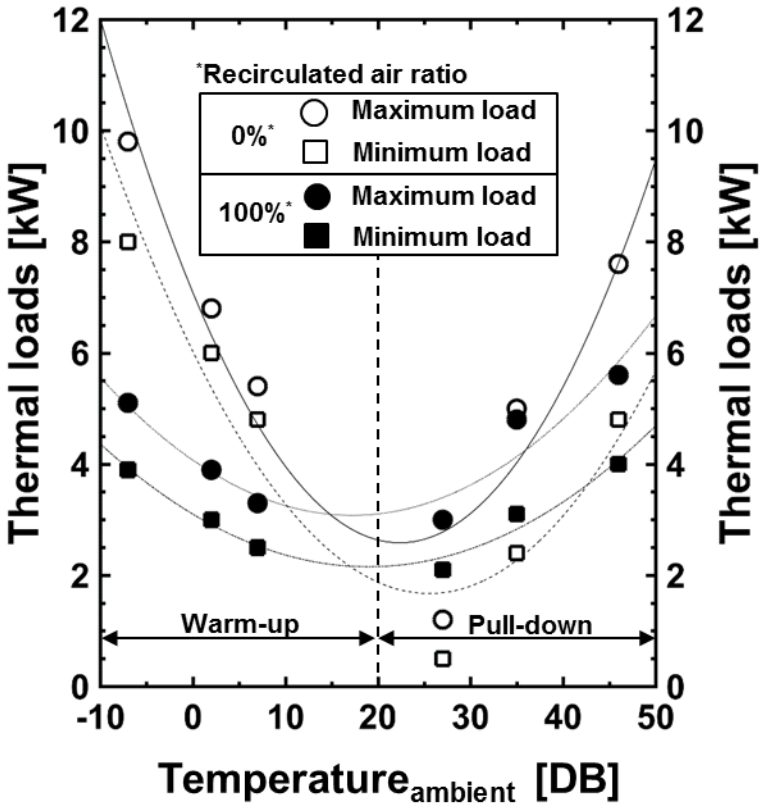

Fig. 2.27 Cabin thermal load simulation result

according to the use of ambient air circulation or the internal air circulation, numerical was performed by dividing when the air entering the cabin is 100% outside air and when in 100% internal air circulation mode. As a result, in most of the 100% outdoor air supply mode, a larger cooling and heating load was required. However, when the outside air temperature was 27ºC, the internal air circulation mode required a larger cooling capacity. The reason is that the outside temperature is sufficiently low to lower the indoor thermal sensation. Under such conditions, it is expected that the electric power consumed by the air conditioner can be reduced if outdoor air is actively used. Through this simulation study, it is possible to determine how much effect on the reduction of mileage when HVAC is operated in an electric vehicle in a cold winter or hot summer by confirming the cooling and heating capacity that varies greatly depending on the outside temperature.

2.5.3 Thermal load imbalance in a light-duty electric vehicle

By synthesizing the simulation results previously performed, it is possible to quantitatively predict the overall heat load required by the vehicle according to the outside temperature during driving of the electric vehicle. The temperature for the PEEM and ESS is assumed to be appropriate in consideration of the

Table 2.8 Basic concept of thermal management of electric powertrain

TMS objectives	TMS control		Working fluid
	Strategy	Location /Value	
EM	Limit hottest spot temperature	Copper coil /150ºC	Coolant
PE		IGBTs & Diodes /125 ºC	
ESS	Min-Max temperature	All cells /15-35ºC	Coolant
Cabin	Comfort temperature & RH	TSENS /0 (neutral)	Refrigerant

Table 2.8. It is assumed that the tempera of coil in electric machine is +60ºC comparing with the ambient temperature, and temperature of IGBTs and diodes in PE is +40ºC comparing with the ambient temperature, and the ESS temperature is equal to ambient temperature. The six representative ambient air temperature were selected in consideration of ISO 15042, 2017 [73], J2765, 2008 [74]. Since the thermal load of the electric drivetrain varies according to the driving conditions of the vehicle, the driving profile NYCC, UDDS and US06 are classified into low, medium, and high driving load conditions. Fig. 2.28 shows when the vehicle is driving under three driving load conditions (low: 0% gradeability, NYCC / medium: 0% gradeability, UDDS / high: 0%, gradeability, US06) for summer outdoor temperature conditions (T2, T1, T3). It shows the required cooling load (thermal load) from the electric powertrain and the air conditioning load required by the cabin of the vehicle. It can be seen that the higher the outside temperature, the higher the air conditioning load. It can be seen that the heat generation from the EPT occurs at a minimum of 500 W to a maximum of 2.5 kW under various operating load conditions. At this time, when the driving load of the vehicle is low under the condition that the ambient temperature is 46ºC, it can be confirmed that the cooling load to be removed by the low temperature radiator (LTR) is reduced. If the air conditioning load (condensing load) can be additionally removed through the

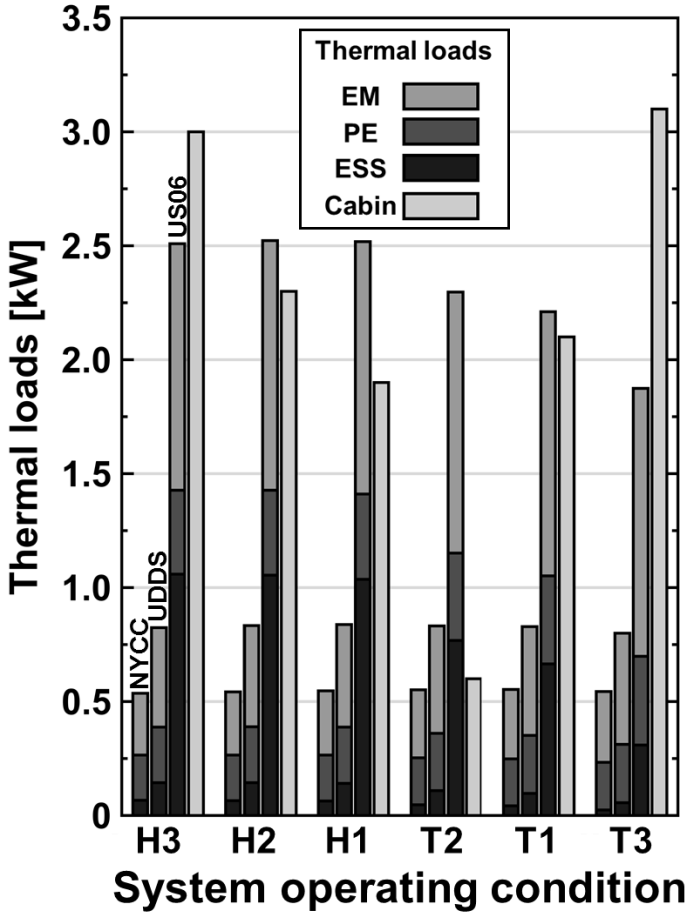

Fig. 2.28 Simulation results for thermal loads of a light-duty electric vehicle

LTR using these features, the performance and efficiency of the HVAC system can be increased. On the other hand, the figure shows the heat generation and air conditioning load of EPT according to the outdoor temperature and driving load in winter. The air conditioning load in winter is higher than in summer. The reason is that the difference between the proper temperature of the vehicle cabin and the outdoor temperature is larger in winter. In winter, when the driving load of the vehicle is low, about 500 W of waste heat is generated, but in high load conditions, since about 2.25 kW of waste heat is generated, the electric energy used in the PTC heater can be supplied if the heat source can be supplied as the heat of the heat pump. The system power consumption can be reduced by reducing. On the contrary, under high-load driving conditions in winter, 2.5 kW waste heat is generated from EPT, so this heat source is used to compensate for insufficient indoor heating capacity, or a waste heat utilization system is actively utilized to increase the mileage of electric vehicles in winter as shown in Fig 2.29. If there is a new integrated thermal management system that can be used both in winter and summer using these two features, the system can suppress the effect of reducing the mileage due to changes in outside temperature, and further, can have a positive effect on electric vehicles expanding.

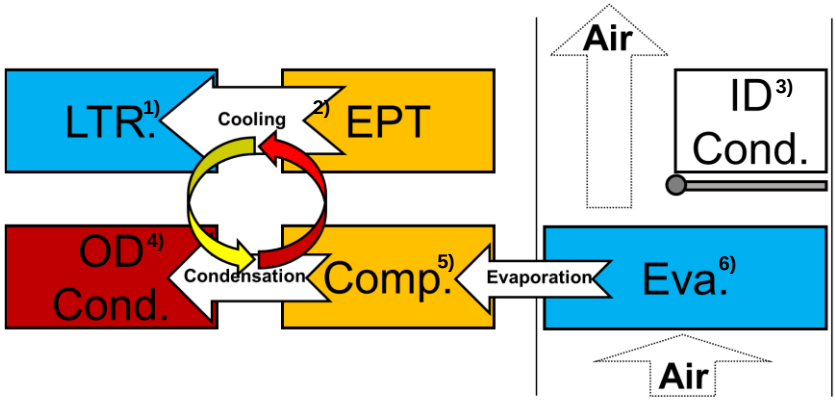

(a) Thermal management system for conventional vehicle

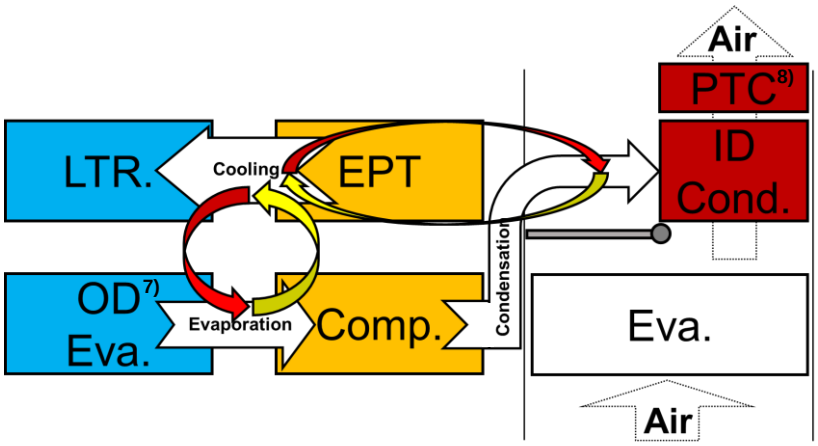

(b) Concept of integrated thermal management system for electric vehicle

Fig. 2.29 Comparison of the thermal management system

[1)] Low-temperature radiator, [2)] Electric powertrains, [3)] Indoor condenser, [4)] Outdoor condenser,

[5)] Compressor, [6)] Evaporator, [7)] Outdoor evaporator, [8)] Positive temperature coefficient heater

Chapter 3 Design and performance analysis of the integrated electric vehicle thermal management system

3.1 Introduction

Electric vehicles must release heat generated from EPT as well as to supply or remove heat to the cabin. Fluid machine, heat exchangers, and working fluid must be accompanied for the integrated thermal management of electric vehicle. However, in order to operate such a system, additional energy must be consumed, which is also the cause of depleting the driving energy of the electric vehicle. Fig 3.1 shows the electric power required by all thermal management systems and its efficiency in electric vehicles. As shown in Fig 3.2, the capacity of the PTC heater for indoor heating in winter is the largest, followed by the compressor and the PTC coolant heater. The consumption power of outdoor fan and indoor blower is about 5 ~ 10% compared to PTC heater or compressor that supplies heat source. Considering that approximately 60 kWh of electric energy is stored in the electric vehicle that is aimed at 400

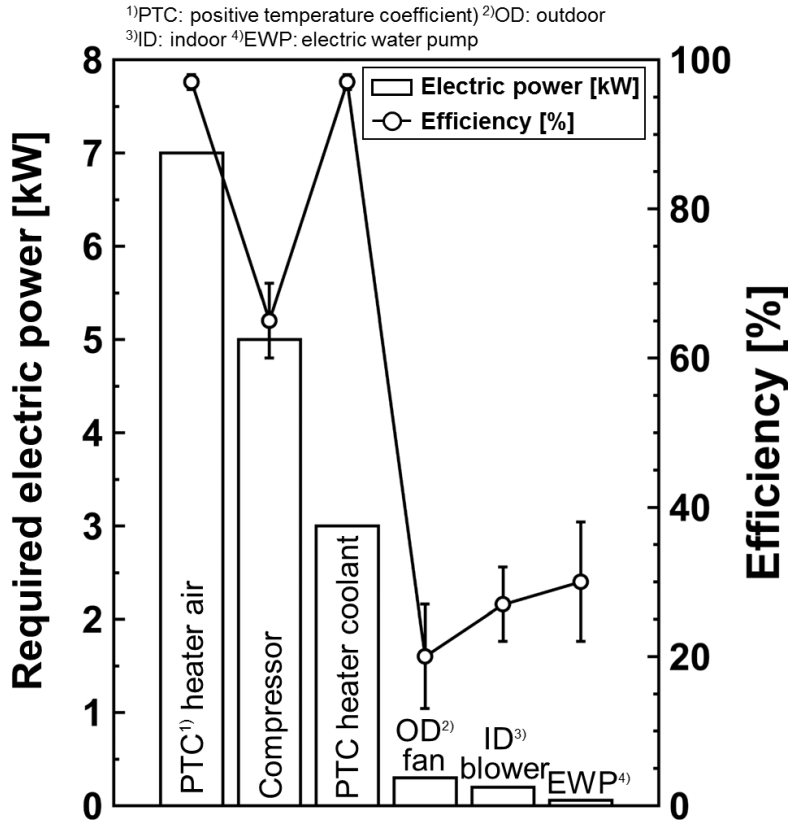

Fig. 3.1 Required electric power for thermal management system

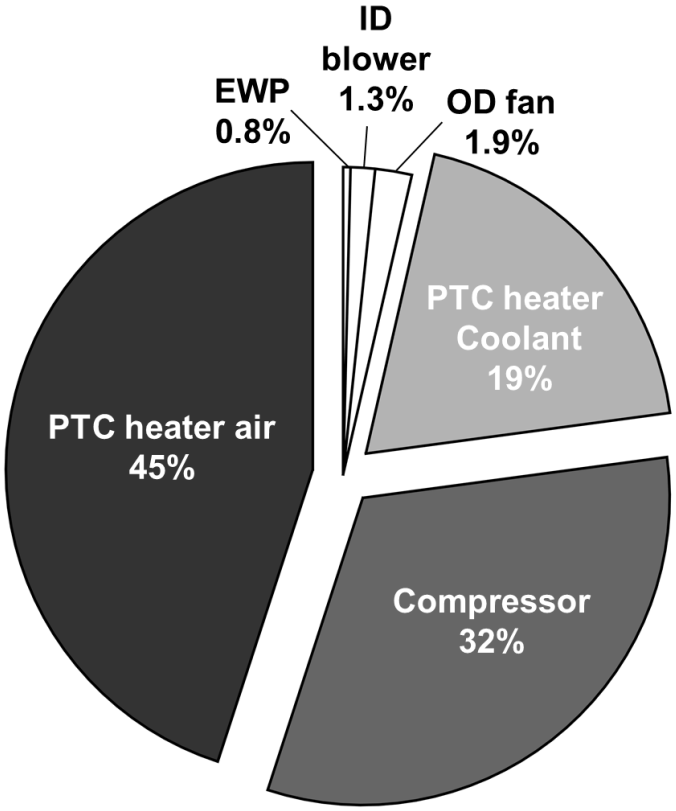

Fig. 3.2. Electric power distribution for electric vehicle thermal management system

km, it can be seen that a 5 kW PTC air heater is a significant source of energy consumption. On the other hand, it can be seen that the consumption power of the electric water pump circulating the cooling water is the smallest among all components. As an alternative technology to reduce the use of PTC air heaters in electric vehicles, heat pump technology is drawing attention as an alternative. In this study, in order to increase the performance and efficiency of such a heat pump, a new heat pump system is designed from the whole vehicle perspective. After all, in order to increase the driving distance, it is necessary to shift the frequency of using the PTC air heater to the heat pump and at the same time reduce the consumption power used by the compressor. When examining the power consumption of TMS, it can be seen that in order to increase the mileage of electric vehicles in winter, the use of PTC air heaters must be suppressed, and in order to increase the mileage in summer, the power consumption used in the compressor must be minimized. In this study, in order to minimize the power consumption used in TMS, a new integrated electric vehicle thermal management system is designed through consideration of the existing baseline system.

3.2 System description

3.2.1. Baseline thermal management system for electric

vehicle

Fig 3.3 represents the baseline integrated thermal management system. The configured baseline IEVTMS is designed to perform not only HVAC heating and cooling but also EPT thermal management. Looking from the HVAC point of view, it can be seen that the thermal energy is absorbed from the outdoor air heat source for indoor heating in winter and the heat is supplied to the room together with the PTC heater when there is insufficient heating capacity through the heat pump system. At this time, for the cooling of the PEEM, the electric water pump (EWP) absorbs heat energy generated by the PEEM and radiates it to the outside through the low temperature radiator (LTR). In the summer, thermal energy is discharged from a high-temperature, high-pressure refrigerant to an outdoor air heat source through a outdoor heat exchanger (condenser), and then heat is absorbed from the cabin. At this time, LTR is similarly used for cooling the PEEM. Since the thermal linkage between HVAC and EPT cannot be actively utilized in this configured cycle, there is a limit to increase the performance and efficiency of the HVAC system. However, in this study, it was assumed that the thermal management of the ESS was properly maintained according to the appropriate temperature.

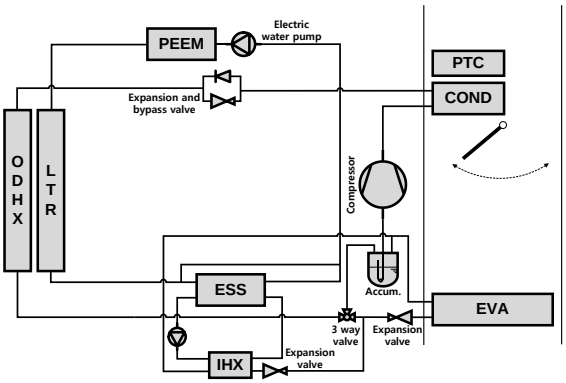

(a) Baseline IEVTMS

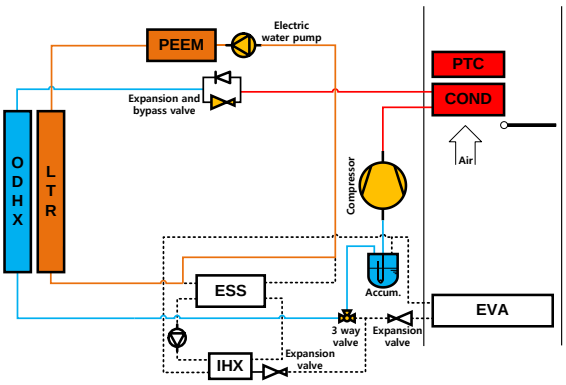

(b) Cabin heating mode of baseline IEVTMS

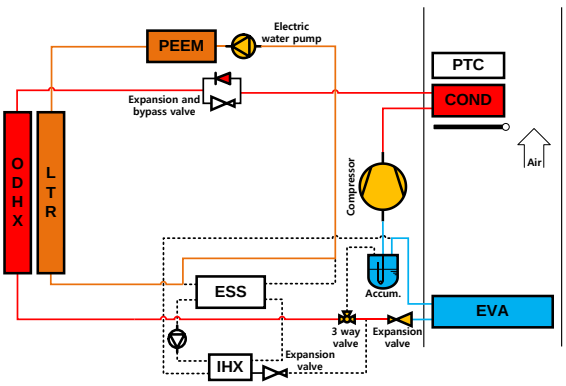

(c) Cabin cooling mode of baseline IEVTMS

Fig. 3.3 Baseline thermal management system for electric vehicle

3.2.2. A new integrated thermal management system

Table 3.1 shows the overall composition of the electric vehicle integrated thermal management system. In the leftmost column, the four driving loads are indicated. This running load determines the cooling load on the EPT. Apart from the cooling load of the EPT, the cooling and heating load of the cabin is mainly determined by the outside temperature. Recently, as the capacity of EV's EPT increases, the cooling load is increasing, and water cooling systems are widely applied for thermal management. In addition, the vapor compression cycle is applied for indoor cooling and heating. It has a structure in which heat generated from EPT and cabin is removed through outside air through each fluid machine and working fluid. A new IEVTMS was designed to secure the baseline system, which lacks thermal connectivity. The most important point in the newly proposed IEVTMS design is to design a system that can more efficiently respond to cabin thermal loads that change significantly with changes in ambient temperature as shown in Fig 3.4. In the case of a heat pump performing an indoor heating function in winter, the lower the outdoor temperature, the lower the heating performance and efficiency. In this case, the PTC heater is used to supply heating energy to the cabin. However, if the amount of use of the PTC heater cannot be reduced, the mileage of the electric

Table 3.1. Battery electric vehicle loads and its thermal management system

<table>
<tr><th colspan="5">Electric vehicle loads</th><th colspan="3">Thermal management system</th><th>Heat source or sink</th></tr>
<tr><td rowspan="2">Driving loads</td><td colspan="4">Thermal loads</td><td rowspan="2">Working</td><td rowspan="2">Fluid</td><td rowspan="2">HX</td><td rowspan="7">Air</td></tr>
<tr><td colspan="3">Driving power</td><td>Weather</td></tr>
<tr><td>Acceleration
Resistance</td><td rowspan="5">EM[1)]</td><td rowspan="4">PE[2)]</td><td rowspan="3">ESS[3)]</td><td rowspan="2">HVAC[4)]</td><td rowspan="2">Refrigerant</td><td>Compressor</td><td rowspan="2">ODHX[5)]</td></tr>
<tr><td>ID[6)] Blower</td></tr>
<tr><td>Air resistance</td><td rowspan="3">Coolant</td><td rowspan="2">OD air fan</td><td rowspan="3">LTR[7)]</td></tr>
<tr><td>Rolling resistance</td><td rowspan="2">EWP[8)]</td></tr>
<tr><td>Grade resistance</td></tr>
</table>

[1)] EM: electric machine [2)] PE: power electronics [3)] ESS: energy storage system [4)] HVAC: heating, ventilating and air conditioning

[5)] ODHX: outdoor (exterior) heat exchanger [6)] ID: indoor (interior) [7)] LTR: low temperature radiator [8)] EWP: electric water pump

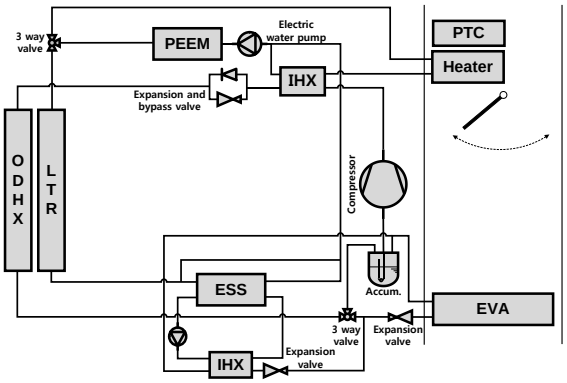

(a) A new IEVTMS

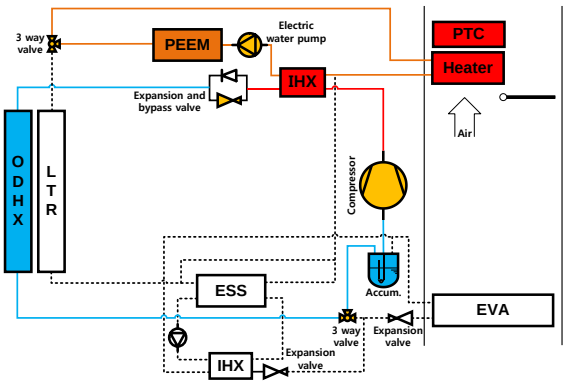

(b) Cabin heating mode of a new IEVTMS

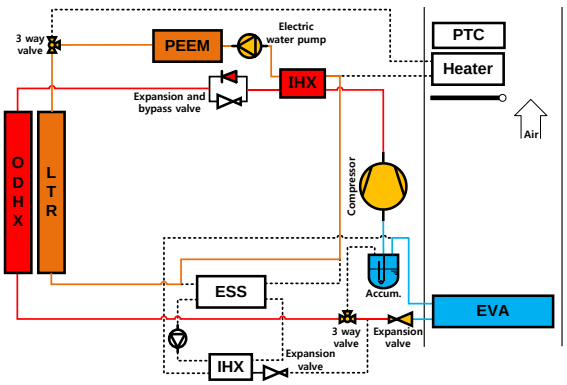

(c) Cabin cooling mode of a new IEVTMS

Fig. 3.4 Cabin cooling and heating operation mode using IEVTMS

vehicle cannot be increased. Therefore, in the newly proposed system, the heating energy is supplied to the cabin by using the unused thermal energy generated by the EPT to minimize the use of the PTC heater in winter. In addition, in order to reduce the energy consumed in indoor cooling in the summer, the heat source is removed through the newly added internal heat exchanger and the heat source to the outside of the system to reduce the pressure of the HVAC system. The most important point in the newly proposed IEVTMS design is to design a system that can more efficiently respond to cabin thermal loads that change significantly with changes in ambient temperature. Fig 3.5 shows the integrated electric vehicle thermal management system considering PEEM and ESS cooling system. The purpose of this system is to reduce the power consumption used in indoor cooling and heating in winter and summer while adding a minimum number of items compared to the existing baseline. The internal heat exchanger located at the high pressure of the heat pump cycle is a crucial part that strengthens the thermal linkage between the refrigerant system and the cooling water system. In the case of indoor cooling in summer, the cooling load of the EPT is small when the running load is low, so the condensation load of the outdoor heat exchanger can be distributed to the LTR through internal heat exchanger (IHX). Dispersion of the condensation load lowers the high pressure in the refrigerant system, which means that the power

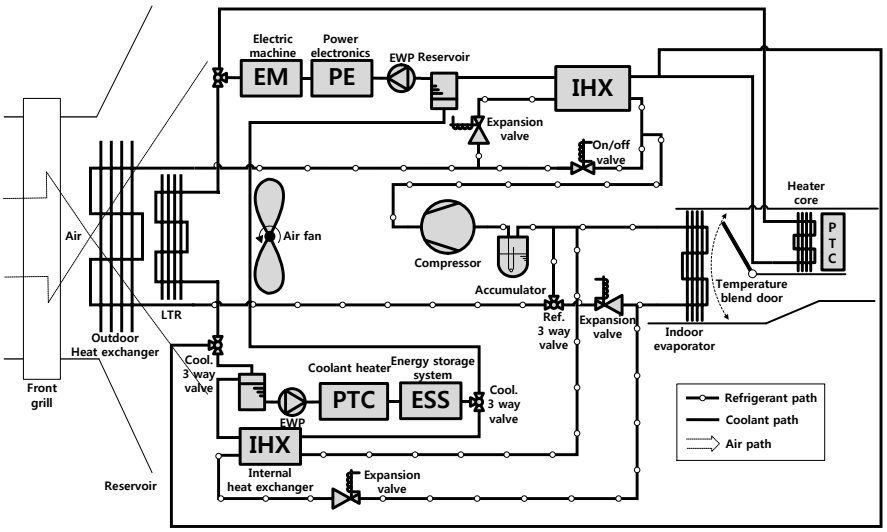

Fig. 3.5 A new integrated electric vehicle thermal management system

consumed in the refrigeration system can be reduced. The added IHX helps supply the heat generated by EPT to the room to compensate for the insufficient indoor heating capacity in winter. At this time, the refrigerant system serves as an auxiliary heating device that assists the insufficient heating heat source.

3.3 Numerical analysis of HVAC system

3.3.1 Heat exchangers

In order to design an integrated thermal management system, it is imperative to develop a model of heat pump for electric vehicle under consideration to strengthen the thermal interrelation between the vapor compression system and coolant thermal management system. In this study, the thermal management system for cabin has three heat exchangers. Outdoor heat exchanger has functional role, condenser for cabin cooling, evaporator for cabin heating. The two indoor units, each with a single function, are a condenser for cabin heating and evaporator for cabin cooling. Moreover, it is required to contain the radiator to release the thermal load from PEEM and ESS to the ambient air. The multi-louvered fin heat compact heat exchanger are adopted for simulation. The overall heat transfer coefficient can be obtained from overall heat transfer resistance by following equation,

$$\frac{1}{(\mathrm{UA})_{total}} = \frac{1}{(\mathrm{UA})_{air}} + \frac{1}{(\mathrm{UA})_{wall}} + \frac{1}{(\mathrm{UA})_{refrigerant}} \tag{3.1}$$

The overall heat transfer coefficient of the air side is defined with the following equation:

$$(\mathrm{UA})_{air} = \eta_{fin,overall} h_{air} A_{heat\_transfer} \tag{3.2}$$

The convective heat transfer coefficient is obtained from the Colburn j factor:

$$j_{air} = \frac{h_{air}}{\rho_{air} v_{air\_max} C_{P,air}} Pr^{2/3} \tag{3.3}$$

In this study, the correlation from Chang and Wang [76] was adopted to get the Colburn j factor for the louvered-fin heat exchangers with the following equation:

$$j_{air} = Re_{Lp}^{-0.49} \left(\frac{\theta}{90}\right)^{0.27} \left(\frac{F_p}{L_p}\right)^{-0.14} \left(\frac{F_l}{L_p}\right)^{-0.29} \left(\frac{T_d}{L_p}\right)^{-0.23} \times \left(\frac{L_l}{L_p}\right)^{0.68} \left(\frac{T_p}{L_p}\right)^{-0.28} \left(\frac{\delta_f}{L_p}\right)^{-0.05} \tag{3.4}$$

The overall fin efficiency of the louvered-fin heat exchangers is defined with

the following equations:

$$\eta_{fin,overall} = 1 - \frac{A_{fin}}{A_{heat\_trasnfer}}(1 - \eta_{fin}) \tag{3.5}$$

$$\eta_{fin} = \frac{\tanh(ML)}{ML} \tag{3.6}$$

where M and L are obtained from the geometry of the heat exchangers and the convective heat transfer of the air. The overall heat transfer coefficient of the wall of the heat exchanger is defined with the following equation:

$$(\mathrm{UA})_{air} = \frac{k_{tube}A_{heat\_transfer}}{t_{tube}} \tag{3.7}$$

The overall heat transfer coefficient of the refrigerant side varies depending on its state and heat transfer phenomenon, either evaporating or condensing. For single phase, Gnielinski correlation [77] was used for gas or liquid state of refrigerant both in condenser and evaporator. The equation is presented as

$$\mathrm{Nu}_{ref,single} = \frac{(f_{Darcy}/8)(Re_D - 1000)Pr}{1 + 12.7\left(\frac{f_{Darcy}}{8}\right)^{\frac{1}{2}}(Pr^{\frac{2}{3}} - 1)} \tag{3.8}$$

In case of two-phase flow of refrigerant, for condensing, two phase condensation heat transfer coefficient was determined by the correlation of Koyama et al. [78]. Koyama et al. suggested the new data set by optimizing its empirical constants for the present non-circular channel geometry. Their condensation heat transfer coefficient in terms of Nusselt number is expressed as a combination of forced convection term and free convection condensation term.

$$Nu = (Nu_F^2 + Nu_B^2)^{1/2} \tag{3.9}$$

$$Nu_F = 0.0112 Pr_{liquid}^{1.37} \left(\frac{\phi_{vapor}}{X_{tt}}\right) Re_{liquid}^{0.7} \tag{3.10}$$

where,

$$Re_{liquid} = \frac{G(1-x)D_h}{\mu_{liquid}} \tag{3.11}$$

The Pr_{liquid} and Re_{liquid} are the Prandtl and Reynolds number for liquid state. The free convection condensation term is expressed as

$$Nu_B = 0.725(1 - e^{(-0.85\sqrt{Bo})})H(\alpha)\left(\frac{Ga_{liquid}Pr_{liquid}}{Ph_{liquid}}\right)^{1/4} \quad (3.12)$$

where the function of void fraction $H(\alpha)$, the Galileo number Ga_{liquid} and the phase change number Ph_{liquid} are defined as

$$H(\alpha) = \alpha + \ [10(1-\alpha)^{0.1} - 8.9]\sqrt{\alpha}(1-\sqrt{\alpha}) \quad (3.13)$$

$$Ga_{liquid} = \frac{g\rho_{liquid}^2 D_h^3}{\mu_{liquid}^2} \quad (3.14)$$

$$Ph_{liquid} = \frac{Cp_{liquid}(T_{ref} - T_{wall,in})}{\Delta h_{vl}} \quad (3.15)$$

In case of two-phase flow of refrigerant, for evaporating, the correlation from Sun and Mishima model [79] was adopted and the equation is presented as follow:

$$h_{tp} = \frac{6Re_{lo}^{1.05}Bo^{0.54}}{We_l^{0.191}\left(\frac{\rho_l}{\rho_v}\right)^{0.142}}\frac{k_l}{D_h} \ , \qquad We_l = \frac{G_{ref}^2 D_h}{\sigma\rho_l} \quad (3.16)$$

3.3.2 Compressor

A simple mathematical model was selected to simulate, high-voltage and -rotational speed, electric scroll compressor with 33 cc compression volume. In the compressor modeling, the input properties are suction pressure, discharge pressure, and suction temperature. In order to calculate the discharge enthalpy and enthalpy difference during compression process, the concept of isentropic efficiency (η_{isen}) was applied as Eq. (3.17).

$$i_{comp,out} = i_{comp,in} + \frac{i_{comp,out,assumed} - i_{comp,in}}{\eta_{isen}} \tag{3.17}$$

$$di_{comp} = i_{comp,out} - i_{comp,in} \tag{3.18}$$

Refrigerant mass flow rate from the compression process is determined by Eq. (3.19), and the electric work consumed by the compressor is also determined by Eq. (3.20).

$$\dot{m}_{comp} = \rho_s (V_{disp} \eta_V) w_{comp} \tag{3.19}$$

$$W_{comp} = \frac{\dot{m}_{comp} di_{comp}}{\eta_{mech}} \tag{3.20}$$

The volumetric efficiency, η_V, isentropic efficiency, η_{isen}, and mechanical efficiency, η_{mech}, are pre-obtained values from the experiments. The efficiency are in the range of about 0.64 to 0.92 depending on changes in compression ratio and its rotational speed.

3.3.3 Expansion device

In this system, a needle type expansion valve was used as the expansion device as shown in Fig 3.6. The length of needle (L_{needle}) was 10 mm, the radius of needle ($r_{needle,fixed}$) was 0.78 mm, and it had 0.5 mm pitch. The refrigerant isenthalpic expands in the electronic expansion valve, so in steady-state modeling, the expansion valve can be simplified as the following Eq. (3.21).

$$i_{eev,in} = i_{eev,out} \tag{3.21}$$

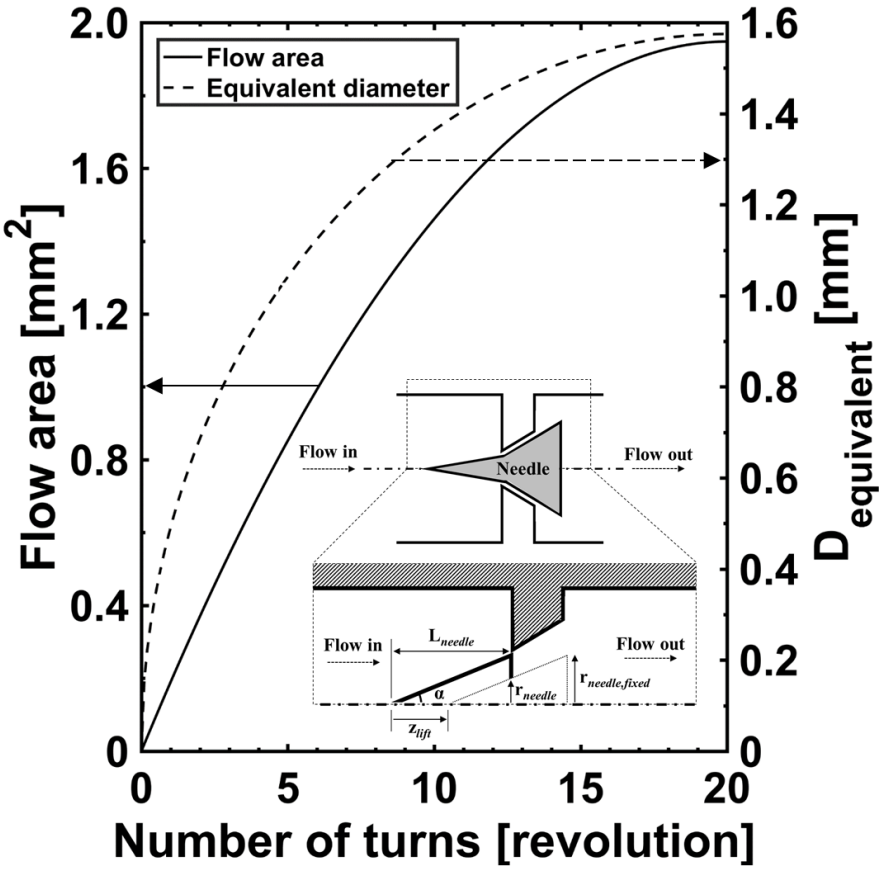

Fig. 3.6 The geometry of the expansion device

3.3.4 Cycle modeling and simulation condition

With the component modeling of heat pump system, a detailed cycle modeling and simulation are possible. Unlikely to typical heat pump simulation, the driving information is given and then the charge amount is calculated. Fig. 3.5 describes the flow chart of the simulation. This figure is a heat pump steady state simulation algorithm. The low pressure of the heat pump is selected to track according to the fixed degree of super heat (DSH) at the compressor inlet, and the refrigerant high pressure of the heat pump is the decided by a logic that is determined to match the amount of refrigerant charged in the system.

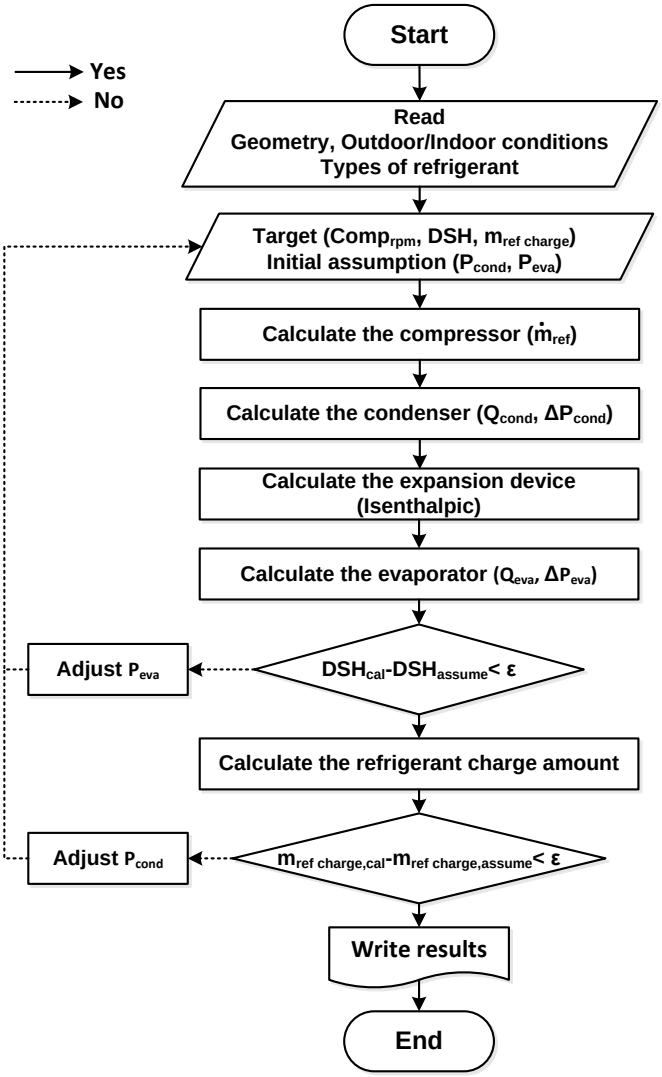

Fig. 3.7 Flow chart of the heat pump simulation

3.3.5 Simulation condition

Table 3.2 shows the simulation condition for both indoor and outdoor air. The six representative temperate condition are from ISO 15042 (2017) [74] and J2765 (2008) [75]. The velocity of outdoor is set as 4 m/s which is the speed of air entering the outdoor heat exchanger unit when the light duty electric vehicle is driving at 100 km/h with outdoor air fan operation. The volume flow rate of indoor is 7 m^3/min. This flow rate is the maximum flow rate for the light duty electric vehicle HVAC system.

3.3.6 Heating and cooling capacity prediction

Heat pump model simulation was performed under the same conditions to experiments. Fig. 3.7 shows the heating and cooling capacity results through simulation. As can be seen, the accuracy of the prediction is very high. The root mean square error (RMS error) is 18.34% and the absolute average deviation (AAD) is 12.12%.

Table 3.2 Simulation and experiment conditions

	Outdoor		**Indoor**	
Cooling mode	**DB [ºC]**	**Air Velocity [m/s]**	**DB/WB [ºC]**	**Volume flow rate [m^3/min]**
T1 (Moderate)	35	4	27/19	7
T2 (Cool)	27		21/15	
T3 (Hot)	46		29/19	

heating mode	**DB [ºC]**	**Air Velocity [m/s]**	**DB/WB [ºC]**	**Volume flow rate [m^3/min]**
H1 (Warm)	7	4	20/15	7
H2 (Moderate)	2			
H3 (Cold)	-7			

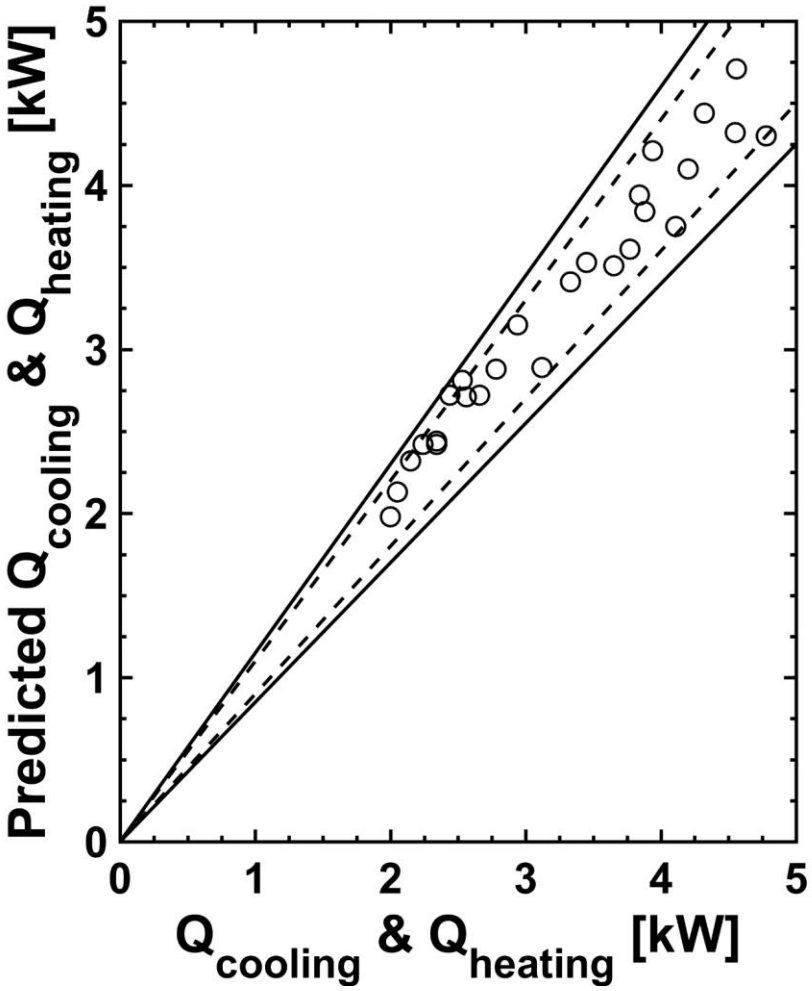

Fig. 3.8 Heating and cooling capacity prediction results

3.4 Experimental study for integrated electric vehicle thermal management system

3.4.1 Experimental set-up

An experiment was conducted to verify the HVAC energy consumption reduction effect by the proposed integrated thermal management system. An electric vehicle heat pump system with nominal capacity of 5 kW, shown in the Fig. 3.7, was used for the experiments. The experimental apparatus is primarily divided into three parts. A constant temperature and humidity chamber with wind tunnel system that can control the temperature, humidity, and flow rate of outdoor air; a constant temperature and humidity chamber with wind tunnel system that control the temperature, humidity and flow rate of indoor air; and a heat pump system with internal heat exchanger to verify the effect of the thermal link between the coolant and the refrigerant system. In Table 3.3, specification of all components is represented. Fig. 3.8 shows a schematic diagram of the experimental facilities. The system is installed in an environmental chamber that can control the air temperature and humidity of the indoor chamber and outdoor chamber separately. The compressor is located in the middle of the outdoor and indoor unit. Using the scroll type inverter compressor, the rotational speed of the compressor is controlled. Needle type

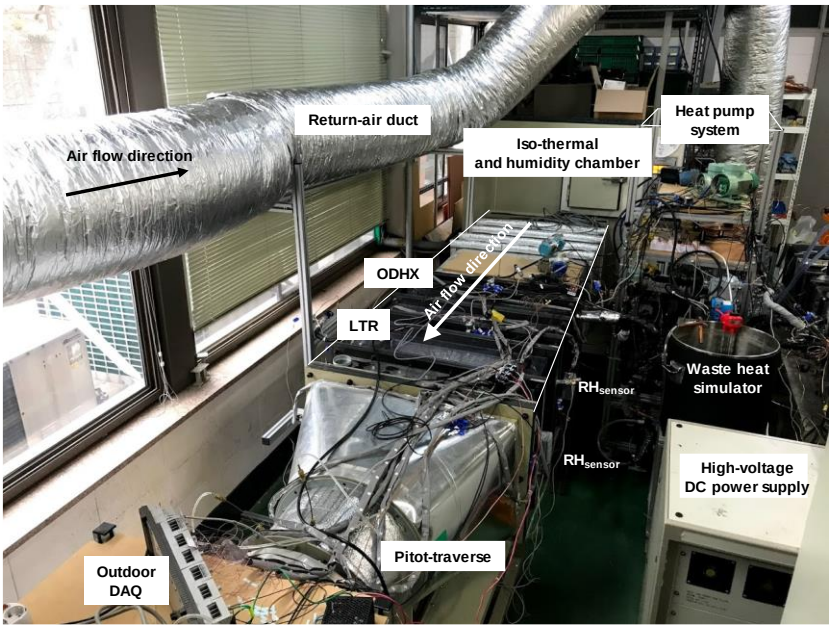

(a) Outdoor air temperature and humidity simulator

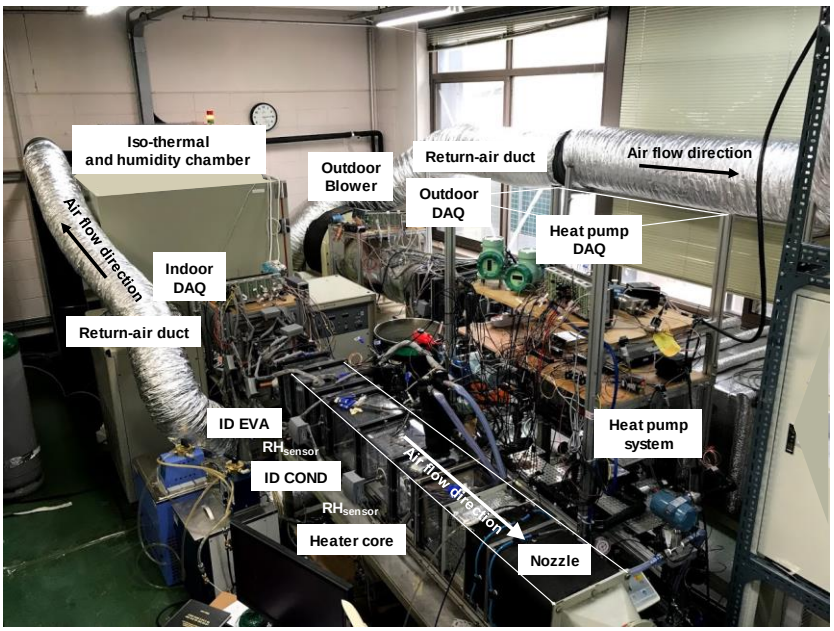

(b) Indoor air temperature and humidity simulator

Fig. 3.7 Light-duty battery electric vehicle IEVTMS simulator

Table 3.3 Specification of HVAC system

Components	Type	Specification
Compressor	Scroll type	Discharge: 33 cm^3/rev Speed range: 1000 ~ 8000 rpm Power: Direct current (380 V)
Outdoor heat exchanger	Louvered fin, Compact heat exchanger with multiport mini-channel tubes	573 (W) x 345 (H) x 20 (D) mm^3
Indoor evaporator		256 (W) x 215 (H) x 45 (D) mm^3
Indoor condenser		216 (W) x 160 (H) x 20 (D) mm^3
Low temperature radiator	Louvered fin, Compact heat exchanger with flat tubes	610 (W) x 412 (H) x 14 (D) mm^3
Indoor heater core		211 (W) x 160 (H) x 27 (D) mm^3
Expansion valve	Needle type	Maximum revolution: 20 turns Maximum flow area: 1.95 mm^2
Internal heat exchanger	Offset strip fins	560 (W) x 70 (H) x 50 (D) mm^3

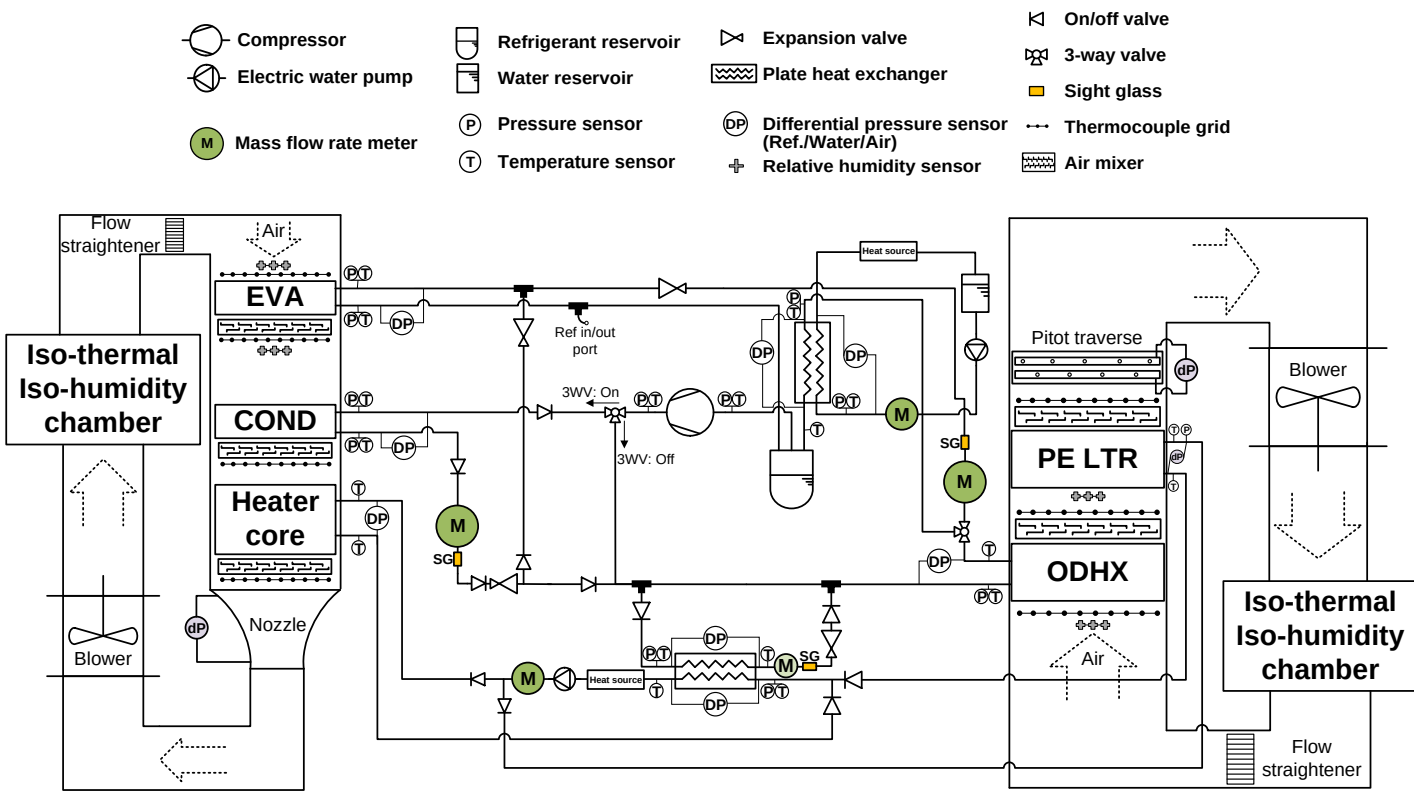

Fig. 3.9 Schematic diagram for the experimental set-up

expansion valves are installed in both indoor units and outdoor unit. The expansion valve at indoor units activate during cooling mode operation, and the expansion valve at outdoor unit operates during heating mode operation. In each case, unused expansion valve were kept fully open. A number of temperature, pressure sensors and mass flow meter are installed. The sensors used for the experiments are presented in Table 3.4 and Table 3.5. In addition, a wind tunnel and nozzles are installed in the indoor chamber to accurately measure the cooling (or heating) capacity of the system. Based on ANSI / AMCA 210 (2007), indoor unit capacity was calculated through air temperature, humidity and flow rate information. The airflow rate and velocity for ODHX (outdoor heat exchanger) are calculated from the pressure difference measured by circular type Pitot tube traverse. The pressure difference is obtained from a one minute average ΔP based on a continuous measurement. The air velocity at the Pitot traverse is defined as

$$\mathrm{v}_{air,\text{Pitot traverse}} = \sqrt{2}\sqrt{\frac{\Delta P_{\text{Pitot traverse}}}{\rho_{air}}} \tag{3.22}$$

The volume flow rate of the air is obtained by following equation

Table 3.4 Specification of measurement instruments

Sensors		Specification	Accuracy (Full scale)	Manufacturer
Data acquisition		DA100	DV voltage: ±0.05% of rdg+5 digits T-type: ±0.05% of rdg+0.5°C	Yokogawa Electric
Thermocouple		T-type	±0.7°C	Omega
Pressure transmitter		TST-10 -40 ~ 125°C	±0.5% F.S.	TIVAL
Relative humidity transmitter		0~100% RH -5 ~ 55°C	±1.7% (RH) F.S. ±0.2°C	VAISALA
Mass flow meter	ODHX	CN010	±0.1% F.S.	OVAL
	Indoor cond.	CX006	±0.1% F.S.	
	Coolant			
Power meter		WT230	±0.1% F.S.	Yokogawa Electric

Table 3.5 Specification of measurement instruments

Sensors		Specification	Accuracy (Full scale)	Manufacturer
Data acquisition		DA100	DV voltage: ±0.05% of rdg+5 digits T-type: ±0.05% of rdg+0.5°C	Yokogawa Electric
Thermocouple		T-type	±1°C	Omega
Pressure transmitter		TST-10 -40 ~ 125°C	±0.5% F.S.	TIVAL
Relative humidity transmitter		0~100% RH -5 ~ 55°C	±1.7% (RH) F.S. ±0.2°C	VAISALA
Mass flow meter	ODHX	CN010	±0.1% F.S.	OVAL
	Indoor cond.	CX006	±0.1% F.S.	
	Coolant			
Power meter		WT230	±0.1% F.S.	Yokogawa Electric

Table 3.6 Specification of measurement instruments

Sensors		Specification	Accuracy (Full scale)	Manufacturer
Differential pressure transmitter	Refrigerant	ODHX: 0-4bar	ODHX (3051S2C04) ±0.055%	ROSEMOUNT
		ID COND: 0-2 bar	STX2100 ±0.04%	Druck
		ID EVA: 0-2 bar	STX2100 ±0.04%	Druck
		IHX top: 0-4 bar	STX2100 ±0.04%	Druck
		IHX bottom: 0-2 bar	STX2100 ±0.04%	Druck
	Water	LTR: 0–500 kPa	SSDB0500R1A ±0.5% F.S. ±1 digit	Sensys (Korea)
		ID heater core: 0-2 bar	STX2100 ±0.04%	Druck
	Air	FCO510 (outdoor)	0.25% F.S.	FURNESS Controll
		264 (indoor)	±1.0% F.S.	SETRA
Pitot Traverse (8-points) (outdoor)		D104A018SSSSS1Z	±1.0% F.S.	Thermo Electron Corporation

$$\dot{V}_{air,\text{Pitot traverse}} = \text{v}_{air,\text{Pitot traverse}}\ \text{A}_{\text{Pitot traverse}} \tag{3.23}$$

The air velocity of outdoor heat exchanger is obtained by following equation

$$\text{v}_{air,\text{ODHX}} = \frac{\dot{V}_{air,\text{Pitot traverse}}}{\text{A}_{\text{ODHX}}} \tag{3.24}$$

The airflow rate for indoor is calculated from the pressure differential measured across a single nozzle [80]. The indoor air volume flow rate is defined as Eq. (3.25)

$$\dot{V}_{air,indoor} = \frac{CA_{nozzle,exit}Y\sqrt{2\Delta P/\rho_{air}}}{\sqrt{1-E\beta^4}} \tag{3.25}$$

where, C is discharge coefficient defined as

$$C = 0.9986 - \frac{7.006}{\sqrt{Re}} + \frac{134.6}{Re} \tag{3.26}$$

and, Y is Expansion factor obtained from Eq. (3.27)

$$\gamma = 1 - (0.548 + 0.71\beta^4)(1 - \alpha) \tag{3.27}$$

According to ISO 15042 (2017) [74] and J2765 (2008) [75], three temperature conditions for cooling mode and three temperature conditions for heating mode were selected. Prior to the experiment, a reference case experiment was conducted to find the optimum refrigerant charge of the system. The experimental range of refrigerant charge condition was selected approximately from 90% to 110% of the optimum charge amount. The system refrigerant charge amount was determined following SAE standard J2765 based on cooling (T2, 27ºC) and heating operation (H2, 2ºC). Lubricant charge was kept constant in current study. During the test, compressor speed was set to 350 rev/min. Refrigerant R134a was gradually added into the system in increments of 50 g starting from 200 g for cooling mode, staring from 400g for heating mode, while for each charge amount, the system was stabilized for at least 10 min, and then data were recorded in intervals of 6 s for another 10 min and averaged to reduce random error.

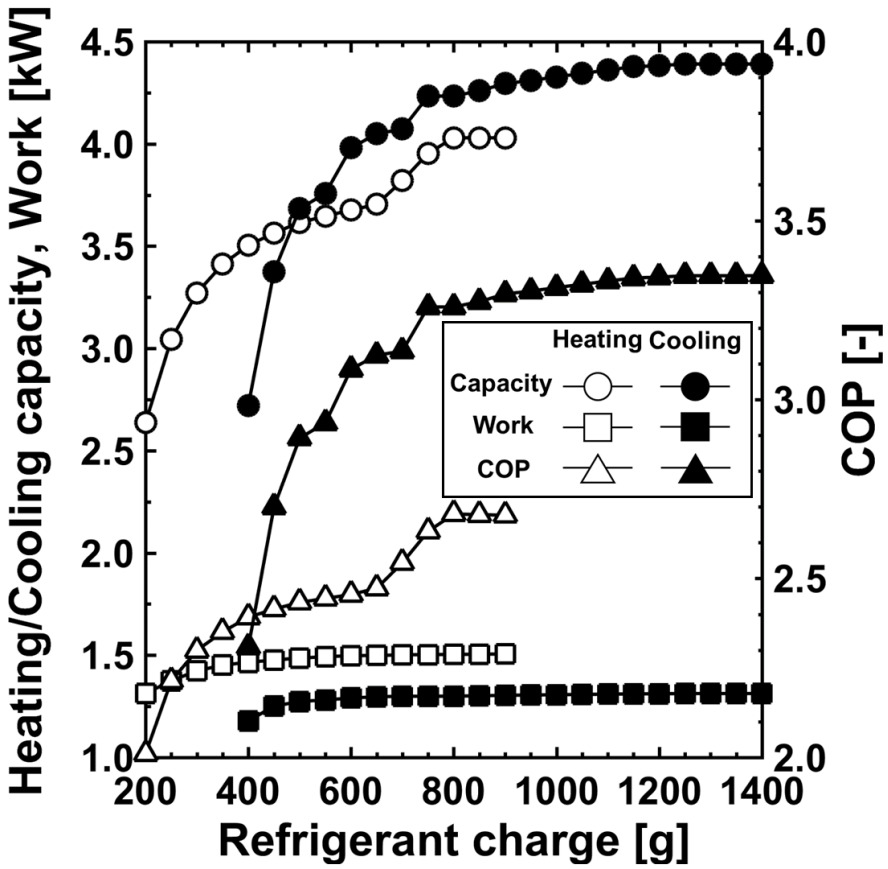

Fig. 3.10 Refrigerant charge determination test

(heating mode and cooling mode)

3.4.2 Data reduction and uncertainty analysis

The optimum charge amount of the system was determined through reference case experiment. Here, the optimum charge amount is defined as a point at which the COP reaches its maximum. The cooling (or heating) capacity and the COP are calculated from the following Eqns. (3.19) and (3.20).

$$Q_{air} = \rho_{air}\dot{V}_{air}(i_{air,inlet} - i_{air,outlet}) \quad (3.13)$$

$$\mathrm{COP} = Q_{air}/W_{comp} \quad (3.14)$$

The uncertainty of measurement data is shown in Table 3.7. The total error of cooling and heating) capacity is 5.41% and 5.12% and the total error of COP is 5.43% on 95% confidence level.

Table 3.7 Uncertainty analysis at reference condition

Variables	Fixed error	Random error	Total error
Pressure transducer (high)	0.5%	0.28%	0.74%
Pressure transducer (low)	0.5%	0.14%	0.57%
Thermocouple (T-type)	0.5K	0.89K	0.89K
Mass flow rate (refrigerant)	0.1%	1.56%	3.09%
Mass flow rate (water)	0.1%	0.16%	0.33%
Differential pressure transducer (outdoor)	0.25%	0.015%	0.25%
Differential pressure transducer (indoor)	1.0%	0.11%	1.02%
Power meter	0.2%	0.23%	0.49%
Cooling capacity	5.32	1.51%	5.41%
Heating capacity	4.95	1.32%	5.12%
COP	-	-	5.43%

3.4.3 Baseline heat pump system

Figure 3.10 shows the pressure-enthalpy chart for the three cooling modes of the baseline system, T1 (OD: 35ºC - ID: 27ºC), T2 (OD: 27ºC - ID: 21ºC), and T3 (OD: 46ºC - ID: 29ºC). For each driving condition, the degree of super heat (DSH) was controlled at 5 K and the compressor rpm was operated at 2000 rev/min to 6000 rev/min. The cooling capacity, compressor work, and the COP is represented in Fig 3.11. The maximum cooling capacity is 5.95 kW at T1 condition at 6000 rpm. Figure 3.12 shows the pressure-enthalpy chart for the three heating modes of the baseline system, H1 (OD: 7ºC - ID: 20ºC), H2 (OD: 2ºC - ID: 20ºC), and H3 (OD: -7ºC - ID: 20ºC). For each driving condition, the degree of super heat (DSH) was controlled at 5 K and the compressor rpm was operated at 2000 rev/min to 6000 rev/min. The cooling capacity, compressor work, and the COP is represented in Fig 3.13. It can be seen that the COP of the heat pump at H3 condition is lower than that of other results. The reason is that the evaporation temperature of the heat pump system decreases according to the outside temperature, causing a decrease in the mass flow rate of the refrigerant circulating inside the system. Looking at the experimental results, it can be seen that the maximum heating capacity is insufficient compared to the maximum cooling capacity. The reason comes from the shape constraints of the electric vehicle heat pump system. Due to the characteristics of automobiles,

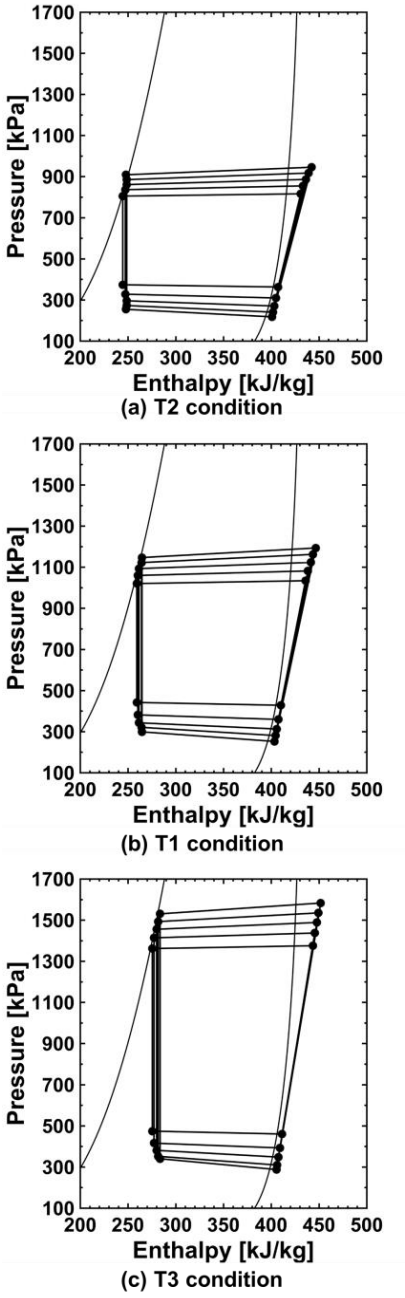

Fig. 3.11 Pressure-enthalpy diagram for cooling conditions (baseline)

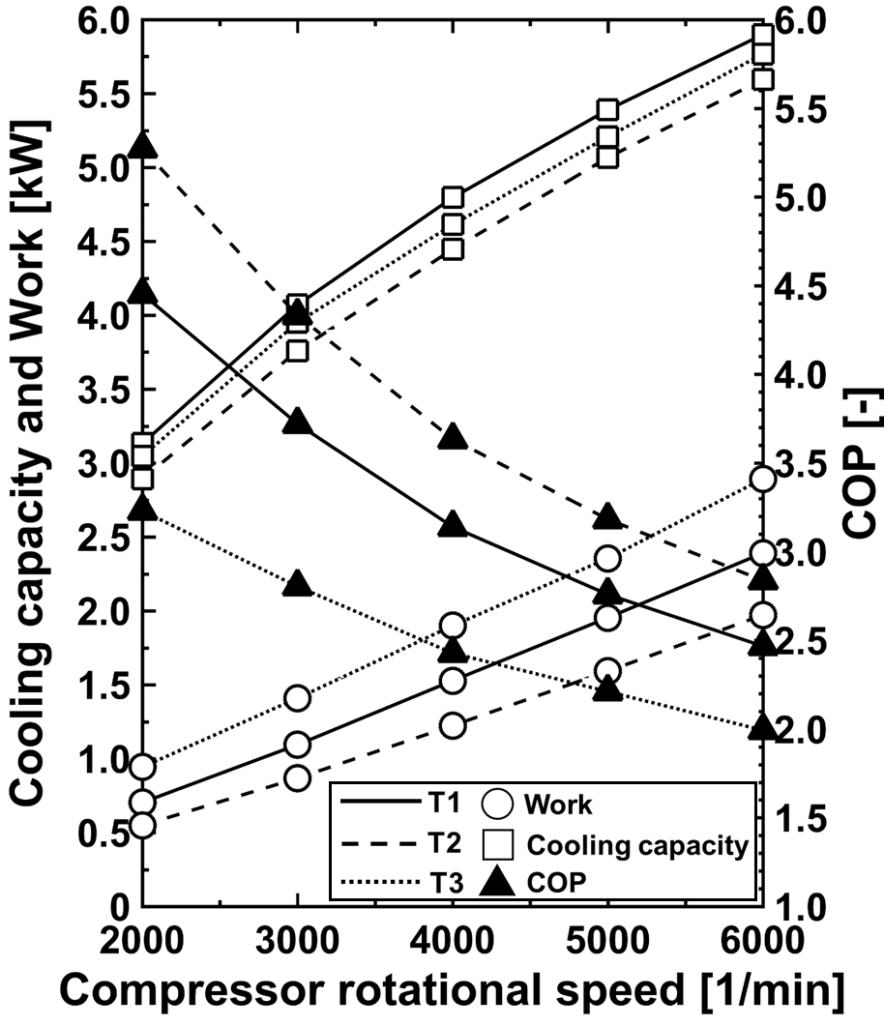

Fig. 3.12 Effect of compressor rotational speed on cooling capacity, work, and COP (baseline)

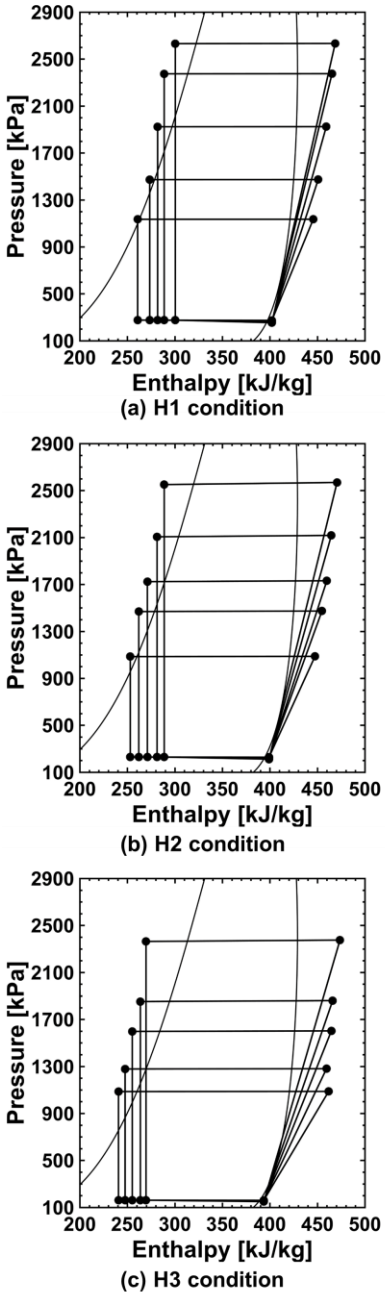

Fig. 3.13 Pressure-enthalpy diagram for heating conditions (baseline)

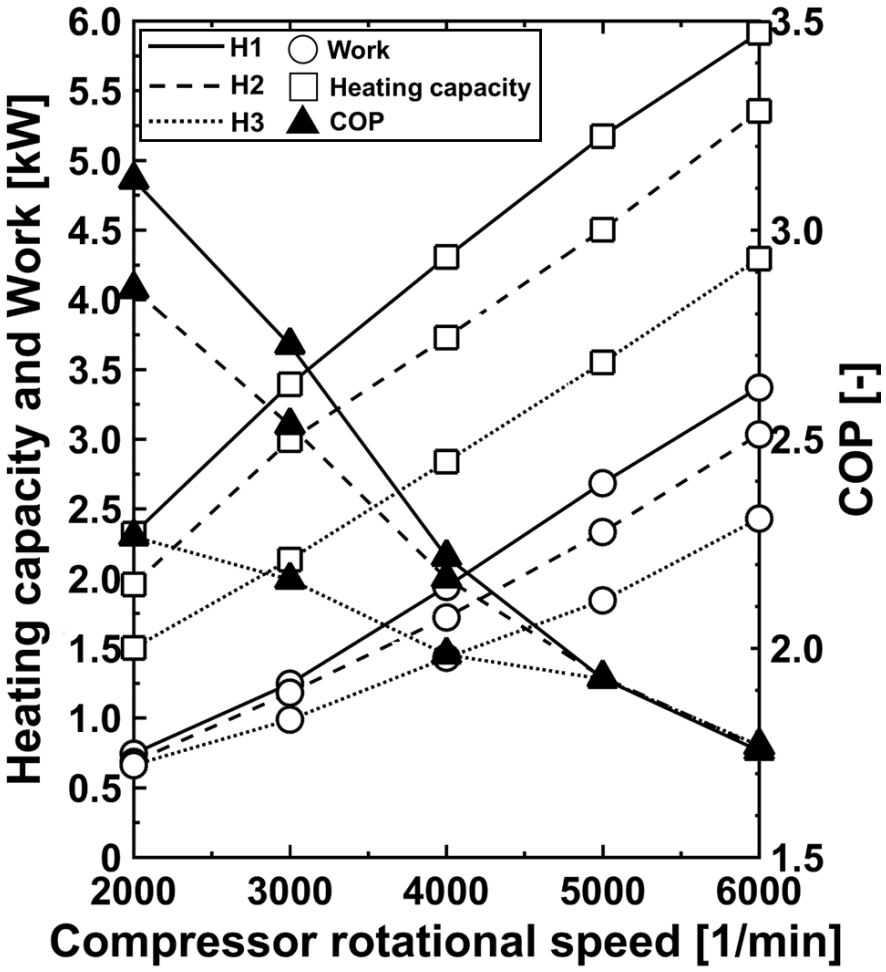

Fig. 3.14 Effect of compressor rotational speed on heating capacity, work, and COP (baseline)

condenser cause the compressor to use more electric energy to obtain the required heating capacity. Fig 3.14 shows the experimental results for the baseline heat pump system. It can be seen that the change in heating capacity is more severe in the winter heating mode than in the summer cooling mode. In addition, it can be seen that the power consumption of the compressor is greater in the heating condition than in the cooling condition. Due to these heat pump characteristics, it can be indirectly confirmed that the reduction rate of mileage of electric vehicles in winter is higher. In addition, it can be seen that COP decreases rapidly as the outside temperature deviates from mild conditions.

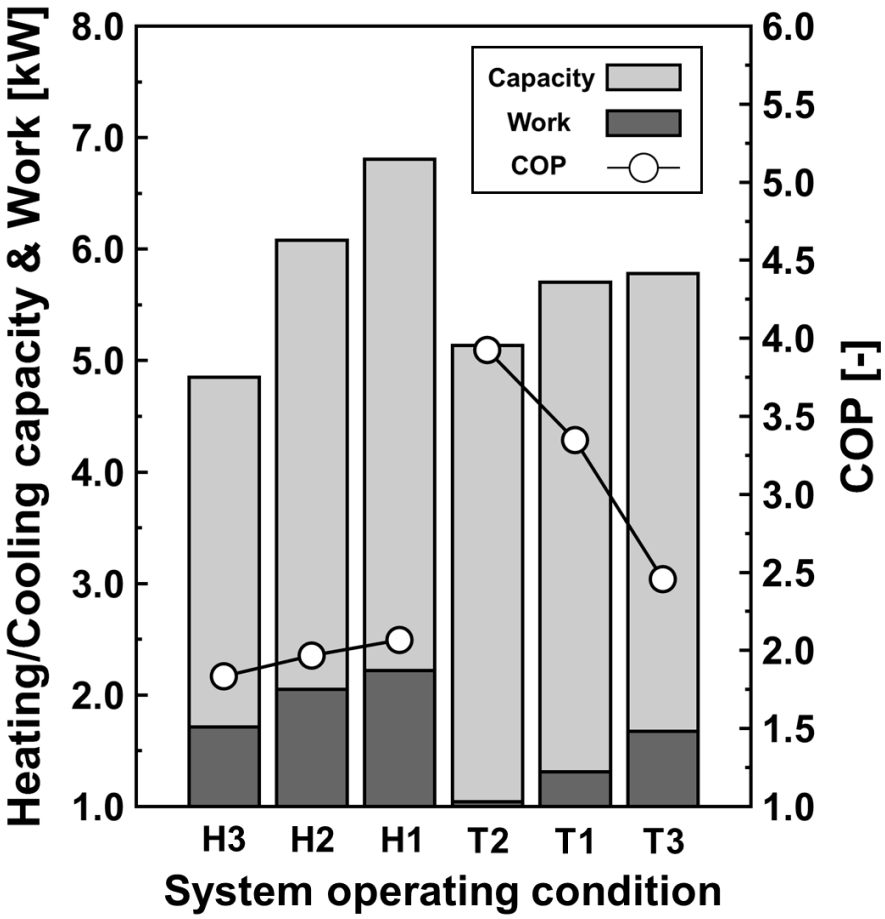

Fig. 3.15 Heating and cooling performance and COP (baseline)

3.4.4 A New integrated electric vehicle thermal management system

The new integrated electric vehicle thermal management system is designed to use lower compressor energy to cabin heating and cooling, strengthening the thermal connectivity between the EPT and cabin thermal management system. The internal heat exchanger conducted two roles, thermal load distributor for cabin cooling, and unused heat direct use for cabin heating. Fig. 3.15 shows the experimental results for the IEVTMS using thermal load distribution strategy. The most important part in strengthening the thermal relationship is that it should not have a significant influence on the operation of the cooling water thermal management system. Experiments were performed for three cooling conditions. The thermal load predicted through the integrated heat generation model was applied to the experiment. The range of cooling load from PEEM was selected as 0.5, 1.0, 1.5, and 2.0 kW, and the flow rate was controlled so that the temperature of the cooling water flowing into the PEEM was less than 60ºC and the temperature of the cooling water flowing out through the PEEM was less than 65ºC. The compressor rotational speed was controlled from 2000 rev/min to 5000 rev/min. As a result, it was confirmed that the PEEM thermal management was properly maintained even though the thermal load was 2.0 kW, and the high pressure of the heat pump system was lowered

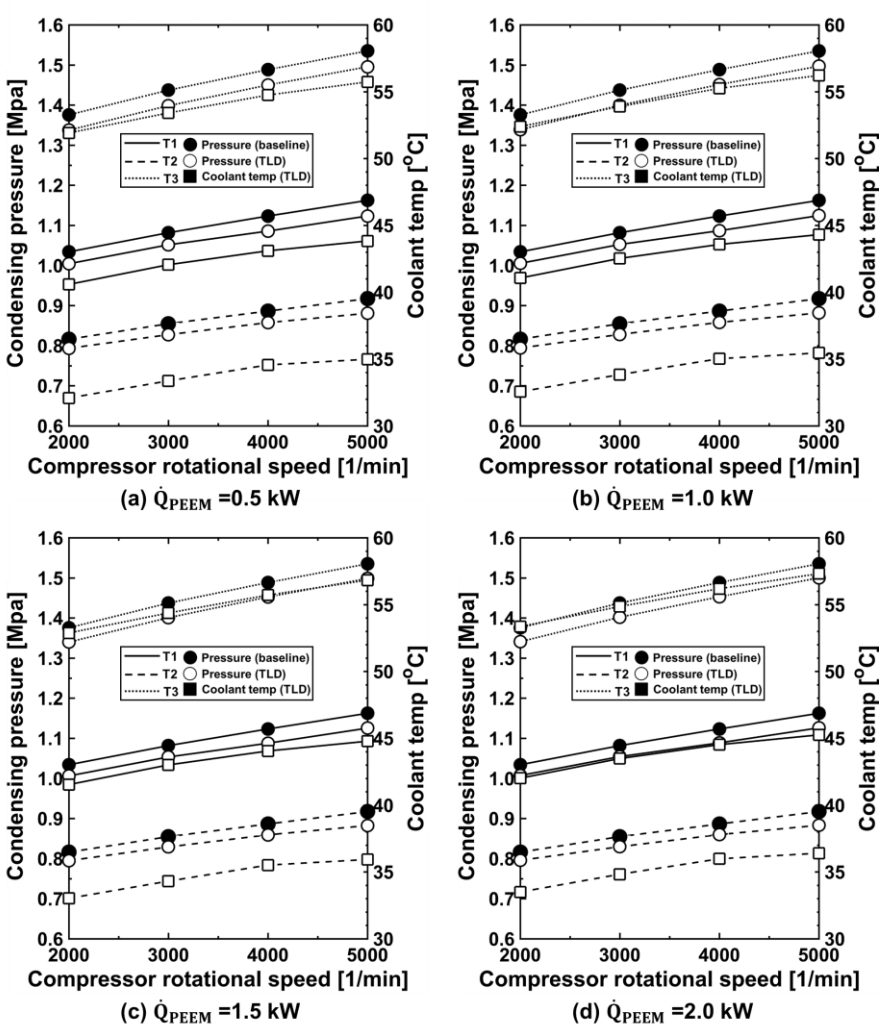

Fig. 3.16 Thermal load distribution strategy for the integrated electric vehicle thermal management system

compared to the baseline. This is because using the thermal load distribution strategy the condensing load for the outdoor heat exchanger is dispersed to the low temperature radiator through the internal heat exchanger. If this method is applied to an electric vehicle, it is possible to increase the maximum driving distance of the electric vehicle by reducing the power consumption used by the heat pump in summer. However, this approach can be applied when the thermal load generated in the PEEM cooling system is relatively low compared to the LTR cooling load. If the cooling capacity of the radiator is not large enough, or the thermal load generated by the PEEM is high, applying this strategy may increase the temperature of the cooling water and cause thermal damage to the PEEM.

3.5 Results and discussion

In order to verify the power consumption reduction of the proposed IEVTMS comparing with the baseline IEVTMS, both heating and cooling capacity, and power consumption from the compressor are measured. For cabin heating mode, the rotational speed of compressor is set to be 3500 rev/min, and 3000 rev/min for cabin cooling mode. In the case of the heating mode, the amount of power consumed when using only the PTC heater and the basic heat pump system was compared to confirm the reduction in the power consumption of the proposed system. Through the above-mentioned cabin thermal modeling, the heating capacity that satisfies the thermal comfort of zero according to the outside temperature was calculated. In order to satisfy the heating load according to the outside temperature, the power required by the PTC heater and compressor was compared. As a result, the proposed IEVTMS showed 15.6% at -7ºC, 28.2% at 2ºC, and 57.1% at 7ºC comparing with the PTC only heating system. In the cooling mode of the proposed system, the newly introduced internal heat exchanger and ODHX are used to remove the high-temperature and high-pressure refrigerant heat to the outside. In the cooling mode of the proposed system, the newly introduced internal heat exchanger and ODHX are used to remove the high-temperature and high-pressure refrigerant heat to the outside. The power consumed by the compressor of the baseline system and the

heat pump system to which the thermal load distribution was applied was compared based on the cooling capacity required according to the outside temperature calculated through cabin thermal modeling. The flow rate of water flowing into the internal heat exchanger was selected as 10 L/min, and the inflow temperature was selected as the outside temperature. As a result of the experiment, it was confirmed that the reduction of the power consumption of the compressor in various temperature ranges was 8.5% at 27ºC, 11.3% at 35ºC, and 7.8% at 47ºC.

3.6 Summary

An experimental study was conducted to confirm the effect of reducing the power consumption of the proposed IEVTMS. In order to check the reduction of power consumption for the heat pump system, it was compared with the electric power required by the basic system, and as a result, it was possible to reduce the power consumed in cabin heat management for various outdoor temperature conditions. For cabin heating mode, the compressor rotational speed is set to be 3500 rev/min, and 3000 rev/min for cabin cooling mode. In the case of the heating mode, the amount of power consumed when using only the PTC heater and the basic heat pump system was compared to confirm the reduction in the power consumption of the proposed system. Through the above-mentioned cabin thermal modeling, the heating capacity that satisfies the thermal comfort of zero according to the outside temperature was calculated. In order to satisfy the heating load according to the outside temperature, the power required by the PTC heater and compressor was compared. As a result, the proposed ITMS showed 15.6% at -7ºC, 28.2% at 2 ºC, and 57.1% at 7ºC. In the cooling mode of the proposed system, the newly introduced internal heat exchanger and ODHX are used to remove the high-temperature and high-pressure refrigerant heat to the outside. In the cooling mode of the proposed system, the newly introduced internal heat exchanger and

ODHX are used to remove the high-temperature and high-pressure refrigerant heat to the outside. However, when the unused heat energy generated from PEEM is directly supplied to the room, if the high pressure of the heat pump system is not sufficiently formed, heat can be absorbed from the cooling water system. In addition, when heat is transferred from a high-temperature refrigerant to the cooling water through internal heat exchanger the flow rate of the cooling water must be secured so that the temperature of the cooling water flowing into the PEEM is properly maintained. It if possible that an increase in the flow rate of cooling water leads to an increase in the power consumption of EWP due to an increase in the differential pressure, but since the power consumption of EWP is not as large as that of the compressor, as shown in Fig 3.16, it does not have a significant effect on the overall increase in COP.

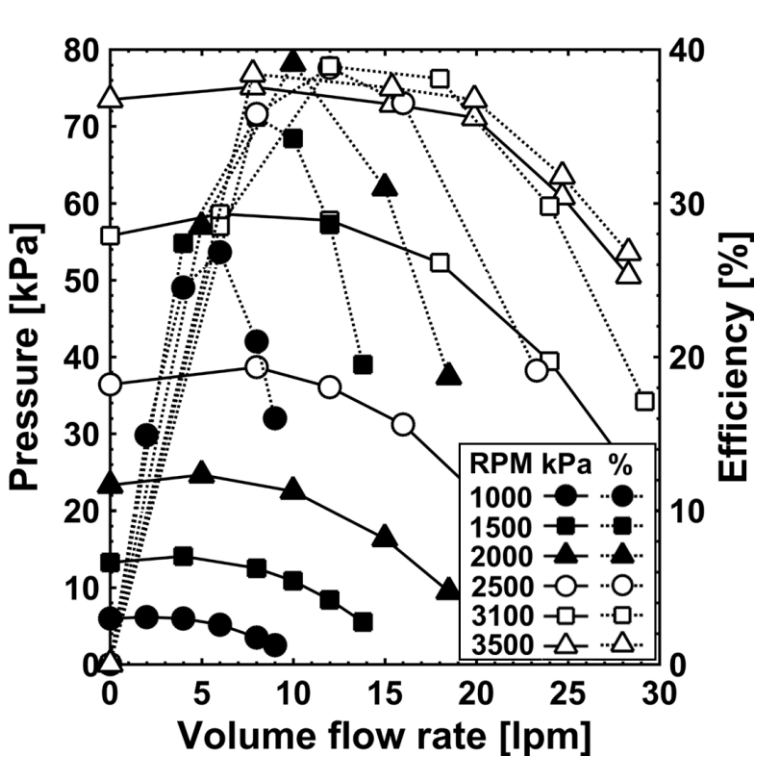

Fig. 3.17 Electric water pump (centrifugal pump) performance and efficiency curve

Chapter 4 The effect of the IEVTMS on range extension

4.1 Introduction

In order to verify the effect of the new IEVTMS to the range extension, electric vehicle mileage prediction model is developed. The newly developed mileage prediction model was developed based on current, unlike the previous studies, and was designed to take into account losses occurring in each element according to the operating temperature of the vehicle's main heat source. A new IEVTMS was designed to secure the baseline system, which lacks thermal connectivity. The most important point in the newly proposed IEVTMS design is to design a system that can more efficiently respond to cabin thermal loads that change significantly with changes in ambient temperature.

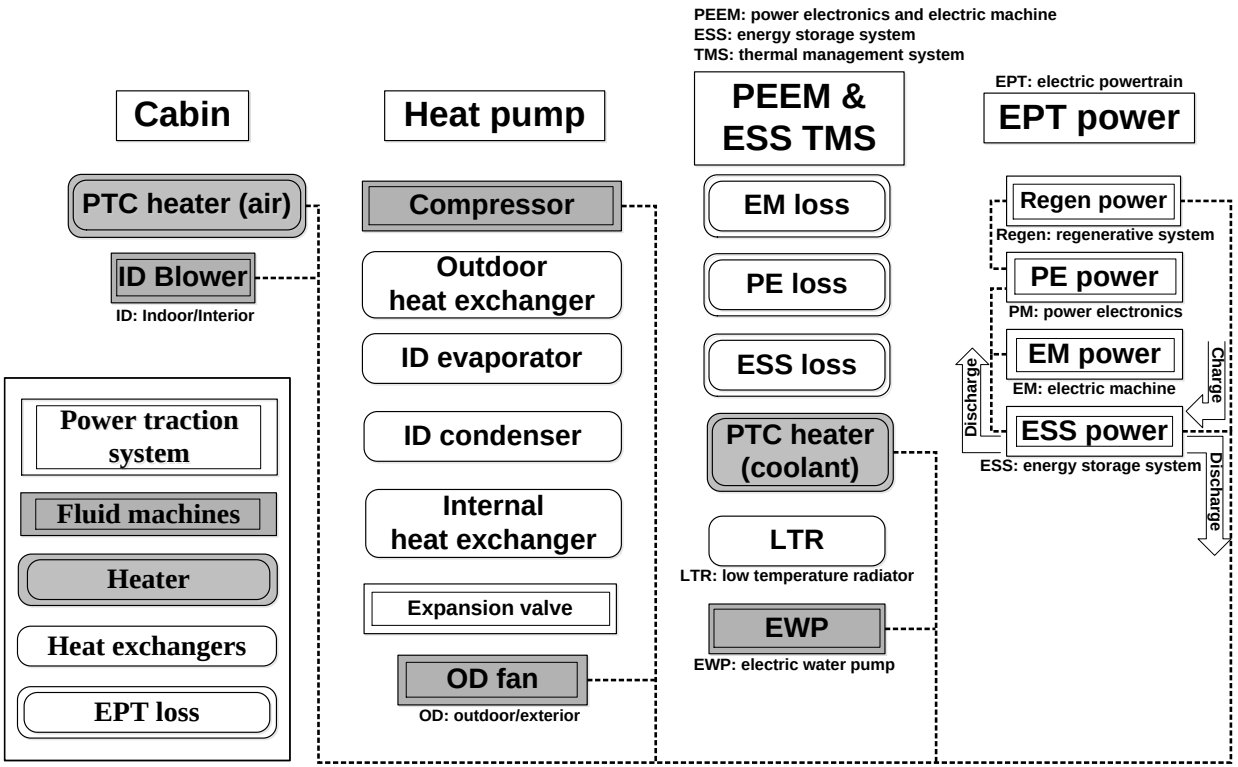

Fig. 4.1 Energy flow diagram for power electronics and electric machine and thermal management system

The electric power from the ESS is consumed by the PTC air heater, indoor air blower, compressor, outdoor air fan, electric water pump, and PTC heater coolant for ESS thermal management for cold winter start-up. In addition, the regenerative braking system that is performed at EM and PE, and the kinetic energy of the vehicle which is recharged to the ESS through the inverter are also considered for the simulation results. In this study, among the various electric power used in TMS, it was confirmed how the change of power consumed by the compressor and PTC air heater affects the increase of the mileage of the electric vehicle. Of course, thermal management system except for the compressor and PTC air heater is a little considerable, the compressor and PTC air heater account for about 77% of the total power consumption of TMS, so the power consumption of the remaining elements were not considered.

4.2 The effect of the IEVTMS for range extension

The schematic diagram of the electric power system of an electric vehicle is shown in Fig. 4.1. In order to figure out the relation power consumption for TMS to mileage of BEV, it is imperative to develop an integrated power transfer and loss model for a light-duty battery electric vehicle. This model should consider the power consumption from PTC air heater and high-voltage compressor. The model initially reads basic information such as the weight of the vehicle. Then read the initial state, such as EPT temperature, battery pack voltage and SOC. When the driving load is determined through the equation of motion of the vehicle, the loss in the corresponding PEEM is calculated. The final power is transferred to the battery based on the calculated loss. In the battery, the final output power is determined by counting the power consumed by the TMS in real time as well as the driving load and losses. When the output power is determined, it is combined with the SOC and voltage of the battery and moves on to the next type step. Fig 4.1 shows the numerical results for the integrated power transfer and loss model predicting the total power consumption for the battery electric vehicle. This figure compares the electric energy consumed by an electric vehicle that only heats the room with PTC and an electric vehicle with IEVTMS. The lower the outside temperature, the greater the heating capacity is required for indoor heating. If heating is

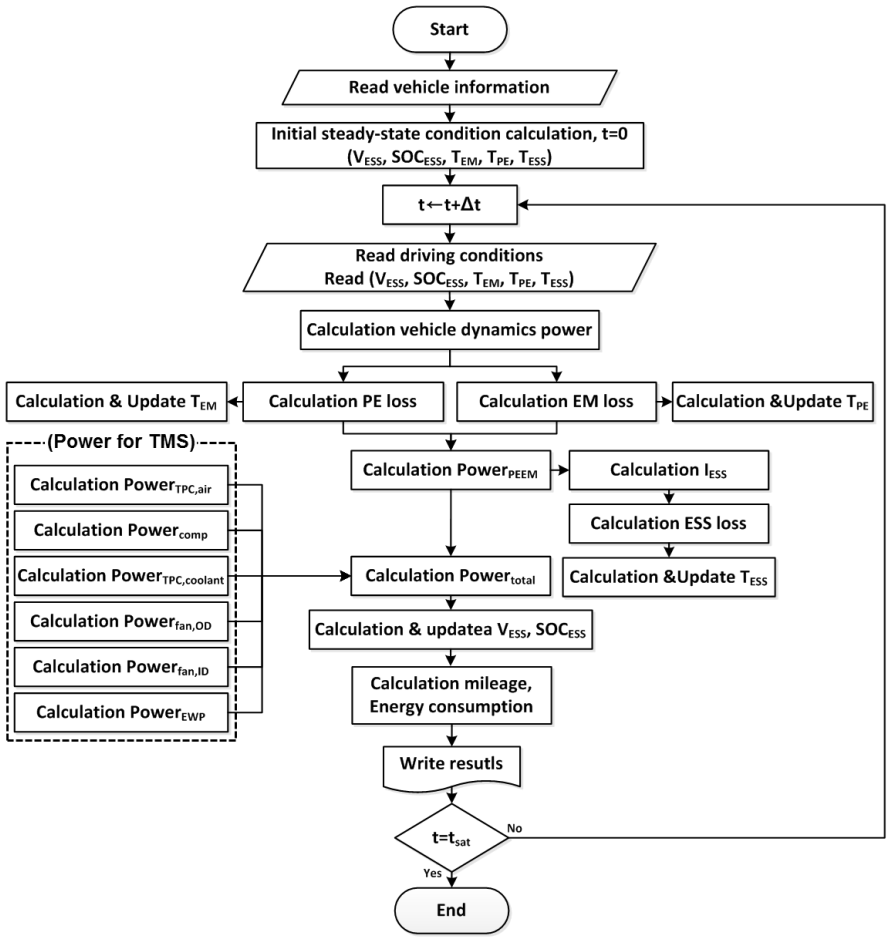

Fig. 4.2 A computational algorithm for a transient state of mileage and energy consumption for a light-duty battery electric vehicle

performed under H3 condition only with PTC heater, about 5.2 kWh of energy is consumed. However, if IEVTMS is applied, energy use can be reduced by about -18%. The reason is that the use of the heat pump actively utilizes the waste heat generated by the PEEM, and if the heating capacity of the heat pump is insufficient, the heating capacity is supplemented through the PTC heater. This tendency increases as the outside temperature in winter gets warmer, and energy use can be reduced by up to -53% in H1 conditions. Although the analysis was performed by setting the operating temperatures of the motor, inverter, and battery differently for each outdoor temperature, the management temperature of each component did not significantly affect the energy consumption result. This is because the energy used by compressors and PTC air heaters is a major cause of the reduction in mileage in automobiles. When the consumption of electric energy used in indoor heating and cooling is reduced, efficiency increases, which means that the driving distance of an electric vehicle can be increased.

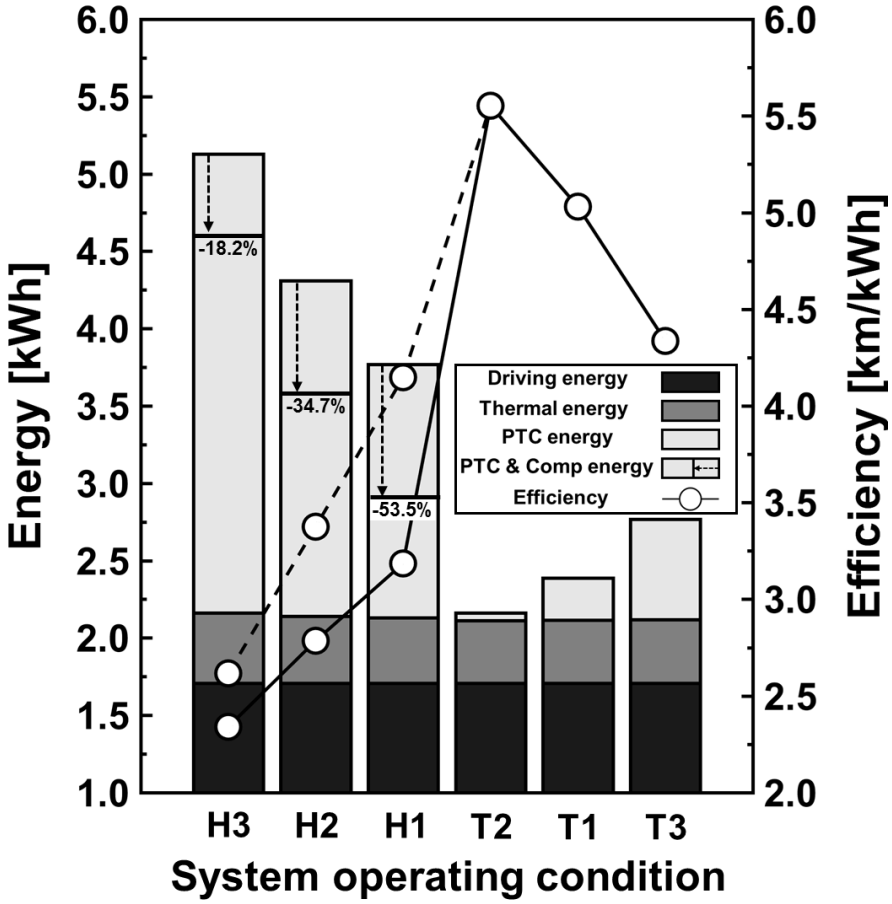

Fig. 4.2 Energy consumption and efficiency of the IEVTMS

(Driving cycle: UDDS)

4.3 Range extension opportunities for various ambient temperature

In order to quantitatively evaluate the effect of the newly proposed IEVTMS on the mileage increase, an analysis on the electric vehicle mileage prediction was performed based on the heat pump efficiency performed through the experiment. Figure 4.3 shows that IEVTMS has a positive effect on increasing the mileage of electric vehicles at various outside temperatures. This is because using the thermal load distribution strategy the condensing load for the outdoor heat exchanger is dispersed to the low temperature radiator through the internal heat exchanger. If this method is applied to an electric vehicle, it is possible to increase the maximum driving distance of the electric vehicle by reducing the power consumption used by the heat pump in summer. Power consumed by the heat pump can be reduced if the unused heat energy generated from PEEM is directly supplied as indoor heating heat during winter indoor heating. However, this approach can be applied when the thermal load generated in the PEEM cooling system is relatively low compared to the LTR cooling load. If the cooling capacity of the radiator is not large enough, or the thermal load generated by the PEEM is high, applying this strategy may increase the temperature of the cooling water and cause thermal damage to the PEEM.

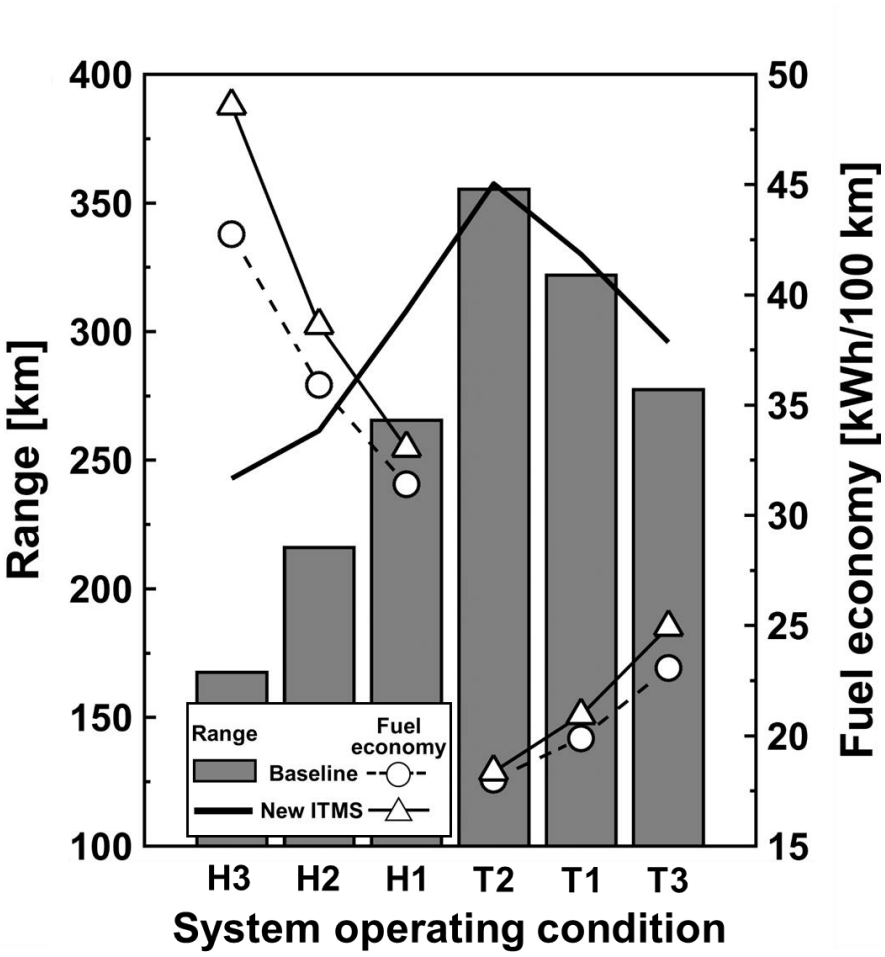

Fig. 4.3 The effect of the new integrated thermal management system for range extension of light duty electric vehicles

4.4 Summary

The consumption power to satisfy the required heat load according to various outdoor conditions was calculated through experiments. As a result, it was confirmed that the power consumption was reduced in the proposed ITMS. In order to check how this reduction in power consumption can affect the mileage increase of electric vehicles, the mileage prediction program of LDBEV was developed to confirm the effect of mileage increase. By reducing the power consumed by HVAC, the distance efficiency of electric vehicles in winter increased by up to 35% (7ºC, driving cycle: NYCC). In addition, the mileage increased by an average of 8% in ITMS with the summer thermal distribution strategy. The increase in mileage in summer was found in NYCC, which has the smallest driving load. The reason is that in the case of NYCC having a small running load, since the heat energy to be radiated from the LTR is small, it is more effective to remove the heat energy of the refrigerant compressed at high temperature and high pressure through the compressor out of the vehicle.

Chapter 5 Concluding remarks

In order to improve the range of battery electric vehicle, the integrated thermal management system very important. However, in order to design ITMS, it is possible to design not only the heat load condition that satisfies the thermal comfort of the vehicle cabin, but also the transmission and loss of electrical energy between the main components of the pure electric vehicle, the motor, the inverter, and the battery. However, all of the existing studies did not obtain a perspective on the efficiency increase due to system integration by performing independent studies. In this study, after designing the ITMS for increasing the mileage of an electric vehicle and confirming the reduction rate of power consumption in the proposed ITMS, the proposed system quantitatively analyzed the mileage increase rate of the vehicle through simulation of the vehicle level.

In the chapter 2, In order to design an efficient HVAC system, the system design perspective needs to be expanded to the vehicle scale to increase the thermal linkage between electric powertrain (EPT) and HVAC. In order to design an integrated thermal management system, it is essential to investigate thermal loads required from both the EPT and cabin, respectively, under several driving conditions and outdoor conditions. A sequential approach with electric current base is developed to get the amount of power transfer and loss from

PEEM and ESS for various driving conditions, such as constant and dynamic respectively. The vehicle under this study is a long-range, light-duty battery electric vehicle. In order to calculate the power transfer and loss for PEEM, 150 kW IPMSM is designed for an electric machine. And then, the electromagnetic field analysis is conducted. For the power electronics, a three-phase full-bridge inverter/converter is designed, and the amount of heat generation from the high-voltage power electronics is predicted by electric current-based model. The power loss model for lithium-ion battery pack is referred to the experimental data. Those prime components for electric traction system are combined with vehicle dynamics and regenerative braking system. To estimate the state of charge (SOC) on various driving loads, the multi-component simulation model is developed. Furthermore, its results are verified with real-world on-road vehicle data. Also, in order to investigate the characteristics of electric power transfer and loss according to the dynamic driving profile, the moving average method is applied to the existing urban dynamometer driving schedule (UDDS) velocity profile generating new velocity profiles with a low acceleration-deceleration rate.

In the chapter 3, In the case of the heating mode, the amount of power consumed when using only the PTC heater and the basic heat pump system was compared to confirm the reduction in the power consumption of the proposed

system. Through the above-mentioned cabin thermal modeling, the heating capacity that satisfies the thermal comfort of zero according to the outside temperature was calculated. In order to satisfy the heating load according to the outside temperature, the power required by the PTC heater and compressor was compared. As a result, the proposed ITMS showed 15.6% at -7ºC, 28.2% at 2 ºC, and 57.1% at 7 ºC. In the cooling mode of the proposed system, the newly introduced internal heat exchanger and ODHX are used to remove the high-temperature and high-pressure refrigerant heat to the outside. In the cooling mode of the proposed system, the newly introduced internal heat exchanger and ODHX are used to remove the high-temperature and high-pressure refrigerant heat to the outside. The power consumed by the compressor of the baseline system and the heat pump system to which the thermal load distribution was applied was compared based on the cooling capacity required according to the outside temperature calculated through cabin thermal modeling. The flow rate of water flowing into the internal heat exchanger was selected as 10 L/min, and the inflow temperature was selected as the outside temperature. As a result of the experiment, it was confirmed that the reduction of the power consumption of the compressor in various temperature ranges was 8.5% at 27ºC, 11.3% at 35 ºC, and 7.8% at 47 ºC.

Finally, in the chapter 4, a range prediction model for battery electric

vehicle was developed. In this chapter, the mileage prediction program of LDBEV was developed to confirm the effect of mileage increase. By reducing the power consumed by HVAC, the distance efficiency of electric vehicles in winter increased by up to 35% (7°C, driving cycle: NYCC). In addition, the mileage increased by an average of 8% in ITMS with the summer thermal distribution strategy. The increase in mileage in summer was found in NYCC, which has the smallest driving load. The reason is that in the case of NYCC having a small running load, since the heat energy to be radiated from the LTR is small, it is more effective to remove the heat energy of the refrigerant compressed at high temperature and high pressure through the compressor out of the vehicle.

In conclusion, in this study, a new integrated thermal management system and its effect to range extension were presented. Using system, range extension for various ambient condition was possible, which is expected to improve 12% average.

[1] World Energy Balances 2019, IEA

[2] Yagcitekin, B., Uzunoglu, M., Karakas, A., & Erdinc, O. (2015). Assessment of electrically-driven vehicles in terms of emission impacts and energy requirements: a case study for Istanbul, Turkey. Journal of Cleaner Production, 96, 486-492.

[3] Hawkins, T. R., Gausen, O. M., & Strømman, A. H. (2012). Environmental impacts of hybrid and electric vehicles—a review. The International Journal of Life Cycle Assessment, 17(8), 997-1014.

[4] Fernández, R. Á., Caraballo, S. C., Cilleruelo, F. B., & Lozano, J. A. (2018). Fuel optimization strategy for hydrogen fuel cell range extender vehicles applying genetic algorithms. Renewable and sustainable energy reviews, 81, 655-668.

[5] Noel, L., de Rubens, G. Z., Sovacool, B. K., & Kester, J. (2019). Fear and loathing of electric vehicles: the reactionary rhetoric of range anxiety. Energy research & social science, 48, 96-107.

[6] Neubauer, J., & Wood, E. (2014). The impact of range anxiety and home, workplace, and public charging infrastructure on simulated battery electric vehicle lifetime utility. Journal of power sources, 257, 12-20.

[7] AAA Electric vehicle range testing, 2019

[8] Neubauer, J., & Wood, E. (2014). The impact of range anxiety and home,

workplace, and public charging infrastructure on simulated battery electric vehicle lifetime utility. Journal of power sources, 257, 12-20.

[9] Bakker, J. J., Mom, G. P. A., & Schot, J. W. (2011). Contesting range anxiety: The role of electric vehicle charging infrastructure in the transportation transition. Technische Universiteit Eindhoven.

[10] King, C., Griggs, W., Wirth, F., Quinn, K., & Shorten, R. (2015). Alleviating a form of electric vehicle range anxiety through on-demand vehicle access. International Journal of Control, 88(4), 717-728.

[11] Ji, F., Zhang, X., Du, F., Ding, S., Zhao, Y., Xu, Z., ... & Zhou, Y. (2020). Experimental and numerical investigation on micro gas turbine as a range extender for electric vehicle. Applied Thermal Engineering, 115236.

[12] Prasad, R. M., & Krishnamoorthy, A. (2019). Design validation and analysis of the drive range enhancement and battery bank deration in electric vehicle integrated with split power solar source. Energy, 172, 106-116.

[13] Geraee, S., Mohammadbagherpoor, H., Shafiei, M., Valizadeh, M., Montazeri, F., & Feyzi, M. R. (2018). Regenerative braking of electric vehicle using a modified direct torque control and adaptive control theory. Computers & Electrical Engineering, 69, 85-97.

[14] Madhusudhanan, A. K. (2019). A method to improve an electric vehicle's range: Efficient Cruise Control. European Journal of Control, 48, 83-96.

[15] Farrington, R., & Rugh, J. (2000). Impact of vehicle air-conditioning on fuel economy, tailpipe emissions, and electric vehicle range (No. NREL/CP-540-28960). National Renewable Energy Lab., Golden, CO (US).

[16] Zubi, G., Dufo-López, R., Carvalho, M., & Pasaoglu, G. (2018). The lithium-ion battery: State of the art and future perspectives. Renewable and Sustainable Energy Reviews, 89, 292-308.

[17] Nitta, N., Wu, F., Lee, J. T., & Yushin, G. (2015). Li-ion battery materials: present and future. Materials today, 18(5), 252-264.

[18] Fotouhi, A., Auger, D. J., Propp, K., Longo, S., & Wild, M. (2016). A review on electric vehicle battery modelling: From Lithium-ion toward Lithium–Sulphur. Renewable and Sustainable Energy Reviews, 56, 1008-1021.

[19] Aaldering, L. J., & Song, C. H. (2019). Tracing the technological development trajectory in post-lithium-ion battery technologies: A patent-based approach. Journal of Cleaner Production, 241, 118343.

[20] Duchêne, L., Remhof, A., Hagemann, H., & Battaglia, C. (2020). Status and prospects of hydroborate electrolytes for all-solid-state batteries. Energy Storage Materials, 25, 782-794.

[21] Li, P., Zhao, G., Zheng, X., Xu, X., Yao, C., Sun, W., & Dou, S. X. (2018). Recent progress on silicon-based anode materials for practical lithium-ion

battery applications. Energy Storage Materials, 15, 422-446.

[22] Zhang, X. Q., Zhao, C. Z., Huang, J. Q., & Zhang, Q. (2018). Recent advances in energy chemical engineering of next-generation lithium batteries. Engineering, 4(6), 831-847.

[23] Siruvuri, S. V., & Budarapu, P. R. (2020). Studies on thermal management of Lithium-ion battery pack using water as the cooling fluid. Journal of Energy Storage, 29, 101377.

[24] Siruvuri, S. V., & Budarapu, P. R. (2020). Studies on thermal management of Lithium-ion battery pack using water as the cooling fluid. Journal of Energy Storage, 29, 101377.

[25] Lai, Y., Wu, W., Chen, K., Wang, S., & Xin, C. (2019). A compact and lightweight liquid-cooled thermal management solution for cylindrical lithium-ion power battery pack. International Journal of Heat and Mass Transfer, 144, 118581.

[26] Kiyota, K., & Chiba, A. (2012). Design of switched reluctance motor competitive to 60-kW IPMSM in third-generation hybrid electric vehicle. IEEE Transactions on Industry Applications, 48(6), 2303-2309.

[27] Yilmaz, M. (2015). Limitations/capabilities of electric machine technologies and modeling approaches for electric motor design and analysis in plug-in electric vehicle applications. Renewable and Sustainable Energy

Reviews, 52, 80-99.

[28] Tariq, A. R., Nino, C. E., & Strangas, E. G. (2009, July). Effect of cooling conditions on the design and operation of IPMSM. In 2009 IEEE Power & Energy Society General Meeting (pp. 1-10). IEEE.

[29] Park, C. B. (2014). Thermal analysis of IPMSM with water cooling jacket for railway vehicles. Journal of Electrical Engineering & Technology, 9(3), 882-887.

[30] Kang, M., Guo, L., Wang, H., Wang, Z., & Xia, C. (2019, August). An Improved Rotor Cooling Structure of IPMSM. In 2019 22nd International Conference on Electrical Machines and Systems (ICEMS) (pp. 1-6). IEEE.

[31] Li, L., Li, X., Wang, X., Song, J., He, K., & Li, C. (2016). Analysis of downshift's improvement to energy efficiency of an electric vehicle during regenerative braking. Applied Energy, 176, 125-137.

[32] Qiu, C., Wang, G., Meng, M., & Shen, Y. (2018). A novel control strategy of regenerative braking system for electric vehicles under safety critical driving situations. Energy, 149, 329-340.

[33] Lv, C., Zhang, J., Li, Y., & Yuan, Y. (2015). Novel control algorithm of braking energy regeneration system for an electric vehicle during safety–critical driving maneuvers. Energy conversion and management, 106, 520-529.

[34] Wu, J., Wang, X., Li, L., & Du, Y. (2018). Hierarchical control strategy with battery aging consideration for hybrid electric vehicle regenerative braking control. Energy, 145, 301-312.

[35] Bashash, S., Moura, S. J., Forman, J. C., & Fathy, H. K. (2011). Plug-in hybrid electric vehicle charge pattern optimization for energy cost and battery longevity. Journal of power sources, 196(1), 541-549.

[36] Heydari, S., Fajri, P., Rasheduzzaman, M., & Sabzehgar, R. (2019). Maximizing regenerative braking energy recovery of electric vehicles through dynamic low-speed cutoff point detection. IEEE Transactions on Transportation Electrification, 5(1), 262-270.

[37] Yuan, Y., Zhang, J., Li, Y., & Li, C. (2018). A novel regenerative electrohydraulic brake system: Development and hardware-in-loop tests. IEEE Transactions on Vehicular Technology, 67(12), 11440-11452.

[38] Chau, K. T., & Wong, Y. S. (2002). Overview of power management in hybrid electric vehicles. Energy conversion and management, 43(15), 1953-1968.

[39] Banjac, T., Trenc, F., & Katrašnik, T. (2009). Energy conversion efficiency of hybrid electric heavy-duty vehicles operating according to diverse drive cycles. Energy Conversion and Management, 50(12), 2865-2878.

[40] Silva, C., Ross, M., & Farias, T. (2009). Evaluation of energy consumption,

emissions and cost of plug-in hybrid vehicles. Energy Conversion and Management, 50(7), 1635-1643.

[41] Silva, C., Ross, M., & Farias, T. (2009). Evaluation of energy consumption, emissions and cost of plug-in hybrid vehicles. Energy Conversion and Management, 50(7), 1635-1643.

[42] Katrašnik, T. (2011). Energy conversion phenomena in plug-in hybrid-electric vehicles. Energy Conversion and Management, 52(7), 2637-2650.

[43] Gao, Z., LaClair, T., Ou, S., Huff, S., Wu, G., Hao, P., ... & Barth, M. (2019). Evaluation of electric vehicle component performance over eco-driving cycles. Energy, 172, 823-839.

[44] Zhang, L., Hashimoto, K., Hasegawa, H., & Saikawa, M. (2018). Performance analysis of a heat pump system with integrated desiccant for electric vehicles. International Journal of Refrigeration, 86, 154-162.

[45] Zhang, G., Zou, H., Qin, F., Xue, Q., & Tian, C. (2017). Investigation on an improved heat pump AC system with the view of return air utilization and anti-fogging for electric vehicles. Applied Thermal Engineering, 115, 726-735.

[46] Ahn, J. H., Kang, H., Lee, H. S., & Kim, Y. (2015). Performance characteristics of a dual-evaporator heat pump system for effective dehumidifying and heating of a cabin in electric vehicles. Applied

Energy, 146, 29-37.

[47] Ahn, J. H., Kang, H., Lee, H. S., Jung, H. W., Baek, C., & Kim, Y. (2014). Heating performance characteristics of a dual source heat pump using air and waste heat in electric vehicles. Applied Energy, 119, 1-9.

[48] Han, X., Zou, H., Wu, J., Tian, C., Tang, M., & Huang, G. (2020). Investigation on the heating performance of the heat pump with waste heat recovery for the electric bus. Renewable Energy, 152, 835-848.

[49] Choi, Y. U., Kim, M. S., Kim, G. T., Kim, M., & Kim, M. S. (2017). Performance analysis of vapor injection heat pump system for electric vehicle in cold startup condition. International Journal of Refrigeration, 80, 24-36.

[50] Tian, Z., Gu, B., Gao, W., & Zhang, Y. (2020). Performance evaluation of an electric vehicle thermal management system with waste heat recovery. Applied Thermal Engineering, 169, 114976.

[51] Zhi, M., Xiang, C., Li, J., Li, M., & Wu, N. (2013). Nanostructured carbon–metal oxide composite electrodes for supercapacitors: a review. Nanoscale, 5(1), 72-88.

[52] López, I., Ibarra, E., Matallana, A., Andreu, J., & Kortabarria, I. (2019). Next generation electric drives for HEV/EV propulsion systems: Technology, trends and challenges. Renewable and Sustainable Energy Reviews, 114,

109336.

[53] Jahns, T. M., Kliman, G. B., & Neumann, T. W. (1986). Interior permanent-magnet synchronous motors for adjustable-speed drives. IEEE Transactions on Industry Applications, (4), 738-747.

[54] Krause, P, C., Analyis of electric machinery and drive systems, 2nd, Wiley-Interscience

[55] Nihonyanagi, A., Takemoto, M., Ogasawara, S., Aoki, N., & Lee, K. (2016, September). Examination to enhance efficiency of V-shaped IPMSM using concentrated winding structure at high speed and high torque area. In 2016 IEEE Energy Conversion Congress and Exposition (ECCE) (pp. 1-6). IEEE.

[56] FluxMotor 2018, Altair

[57] Huang, W., Zhang, Y., Zhang, X., & Sun, G. (2013). Accurate torque control of interior permanent magnet synchronous machine. IEEE Transactions on Energy Conversion, 29(1), 29-37.

[58] López, I., Ibarra, E., Matallana, A., Andreu, J., & Kortabarria, I. (2019). Next generation electric drives for HEV/EV propulsion systems: Technology, trends and challenges. Renewable and Sustainable Energy Reviews, 114, 109336.

[59] Morimoto, S., Tong, Y., Takeda, Y., & Hirasa, T. (1994). Loss minimization control of permanent magnet synchronous motor drives. IEEE Transactions

on industrial electronics, 41(5), 511-517.

[60] Liu, J., Gong, C., Han, Z., & Yu, H. (2018). IPMSM model predictive control in flux-weakening operation using an improved algorithm. IEEE Transactions on Industrial Electronics, 65(12), 9378-9387.

[61] Ekanayake, S., Dutta, R., Rahman, M. F., Xiao, D., & Fletcher, J. (2016). Operation along the maximum torque per voltage trajectory in a direct torque and flux controlled interior permanent magnet synchronous motor.

[62] Fadel, M., Sepulchre, L., & Pietrzak-David, M. (2018). Deep Flux-Weakening Strategy with MTPV for High-Speed IPMSM for Vehicle Application. IFAC-PapersOnLine, 51(28), 616-621.

[63] Venkataraman, B., Godsey, B., Premerlani, W., Shulman, E., Thaku, M., & Midence, R. (2005, April). Fundamentals of a motor thermal model and its applications in motor protection. In 58th Annual Conference for Protective Relay Engineers, 2005. (pp. 127-144). IEEE.

[64] Ruoho, S., Kolehmainen, J., Ikaheimo, J., & Arkkio, A. (2009). Interdependence of demagnetization, loading, and temperature rise in a permanent-magnet synchronous motor. IEEE Transactions on Magnetics, 46(3), 949-953.

[65] Fan, J., Zhang, C., Wang, Z., Dong, Y., Nino, C. E., Tariq, A. R., & Strangas, E. G. (2010). Thermal analysis of permanent magnet motor for the electric

vehicle application considering driving duty cycle. IEEE Transactions on Magnetics, 46(6), 2493-2496.

[66] HybridPACK™ 2 Module, infinion

[67] Thoben, M., Mainka, K., Bayerer, R., Graf, I., & Münzer, M. (2008, May). From vehicle drive cycle to reliability testing of power modules for hybrid vehicle inverter. In PCIM Europe (pp. 27-29).

[68] OKUBO, K., MASUDA, M., KATO, Y., & NAKATANI, Y. (2008). Development of Low-loss Inverters for Electric Vehicle (EV) Motors. Mitsubishi Heavy Industries Technical Review, 45(3).

[69] Doh, C. H., Ha, Y. C., & Eom, S. W. (2019). Entropy measurement of a large format lithium ion battery and its application to calculate heat generation. Electrochimica Acta, 309, 382-391.

[70] Viswanathan, V. V., Choi, D., Wang, D., Xu, W., Towne, S., Williford, R. E., ... & Yang, Z. (2010). Effect of entropy change of lithium intercalation in cathodes and anodes on Li-ion battery thermal management. Journal of Power Sources, 195(11), 3720-3729.

[71] Hosseinzadeh, E., Genieser, R., Worwood, D., Barai, A., Marco, J., & Jennings, P. (2018). A systematic approach for electrochemical-thermal modelling of a large format lithium-ion battery for electric vehicle application. Journal of power sources, 382, 77-94.

[72] Hosseinzadeh, E., Genieser, R., Worwood, D., Barai, A., Marco, J., & Jennings, P. (2018). A systematic approach for electrochemical-thermal modelling of a large format lithium-ion battery for electric vehicle application. Journal of power sources, 382, 77-94.

[73] Huang, C. C. D. (1998). A dynamic computer simulation model for automobile passenger compartment climate control and evaluation (Doctoral dissertation, Michigan Technological University).

[74] ISO 15042, 2017, Multiple split-system air conditioners and air-to-air heat pumps-Testing and rating for performance

[75] J2765, 2008, Procedure for Measuring System COP of a Mobile Air Conditioning System on a Test Bench, SAE

[76] Chang, Y. J., & Wang, C. C. (1997). A generalized heat transfer correlation for Iouver fin geometry. International Journal of heat and mass transfer, 40(3), 533-544.

[77] Gnielinski, V., chem,. Eng., 16, 359, 1976

[78] Koyama, S., Kuwahara, K., & Nakashita, K. (2003, January). Condensation of refrigerant in a multi-port channel. In International Conference on Nanochannels, Microchannels, and Minichannels (Vol. 36673, pp. 193-205).

[79] Sun, L., & Mishima, K. (2009). An evaluation of prediction methods for

saturated flow boiling heat transfer in mini-channels. International Journal of Heat and Mass Transfer, 52(23-24), 5323-5329.

[80] Standard, A. S. H. R. A. E., & Standard, A. S. H. R. A. E. (1999). Laboratory methods of testing fans for aerodynamic performance rating.

국 문 초 록

전기자동차의 1 회 충전 주행거리는 탑재된 배터리의 전기용량에 의하여 결정된다. 하지만 최근 적용되고 있는 리튬-이온 배터리의 경우 단위 무게당 에너지 밀도의 한계로 인해 전기승용차의 1 회 충전 최대 주행거리는 약 350~400 km 를 상회한다. 그런데 이러한 최대 주행 가능 거리는 외기온도에 의해 크게 변동되며 운전자로 하여금 심각한 거리불안감을 유발하고 있으며 이는 전기자동차의 보급 확대에 큰 걸림돌로 알려져 있다. 외기온도에 따라 주행거리가 변화하는 가장 큰 원인은 차량의 실내 열관리를 위해 냉난방 공조시스템에서 요구하는 전기에너지가 클 뿐만 아니라, 이러한 에너지의 양이 외기온도에 따라 큰 폭으로 변화하기 때문이다. 본 연구는 승용전기자동차의 전동 파워트레인과 공조시스템간의 열적 연계성을 강화시켜 외기온도에 따라 공조시스템 소모 동력 변화가 적은 통합열관리시스템을 제안하였으며, 이러한 통합열관리 시스템이 전기자동차의 주행거리 연장에 미치는 영향성을 정량적으로 분석하였다.

먼저, 시뮬레이션 기반으로 전기자동차의 전동 파워트레인(배터리,모터,인버터)에서 발생하는 발열량 예측 방법을 제시하였다. 배터리, 모터, 인버터는 전기에너지와 기계에너지간의 연속적인 변환과정을 수행한다. 이러한 변환과정에서 전기에너지는 전압과 전류의 형태로 기계에너지로 변환되며 반대로 발생된 기계에너지는 그것의 역 과정을 통해 배터리로 저장되게 된다. 본 연구에서는 각 구성요소에서 발생하는 발열량을 정량적으로 예측하기 위해 기계에너지와 전기에너지의 실시간 변환에 대한 통합 동력전달모델 및 열에너지 손실 모델을 개발하였다.

실외 온도에 따라 차량의 실내에서 요구되는 공조 부하를 정량적으로 예측하기 위해 열 쾌적성 기반의 차량 실내 모델을 개발하였다. 개발된 모델에서는 차량의 외부로부터 유입되는

복사에너지 뿐만 아니라 차량 내장재의 비열까지 고려하여 보다 현실성이 높은 공조 부하량을 예측할 수 있다.

배터리, 인버터, 모터에서 발생하는 발열량과 공조 부하량을 바탕으로 승용전기자동차에 적합한 통합열관리시스템을 설계하였다. 설계된 시스템의 성능과 효율을 검증하기 위해 실험연구를 수행하였으며 그 결과 기본 시스템과 비교하여 난방조건에서는 약 12%, 그리고 냉방조건에서는 약 5% 의 소모동력 저감율을 확인하였다.

이러한 소모동력 저감율이 전기자동차의 주행거리에 미치는 영향력을 확인하기 위해 전기자동차 주행거리 예측 모델을 개발하였다. 다양한 외기조건에 대해 주행거리 증대효과를 확인한 결과 약 10%의 주행거리 증대 효과가 기대된다. 본 연구에서 제시한 통합열관리시스템이 전기자동차에 적용된다면, 외기온도에 따른 주행거리 변화율을 줄이고 나아가 전기자동차 보급에 기여할 수 있을 것으로 기대된다.

주요어: 전기자동차, 통합열관리시스템, 히트펌프, 주행거리

학 번: 2015-30996